ABSTRACT

Title of dissertation: NON-LINEAR DEVELOPMENT OF STREAMING INSTABILITIES IN MAGNETIC RECONNECTION WITH A STRONG GUIDE FIELD

Haihong Che, Doctor of Philosophy, 2009

Dissertation directed by: Professor James F. Drake
Department of Physics

Magnetic reconnection has been recognized as a dominant mechanism for converting magnetic energy into the convective and thermal energy of particles, and has been thought as the driver of explosive events in nature and laboratory, such as solar and stellar flares, magnetic substorms and disruptions in fusion experiments. Magnetic reconnection (Sweet-Parker and Petscheck model) is often modeled using resistive magnetohydrodynamics, in which collisions play the key role in facilitating the release of energy in the explosive events. However, in space plasma the collisional resistivity is far below the required resistivity to explain the observed energy release rate. Turbulence is common in plasmas and the anomalous resistivity induced by the turbulence has been proposed as a mechanism for breaking the frozen-in condition in magnetic reconnection. Turbulence-driven resistivity has remained a poorly understood, but widely invoked mechanism for nearly 50 years. The goal of this project is to understand what role anomalous resistivity plays in fast magnetic reconnection.

Turbulence has been observed in the intense current layers that develop during magnetic reconnection in the Earth's magnetosphere. Electron streaming is believed to be the source of this turbulence. Using kinetic theory and 3D particle-in-cell simulations, we study the nonlinear development of streaming instabilities in 3D magnetic reconnection with a strong guide field. Early in time an intense current sheet develops around the x-line and drives the Buneman instability. Electron holes, which are bipolar spatial localized electric field structures, form and then self-destruct creating a region of strong turbulence around the x-line. At late time turbulence with a characteristic frequency in the lower hybrid range also develops, leading to a very complex mix of interactions. A major challenge is to investigate what occurs after the saturation of Buneman instability and how the momentum and energy are exchanged among the waves and particles by the turbulence.

The difficulty we face in this project is how to address a long-standing problem in nonlinear kinetic theory: how to treat large amplitude perturbations and the associated strong wave-particle interactions. In my thesis, I address this long-standing problem using particle-in-cell simulations and linear kinetic theory.

The kinetic process of 3D magnetic reconnection is complicated. To separate problem of turbulent driven drag from reconnection, we carry out 3D simulations in which we specify the initial streaming velocities of particles to mimic the configuration of the x-line during magnetic reconnection. The geometry is chosen so that reconnection does not develop. Some important physics have been revealed.

1: At late time the lower hybrid instability (LHI) dominates the dynamics in low β plasma in combination with either the electron-electron two-stream instability

(ETS) or the Buneman instability (BI), depending on the parallel phase speed of the LHI. If its parallel phase speed is sufficiently large and leaves sufficient velocity space for the ETS to grow, the ETS takes over the BI and interacts with the LHI to slow the streaming electrons. If not, the BI acts with the LHI to slow the high speed electrons.

2: An instability with a high phase speed is required to tap the energy of the high velocity electrons. The BI with its low phase speed, can not do this. The ETS and the LHI, both have high phase speed.

3: The condition for the formation of stable electron holes requires $|v_p - v_g| < \sqrt{2e|\phi|/m_e}$, where $|\phi|$ is the amplitude of the electric potential, and v_p and v_g are the phase and group velocity of the relevant waves. Like the BI and ETS the LHI can form electron holes.

4: The overlapping resonance in phase space is the dominant mechanism for transporting the momentum and energy from high velocity electrons to low velocity electrons, which then couple to the ions. These resonances also lead to the chaotic motion of electrons in phase space and finally to the destruction of the electron holes.

NON-LINEAR DEVELOPMENT OF STREAMING INSTABILITIES IN MAGNETIC RECONNECTION WITH A STRONG GUIDE FIELD

by

Haihong Che

Dissertation submitted to the Faculty of the Graduate School of the
University of Maryland, College Park in partial fulfillment
of the requirements for the degree of
Doctor of Philosophy
2009

Advisory Committee:
Professor James. F. Drake, Chair/Advisor
Professor Thomas M. Antonsen Jr.
Senior Research Scientist Parvez N. Guzdar
Professor Adil Hassam
Professor Williams Dorland
Professor Eve Ostrike

To my grandma

ACKNOWLEDGMENTS

First and foremost I owe a large amount of gratitude to my advisor, Professor James F. Drake. I thank him for giving me such an invaluable opportunity to work on challenge and awesomely interesting projects. I have learnt a lot from the experience to work with him. His sharp intuition in catching the physics from simulations and his wisdom in exploring physics with simulations will influence me all life.

I owe a lot of thanks to both Drs. Marc Swisdak and Peter Yoon. I can't smoothly finish my thesis without either of them. I am gratitude to Dr. Parvez Guzdar, he always provide me with his inspiring discussions and encouragements.

I wish to thank all of the professors who have taught me. In particular professor Bei-lok Hu and Serguei Novikov. By a small project on the entanglement of relativistic quantum oscillators, professor Hu taught me how to use the sophisticated mathematics to formulate the physics problems. Professor Novikov not only led me into the world of the geometry and topology, but also influenced me with his extraordinary vision and formidable skill in exploring math and physics.

Thanks to my past advisors and teachers for all the help and encouragements they gave me: Professor Liao Liu, Cheng Zhao, Shenglin Cao in Beijing Normal University, Tipei Li in Qinghua university, and Tan Lu in Nanjing University. Professor Robert Nemiroff and Professor Robert Weidman in Michigan Technological

University. Thanks to the staff at IREAP, Mohini, Nancy, Janice, Margaret and Carol, and Jane in department of physics. Many thanks to Ed Condon for his great help on my computers. I also want to thank Professor Chant for his help during my PhD study.

Thanks to all of my past coworkers, Mike Shay, Paul Cassak, Yi-Hsin Liu, Ray Fermo, kevin Schoeffler, and Tak Chu Li. Thanks to my officemates Sepehr Morshed and Andy Pearson for the fun time they brought to me. Thanks to my friends Kate Despain, Jiao Yu and Min Wu for the happy time we were together.

Finally my deepest thanks to my husband Yuxuan for his continuous support and encouragement to me during these years.

TABLE OF CONTENTS

LIST OF TABLES

LIST OF FIGURES

Chapter 1

Anomalous Resistivity and Magnetic Reconnection

1.1 A Brief History of Magnetic Reconnection

On September 1st 1859, Carrington and Hodgson independently (Carrington 1859; Hodgson 1859) observed a giant spot on the Sun. Carrington saw strong light arc lasted for five minutes in his projected picture of the Sun's spot. Later he compared his findings to the measurements at Kew observatory in London and noticed that there was a one-hour interference in the magnetic field exactly at the same time during which the giant spot was observed.

This is the first recorded solar flare. Solar flares occur when magnetic energy built up in the solar atmosphere is suddenly released. They last for seconds to hours. The rate of energy release during a flare is typically on the order of 10^{27} $\mathrm{erg\,s^{-1}}$. A larger flare can emit up to 10^{32} $\mathrm{erg\,s^{-1}}$ of energy. Radiation is emitted from radio waves at long wavelength, through optical emission to x-rays and gamma-rays at short wavelength. Particles, including electrons, ions and heavy nuclei, are accelerated and heated in the solar atmosphere to MeVs during flares.

The corona is the outmost layer of the atmosphere of the Sun, composed of highly rarefied gas with temperature up to a few million degrees Kelvin. The corona is not uniformly bright, Emissions is concentrated around active regions and bright loops as shown in Fig. 1.1. Sunspots are located in these active regions and solar

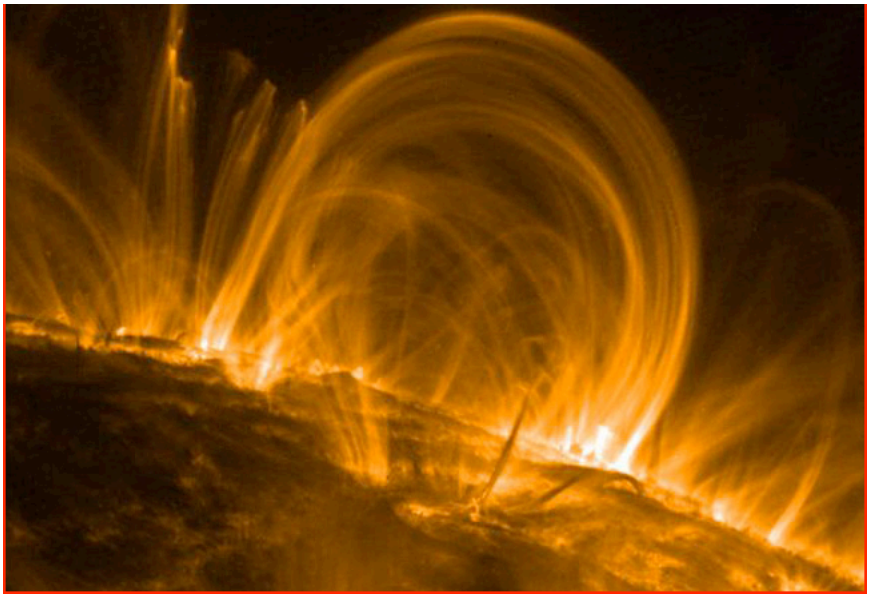

Figure 1.1: This image is the heating coronal loops imaged in extreme ultraviolet light. This TRACE image shows that the strong heating occurs near the bases of the loops emerging and returning to the solar surface. These loops span 30 or more times the diameter of the Earth. (Credit: M. Aschwanden et al. (LMSAL), TRACE and NASA.)

flares occur in active regions. The huge amount of energy releasing is logically related to the magnetic field since the magnetic energy dominates that of the plasma.

The mechanism for the fast release of magnetic energy was mystery until R. G. Giovanelli (Giovanelli 1946) and F. Hoyle (Hoyle 1949) suggested that magnetic X-type null points may be the source for plasma heating and particle acceleration in a solar flare. This is the origin of the magnetic reconnection concept. In 1953, Dungey, a student of Hoyle was the first to propose that magnetic field lines can be broken and reconnected. He considered self-consistent dynamics of both field and particles at the null point and found that a small perturbation in the vicinity of a null point leads to the formation of a current sheet (introduced in next section). He considered the quiescent solar prominence to be in static equilibrium in which

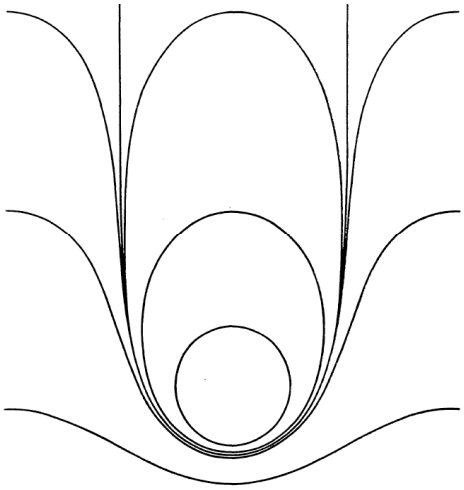

Figure 1.2: Configuration of magnetic field lines as a solution of self-consistent dynamics of magnetic field, gravitational field and particles in static equilibrium of solar atmosphere. The electromagnetic force balance the pressure gradient and gravity force, which resemble a corona magnetic loops (From the paper written by Dungey in 1953)

the electromagnetic force balances the pressure gradient and the force of gravity. A family of solutions of the magnetohydrodynamic (MHD) equilibrium problem in a conducting atmosphere in a gravitational field was obtained which resembles a filament of magnetic field and its associated coronal arches as shown in Fig. 1.2 (Dungey 1953). Two adjacent coronal magnetic loops form a configuration necessary for magnetic reconnection.

The first quantitative MHD model of magnetic reconnection after Dungey's pioneering work on the formation of current sheets was proposed by P. A. Sweet (Sweet 1958) and E. N. Parker (Parker 1957). They develop a steady-state model for reconnection which might work in a current sheet formed at a null point. Later Parker built an advanced mechanism in which he modeled the internal structure

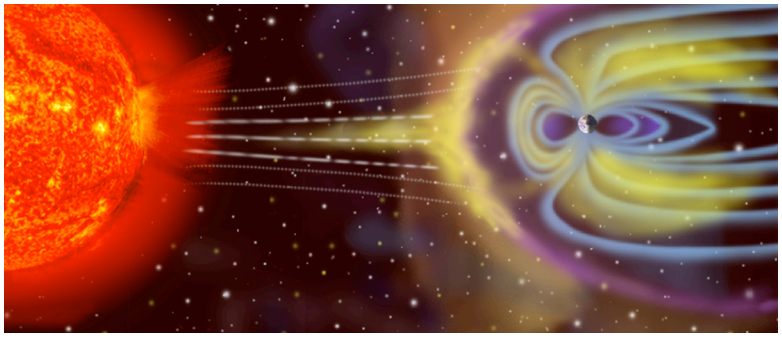

Figure 1.3: Artist's rendition of Earth magnetosphere. (Credit: Yoshi Canopus, NASA).

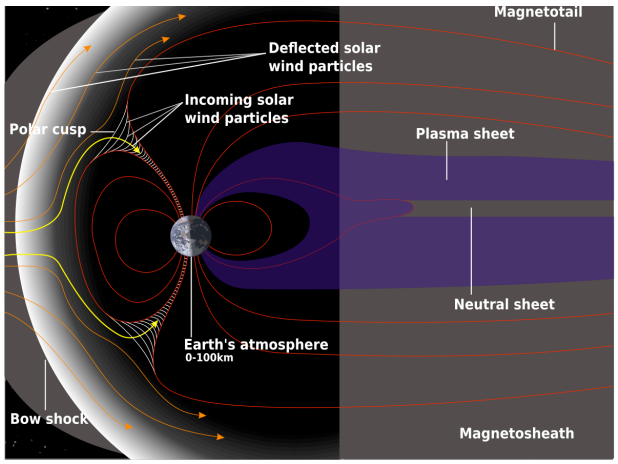

Figure 1.4: Artist's rendition of Earth magnetotail. (Credit: Aaron Kaase, NASA).

within the current sheet and included compressibility and fluid instability to enhance reconnection(Parker 1963).

The magnetic field has been identified as an important energy source for many explosive phenomena in nature such as substorms in the magnetosphere of the planets Mercury, Jupiter, Saturn, Uranus, Neptune, and Mars, and stellar flares in the magnetosphere of celestial objects, e.g. pulsar magnetosphere.

Fig. 1.3 is an artist's illustration of the magnetosphere of the Earth. The structure of the magnetosphere of the Earth is determined by a combination of

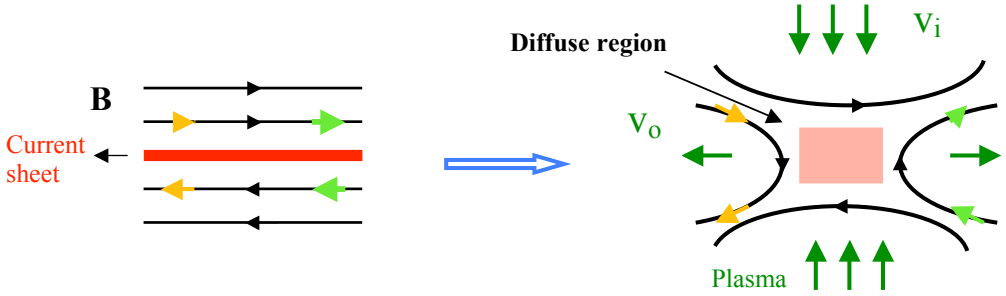

Figure 1.5: Illustration of Magnetic Reconnection

the Earth's internal magnetic field, the solar wind plasma and the interplanetary magnetic field. A magnetotail as shown in Fig. 1.4 is formed by pressure from the solar wind and extends in the anti-sunward direction far away from the Earth. Magnetic reconnection can occur in the plasma sheet and transfer energy from the solar wind to the magnetosphere, the so-called substorm.

From the examples described above, we have seen that magnetic reconnection is a crucial physical process that acts as a driver of explosions in nature. They can also occur in fusion plasmas in which this process destroys the magnetic confinement of the plasma.

Up to now, we have not discussed what magnetic reconnection is and how it is related to the release of magnetic energy in a solar flare. Magnetic reconnection is the process whereby magnetic field lines in opposite directions, separated by a thin current sheet can cross-link with one another. The patterns of connection of magnetic field lines are changed and a large amount of magnetic simultaneously energy is released as shown in Fig. 1.5.

There are important physical processes involved in magnetic reconnection that

must be identified to understand how the magnetic energy conversion takes place.

1) What is the mechanism to convert magnetic field energy into heat, and the kinetic energy of particles?

2) What is the consequence of magnetic reconnection? A resulting current sheet, large scale electric field and shock waves? How do these processes accelerate particles?

3) How does the topological change of the magnetic field configuration affect the dynamics of fast particles since these particles mainly move along field lines?

The understanding of these questions are the keys understanding magnetic reconnection.

1.2 Mechanism of Fast Magnetic Reconnection

Magnetic reconnection involves the convection and dissipation of the magnetic field. In the MHD model, this can be described by the equation:

$$\frac{\partial \mathbf{B}}{\partial t} = \nabla \times (\mathbf{v} \times \mathbf{B}) - \frac{c^2 \eta}{4\pi} \nabla \times (\nabla \times \mathbf{B}), \tag{1.1}$$

where $\frac{\eta c^2}{4\pi}$ is the magnetic diffusion rate, $\eta = (\sigma)^{-1} = \eta_e$ is the magnetic diffusivity, and σ is the electrical conductivity. If η is uniform, then

$$\frac{\partial \mathbf{B}}{\partial t} = \nabla \times (\mathbf{v} \times \mathbf{B}) + \frac{c^2 \eta}{4\pi} \nabla^2 \mathbf{B}. \tag{1.2}$$

This equation determines the magnetic field evolution in MHD once $\mathbf{v}$ is known.

If V_0 and L_0 are typical plasma velocity and magnetic field spatial length scale, the ratio of the first (convection) to second term (diffusion) on the right side

of equation (1.2) defines the magnetic Reynolds number $R_m = 4\pi L_0 V_0/(\eta c^2)$. If $R_m \ll 1$, $\mathbf{B}$ is governed by the diffusion term and the induction equation is reduced to

$$\frac{\partial \mathbf{B}}{\partial t} = \frac{c^2 \eta}{4\pi} \nabla^2 \mathbf{B}; \tag{1.3}$$

If $R_m \gg 1$, $\mathbf{B}$ is governed by the convection term and the induction equation becomes

$$\frac{\partial \mathbf{B}}{\partial t} = \nabla \times (\mathbf{v} \times \mathbf{B}). \tag{1.4}$$

In the solar corona above an active region, where $T \sim 10^6 K$, $\eta c^2/4\pi \sim 1 m^2 s^{-1}$,$L_0 \sim 10^7 m$ and $V_0 \sim 10^4 m s^{-1}$, we find $R_m \sim 10^{11}$. Thus the diffusion term in the induction equation is completely negligible. Using Faraday's equation $\nabla \times \mathbf{E} = -\frac{1}{c}\frac{\partial \mathbf{B}}{\partial t}$, equation (1.4) reduces to $\mathbf{E} + \frac{\mathbf{v}}{c} \times \mathbf{B} = 0$ which is a very good approximation in almost all of the solar atmosphere, and plasma universe. This approximation is called the MHD ideal frozen-in condition. However, η can be important in regions where the length-scale is extremely small, such as current sheets. Here $R_m \lesssim 1$, so equation 1.3 can be used in current sheets. This result is consistent with the requirement that a topology change of oppositely directed magnetic field lines requires the breaking of the ideal MHD ohm's law $\mathbf{E} + \frac{\mathbf{v}}{c} \times \mathbf{B} \neq 0$ (also called frozen-in condition), and the breaking of the frozen-in condition by electrical resistivity is the most fundamental mechanism. Equation (1.3) implies that the varied field $\mathbf{B}$ on a scale L_0 diffuse away on a time scale of $\tau_d = 4\pi L_0^2/(\eta\, c^2)$. For a sunspot with $\eta c^2/4\pi \sim 1 m^2 s^{-1}$ and $L_0 \sim 10^5 m$, the diffusion time is 3×10^2 year. This time scale is too long to explain the disappearance of sunspot in a few weeks so that the

process by which the sunspots decay can not be by diffusion.

If magnetic reconnection is responsible for the fast release of magnetic field energy in solar flares and substorms in the magnetosphere, a serious problem that remains to be understood is what mechanism drives fast magnetic reconnection if the electrical resistivity (also called Spitzer resistivity) is small? This problem has been investigated for half a century and yet has not been solved.

To understand this long-standing problem, we need to first answer two very basic questions 1) what is the steady configuration during magnetic annihilation? 2) how is the current sheet formed during magnetic reconnection? These two questions will help us to understand models of magnetic reconnection in which the length and width of current sheets play important roles.

1.2.1 Formation of a Current Sheet

In magnetic reconnection, though the magnetic field may annihilate by cancellation of inflowing oppositely directed magnetic fields, the plasma itself can not vanish and needs to flow sideways. On the other hand, a current sheet diffuses away and convert magnetic energy into joule heat. The magnetic field diffuses and spreads out at velocity $v_d = L/\tau_d = c^2\eta/4\pi L$ from the induction equation (1.2). Therefore a steady state might exist if the magnetic field and plasma come in at the same rate as the magnetic field diffuses away.

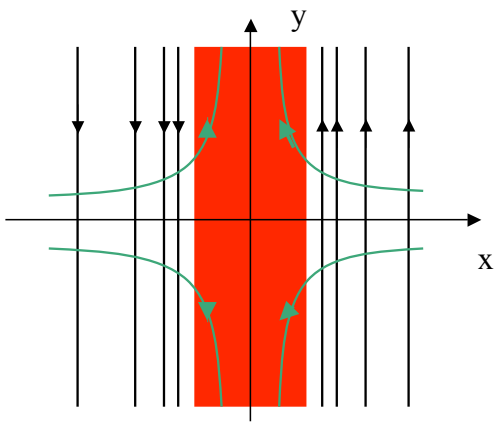

Figure 1.6: Stagnation-point flow and Creation of current sheet: the red color represent the current sheet, green lines are the streamlines and black lines are the magnetic field lines.

There are a few exact steady solutions of the MHD equations:

$$\rho\frac{d\mathbf{v}}{dt} = -\nabla p + \frac{\mathbf{j}}{c}\times\mathbf{B}, \tag{1.5}$$

$$\frac{\partial\rho}{\partial t} + \nabla\cdot(\rho\mathbf{v}) = 0, \tag{1.6}$$

$$\mathbf{E} + \frac{\mathbf{v}}{c}\times\mathbf{B} = \eta\mathbf{j}, \tag{1.7}$$

and thermal relations, where $p = \rho T/m$ is the pressure in the isotropic plasma.

We first introduce the work on stagnation-point flow by Sonnerup and Priest (Sonnerup & Priest 1975). They give a set of solutions for incompressible fluid $\nabla\cdot\mathbf{v} = 0$. A stagnation flow is

$$v_x = -v_0 x/a, \qquad v_y = v_0 y/a, \tag{1.8}$$

where a and v_0 are constant. The streamlines of plasma flow as shown in Fig. 1.6 by green lines are the rectangular hyperbolae ($xy = constant$) and cross the straight lines of magnetic field with $\mathbf{B} = B(x)\hat{y}$ (denoted by black lines).

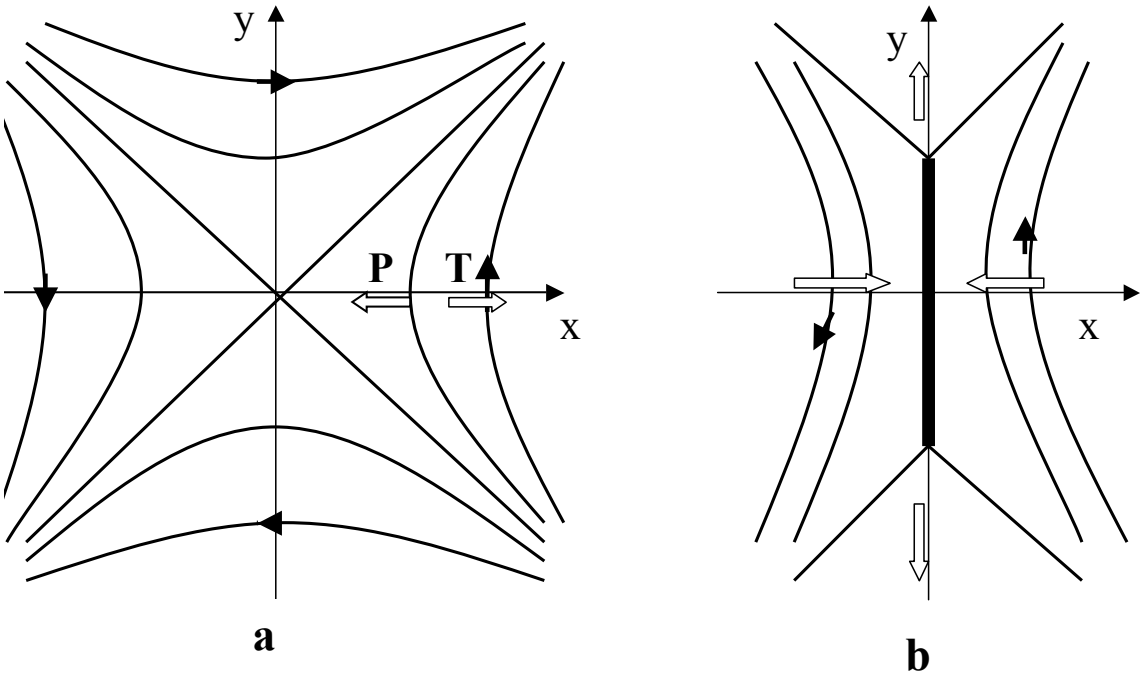

Figure 1.7: Collapse of X-Point and Creation of current sheet.

In Ohm's law $\mathbf{E} + \frac{\mathbf{v}}{c} \times \mathbf{B} = \eta \mathbf{j} = \frac{c\eta}{4\pi} \nabla \times \mathbf{B}$, both $\mathbf{v} \times \mathbf{B}$ and $\nabla \times \mathbf{B}$ are in the z direction, thus $\mathbf{E} = E(x, y)\hat{z}$. $\nabla \times \mathbf{E} = 0$ implies that $E = constant$.

Then we have the equation of magnetic field :

$$E - v_0 x B/ac = \frac{c\eta}{4\pi} \partial B/\partial x. \tag{1.9}$$

We can have two limits of B for $x \longrightarrow \infty$ and $x \longrightarrow 0$: $B \approx caE/v_0 x$ and $B = 4\pi Ex/c\eta$, respectively. The magnetic field lines are frozen to the plasma and are driven inwards at large x and diffuse through the plasma at small x. The half width of the current sheet can be estimated by equating the two solutions of B to obtain $x = \sqrt{a\eta/4v_0}$. The plasma pressure can be determined from the conservation of energy $p + B^2/8\pi + \frac{\rho v^2}{2} = constant$ which is derived from the steady equation of motion of incompressible fluid.

Another way of forming a current sheet is through the collapse of an x-point. In a cold plasma, the MHD equation of motion reduces to

$$\rho\frac{d\mathbf{v}}{dt} = \frac{\mathbf{j}}{c} \times \mathbf{B}, \tag{1.10}$$

thus the simplest steady state is $\mathbf{j} \times \mathbf{B} = 0$, where $\mathbf{j} \times \mathbf{B} = \frac{c}{4\pi}(\mathbf{B} \cdot \nabla)\mathbf{B} - \bigtriangledown\frac{B^2}{2})$. Magnetic pressure force ($\bigtriangledown P = \bigtriangledown\frac{B^2}{2}$) is balanced by magnetic tension ($T = (\mathbf{B} \cdot \nabla)\mathbf{B}/4\pi$). An X-type null point configuration satisfies:

$$B_x = y, \qquad B_y = x, \tag{1.11}$$

and electric current $\mathbf{j} = c(\partial B_x/\partial x - \partial B_y/\partial y)/4\pi = 0$, thus $P = T$ everywhere as shown in Fig. 1.7 (a).

However, we expect an inward force in the x direction if the force due to magnetic pressure is larger than the magnetic tension (smaller curvature of magnetic field lines) and outward force in the y-direction if the magnetic tension is larger (larger curvature of field lines) as shown in Fig. 1.7 (b). Suppose the distorted magnetic field is $B_x = y$ and $B_y = Ax$, where $A > 1$. The corresponding field lines satisfy the equation $y^2 - Ax^2 = constant$ as sketched in Fig. 1.7 (b) and the electric current $\mathbf{j} = c(A-1)/4\pi$. The magnetic force is:

$$\mathbf{j} \times \mathbf{B} = -\frac{c(A-1)Ax}{4\pi}\hat{x} + \frac{c(A-1)y}{4\pi}\hat{y}. \tag{1.12}$$

which are denoted by the big arrows in Fig. 1.7 (b). The formation of a current sheet causes the configuration to be unstable.

We have given two examples of the formation of a current sheet, but none of them allow steady magnetic reconnection. Priest (Priest & Forbes 2000) proved

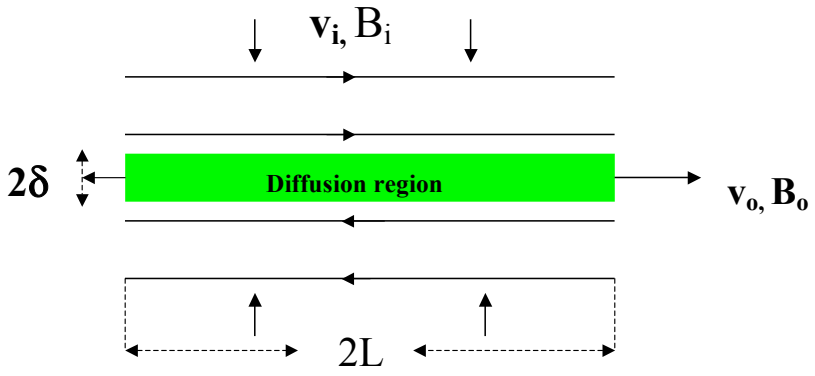

Figure 1.8: Sweet-Parker model

that 2D incompressible linear reconnection is impossible. This theorem implies that reconnection requires the flow speed to be Alfvenic somewhere so that the process become nonlinear as discussed in the next section.

1.2.2 MHD Model: From Sweet-Parker To Petschek Model

The crucial first step on fast magnetic reconnection was made by Sweet and Parker (Sweet 1958; Parker 1957). They showed that the conversion of magnetic energy could be much faster than the resistive decay rate because of the formation of current sheets. It was realized that resistive processes would lead to a change of topology of lines and that a change of topology can be produced by magnetic reconnection in small region.

The Sweet-Parker model (Fig. 1.8) consists of a current sheet with length $2L$ and width 2δ between oppositely directed fields. Suppose the input flow speed is v_i and magnetic field is B_i; the outflow speed is v_o and magnetic field is B_o. What are the relations between v_i and v_o, B_i and B_o? How fast does the plasma enter

the diffusion region, i.e, what is v_i? How large is the outflow speed v_o? What is the ratio of magnetic energy to the inflowing kinetic energy? How much magnetic energy is converted into kinetic energy? How long is the reconnection time scale?

Conservation of the mass of the incompressible fluid implies that the rate at which mass enters the current sheet must equal the rate at which the mass leaves the reconnection region, thus we have

$$Lv_i = \delta v_o. \tag{1.13}$$

Steady state reconnection requires that the plasma must carry the field line into the diffusion region at the same speed at which plasma diffuses away. The induction equation give us

$$v_i = \eta c^2/4\pi\delta. \tag{1.14}$$

The electric current sheet $\mathbf{j} = c(\nabla \times \mathbf{B})/4\pi \approx cB_i/(4\pi\delta)\hat{z}$ and so the Lorentz force along the sheet is $|\frac{\mathbf{j}}{c} \times \mathbf{B}| \approx jB_o/c\hat{y} = B_iB_o/(4\pi\delta)\hat{y}$. The force accelerates the plasma from the rest at the neutral point to v_o over a distance L. In steady state equation(1.10) reduces to $\rho\mathbf{v}\cdot\nabla v_x = B_iB_o/(4\pi\delta)$. Thus we have the scaling relation

$$\rho\frac{v_o^2}{L} \approx B_iB_o/4\pi\delta, \tag{1.15}$$

From $\nabla \cdot \mathbf{B} = 0$,

$$B_o/\delta = B_i/L, \tag{1.16}$$

then

$$v_o^2 = B_i^2/4\pi\rho \equiv c_A^2, \tag{1.17}$$

where c_A is the Alfven speed at the inflow. The magnetic force accelerates the plasma to the Alfven speed.

We can also obtain $v_i = \delta c_A/L = \sqrt{\eta c^2 c_A/4\pi L}$. This result indicates that $v_i \ll c_A$ for $\delta \ll L$ and the width of current sheet is controlled by the resistivity $\delta = \sqrt{\frac{c^2 L\eta}{4\pi c_A}}$. The inflowing electromagnetic energy w_{iem} is the poynting flux $c\mathbf{E}\times\mathbf{B}/4\pi$, and $E = v_i B_i/c$. Thus $w_{iem} = LEB_i/4\pi = v_i L B_i^2/4\pi$, and therefore the ratio of the inflowing kinetic energy w_{ik} to magnetic energy is

$$\frac{w_{ik}}{w_{iem}} = \frac{\frac{1}{2}\rho v_i^2 (v_i L)}{v_i L B_i^2/4\pi} = \frac{v_i^2}{2c_A^2} \ll 1. \tag{1.18}$$

Most of the inflowing energy is magnetic.

The conservation of magnetic flux gives us $v_o B_o = v_i B_i$, so $B_o = \frac{v_i}{c_A} B_i \ll B_i$. Similarly the ratio of outflowing kinetic energy w_{ok} to inflowing magnetic energy is

$$\frac{w_{ok}}{w_{iem}} = \frac{\frac{1}{2}\rho v_o^2 (\delta v_o)}{v_i L B_i^2/4\pi} = \frac{v_o^2}{2c_A^2} = \frac{1}{2}. \tag{1.19}$$

Thus half of the inflowing magnetic energy is converted into kinetic energy and the other half is converted to Ohmic heat.

The time of reconnection is of the order $\tau_r \sim L/v_i = L\sqrt{R_m}/c_A$, where $R_m = 4\pi L c_A/c^2\eta$ is the magnetic Reynolds number. Compared to the resistive decay time $\tau_d = LR_m/c_A$, the reconnection rate is of $\sqrt{R_m}$ times faster. However, compared to the energy release time scale in nature, it is still too slow. Here is an example from a solar flare (Kulsrud 2005, 2001): $B = 300$ G, $\rho = 10^{-15}$ gm/cm ^{3}, $c_A = 2.7\times 10^9$ cm/s, $L = 10^9$ cm, $R_m = 2.7\times 10^{14}$, dynamic time $L/c_A = 0.37$ s, then the resistive decay time $\tau_d = 10^{14}$ s $= 3.2\times 10^6$ years and the Sweet-Parker reconnection time is $\tau_r = 6.1\times 10^6$ s $= 2.4$ months. The typical solar flare duration is 15 min to 1 h.

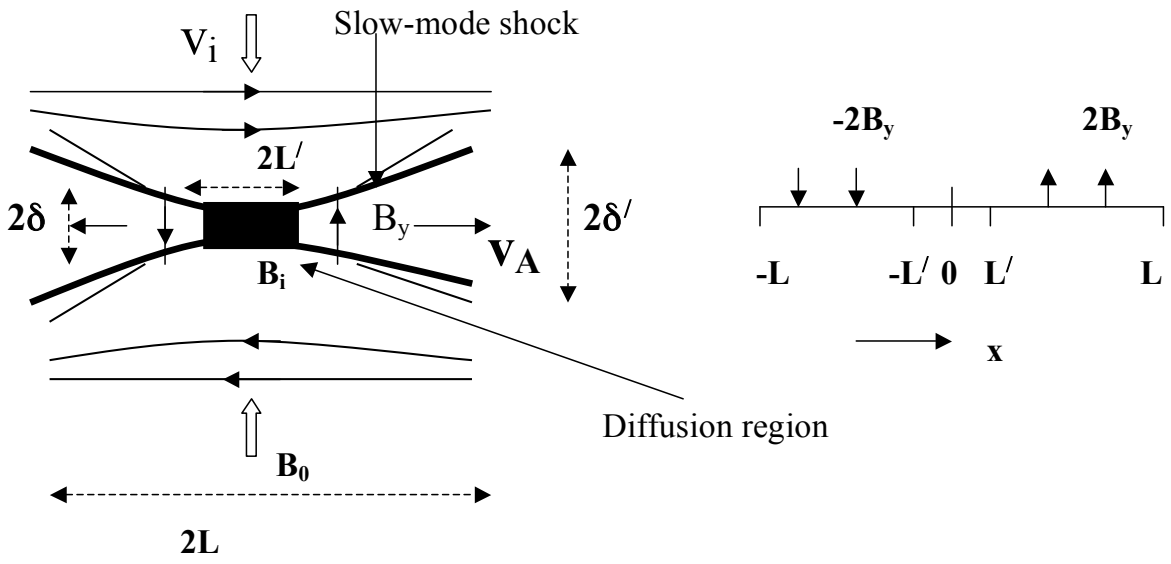

Figure 1.9: Left: Petschek model. The dark lines are shocks across which the plasma is accelerated to v_A in the x direction. Right: Magnetic field in the inflow region.

Petschek developed a model in which the reconnection rate only depends logarithmically on the resistivity η which significantly decreases the reconnection time scale (Petschek 1964). The maximum reconnection inflow speed is $v_i = \frac{\pi c_A}{8 ln R_m}$. For our example above, the reconnection time scale is 20 s.

Petscheck observed that the heart of the Sweet-Parker model is the current layer which is responsible for reconnecting field lines. The reconnection rate depends on the ratio of the width and length of the current layer. He wondered if dissipation could be restricted to a very small region of the layer $L^{'} \ll L$ and the plasma could fan out to a cross section $\delta^{'} \gg \delta$ with flow speed c_A (Fig. 1.9). Then the reconnection inflow speed could be increased to $v_i = c_A \delta^{'}/L^{'}$ (from the mass conservation).

Petschek's regime is "almost uniform". In the inflow region, the magnetic field B_y is a small perturbation to the magnetic field B_0 and the current is small. Most

of the energy conversion takes place at the standing slow-mode shock. These shock waves accelerate and heat the plasma.

Petschek estimated the maximum reconnection speed by assuming $B_i = B_0/2$, then

$$v_i = \pi c_A / 8 ln R_m. \tag{1.20}$$

Great efforts have been devoted to rigorously establish Petschek's model for fast reconnection (Priest & Forbes 1986; Yeh & Axford 1970; Sato & Hayashi 1979; Uzdensky & Kulsrud 2000). However, the Petscheck solution is not obtained in simulations. Several numerical simulations (Cowley 1975; Biskamp 1986; Scholer 1989; Biskamp 1994; Ugai 1995) have shown that simple, two dimensional systems will reach the Sweet-Parker solution for low inflow rates. At higher rates, the simulations find a transition to unsteady behavior, rather than a transition to the Petschek mode. In addition, recent lab work which was configured explicitly to measure reconnection physics seems to support the Sweet-Parker model (Ji et al. 1998; Kulsrud 1998, 2001).

1.2.3 Non-MHD Reconnection

MHD models have difficulty in explaining fast reconnection. The width of the current layer δ is controlled by resistivity while the length of current layer is linked to the macroscopic system scale length, independent of the dissipation processes. However, it was discovered that the motion of the electrons and ions decouple at small spatial scales, and that two distinct ion and electron diffusion regions develop

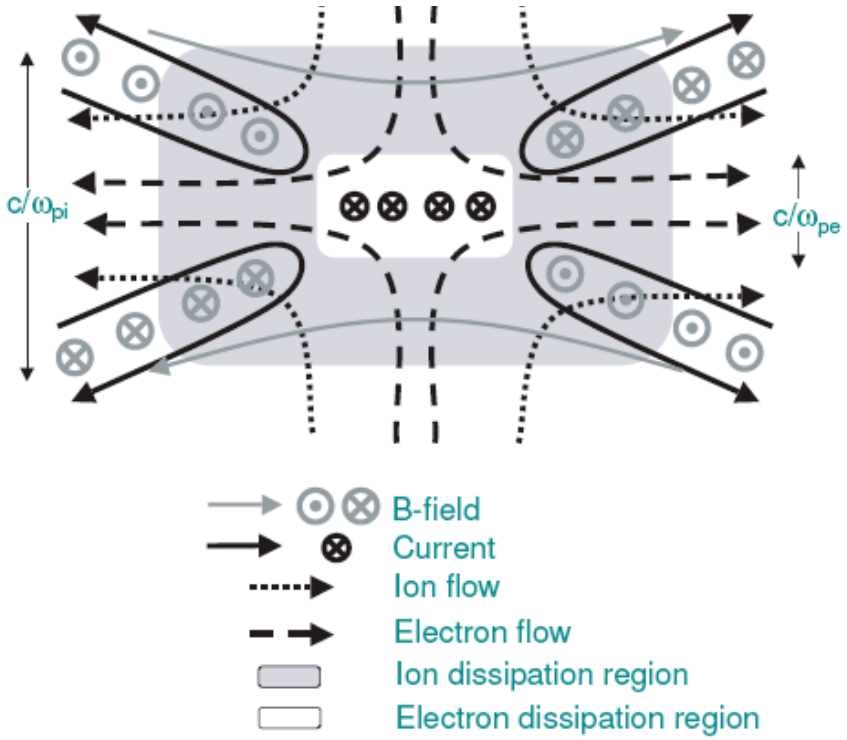

Figure 1.10: Schematic of multiscale structure of the dissipation region during anti-parallel reconnection. Electron (ion) dissipation region in white (gray) with scale size c/ω_{pe} (c/ω_{pi}). Electron (ion) flows in long (short) dashed lines. In-plane current marked with solid solid dark lines and associated out-of-plane magnetic quadrupole field in gray. (From the paper by Drake & Shay (Birn & Priest 2007))

(Fig 1.10)(Sonnerup & Ledley 1979; Mandt et al. 1994; Horiuchi & Sato 1994). This discovery provided a new insight into the magnetic reconnection mechanism that requires non-MHD dynamics. In addition, the observations of large number of energetic electrons during solar flares (Lin & Hudson 1971; Miller 1997) and high-energy tails on the particle distributions observed in magnetotail (Øieroset et al. 2002) indicate that kinetic dynamics is required to understand reconnection because heating processes can only be treated with a kinetic model.

The new dynamics is investigated by the electron equation of motion,

$$m_e \frac{dv_e}{dt} = -e\mathbf{E} - e\frac{\mathbf{v}_e}{c} \times \mathbf{B} - \frac{1}{n_e}\nabla \cdot \mathbf{P}_e - m_e \nu_{ei}(\mathbf{v}_e - \mathbf{v}), \tag{1.21}$$

where $\mathbf{v}$ is the bulk ion velocity, $\mathbf{P}_e$ is the electron pressure tensor. This equation can be rewritten as an Ohm's-law if $\mathbf{v}_e$ is replaced with $\mathbf{v}_e = \mathbf{v} - \mathbf{j}/ne$ and terms of order m_e/m_i are neglected,

$$\frac{m_e}{n_e e^2}\left[\frac{\partial \mathbf{j}}{\partial t} + \nabla \cdot (\mathbf{j}\mathbf{v} + \mathbf{v}\mathbf{j})\right] = \mathbf{E} + \frac{\mathbf{v}}{c} \times \mathbf{B} - \frac{\mathbf{j} \times \mathbf{B}}{n_e e} + \frac{1}{n_e e}\nabla \cdot \mathbf{P}_e - \eta \mathbf{j}. \tag{1.22}$$

Equation (1.22) is called the generalized Ohm's law. It contains three new terms that are not present in the resistive MHD Ohm's law, the electron inertia term on the left of equation (1.22), the Hall term ($\frac{\mathbf{j}}{c} \times \mathbf{B}$) and the electron pressure. The Hall term brings in whistler waves and the electron pressure brings in kinetic Alfven waves. The inertial term is associated with the electron skin length $d_e \equiv c/\omega_{pe}$. Comparing the Hall term with $\mathbf{v} \times \mathbf{B}$, the Hall term dominates when

$$\frac{|\mathbf{v}}{c} \times \mathbf{B}| \sim c_A B < \frac{|\mathbf{j} \times \mathbf{B}|}{c n_e e} \sim \frac{1}{4\pi n_e e}\frac{B^2}{\delta}, \tag{1.23}$$

or

$$\delta < d_i \equiv c/\omega_{pi}. \tag{1.24}$$

If $\delta < d_i$, $j/n_e e > v$ so that $v_e > v$ which means that electrons and ions decouple and no longer move together. In the MHD regime, $v_e \sim v$ and MHD equation are scale invariant which means MHD equations do not define a specific spatial scale. The isotropic pressure term brings in the effective ion Larmor scale $\rho_s = \sqrt{T_e/m_i}/\Omega_i$ based on the ion-sound speed, $v_s = \sqrt{T_e/m_i}$ for $T_e \gg T_i$.

The generalized Ohm's law was investigated systematically by the *GEM Reconnection Challenge* collaborations (Birn et al. 2001). One important result was that the rate of the late-time reconnection was insensitive to dissipation when whistler and kinetic Alfven waves drive the outflow from the x-line (Shay & Drake 1998; Hesse et al. 1999). The whistler wave plays an important role in anti-parallel reconnection while the kinetic Alfven wave dominates in guide-field reconnection, in which an initial magnetic field is perpendicular to the reconnection plane.

1.2.3.1 Anti-parallel Reconnection

Replacing the ideal MHD Ohm's law $\mathbf{E} + \frac{\mathbf{v}}{c} \times \mathbf{B} = 0$ by equation (1.22), the generalized Ohm's law, we can calculate the dispersion relation of waves propagating perpendicularly to the reconnection magnetic field B_x(Wang et al. 2000; Rogers et al. 2001),

$$\omega^2 = \frac{k_y^2 c_{Ay}^2}{D}(1 + \frac{k_y^2 d_i^2}{2D} + \sqrt{\frac{k_y^2 d_i^2}{D} + \frac{k_y^4 d_i^4}{4D^2}}), \tag{1.25}$$

where we have approximated the magnetic field $\mathbf{B}_0 = B_{y0}\hat{y}$ in the outflow region. $D = 1 + k_y^2 d_e^2$, $c_{Ay} = B_{y0}/\sqrt{4\pi m_i \rho_0}$.

This dispersion relation is dispersive. For long wavelength $k_y d_i \ll 1$, the equation reduces to $\omega^2 = k_y^2 c_{Ay}^2$, which is the Alfven wave. For intermediate wavelengths $k_y d_e \ll 1 \ll k_y d_i$, the dispersion relation gives $\omega = k_y^2 c_{Ay} d_i$, which is the whistler wave. For very short wavelength $k_y d_e \gg 1$, it reduces to the electron cyclotron wave with frequency $\omega = eB_{y0}/cm_e$. Whistler wave causes the quadrupole structure of reconnection region as shown in Fig. 1.10. The electrons decouple from the

magnetic field when they approach within d_e of the x-line and are accelerated in the outflow direction. The peak outflow velocity of electrons reaches the electron Alfven speed $v_{Ae} = B/\sqrt{4\pi m_e n_e}$ and then drops quickly to match the ion outflow speed c_A. The current loops in the reconnection plane caused by the different trajectories of the electrons and ions generate a self-consistent out-of-plane magnetic field B_z. B_z is the signature of standing whistler wave that drives the electron out-flow from the x-line. The width of electron diffusion region can be estimated by the electron Larmor radius $\delta_e = \sqrt{\frac{v_{te}}{\Omega'_{ex}}}$, based on the asymptotic magnetic field, where v_{te} is the electron thermal velocity and $\Omega_{ex} = eB_0x/m_e$ is the electron cyclotron frequency and $\Omega'_{ex} = \partial\Omega_{ex}/\partial x$ (Laval et al. 1966). In the high temperature reconnection, the width of the current sheet is $\delta_e > d_e$, where $d_e = c/\omega_{pe}$, the electron skin length. In the low temperature reconnection, $v_{te} \sim v_{Aex} = \sqrt{\frac{B_x^2}{4\pi n m_e}}$, and the width of the current sheet is of the order $\delta_e \sim d_e$ (Zeiler et al. 2002).

Compared to the MHD model, the reconnection rate of the kinetic model is much larger and also is insensitive to the mechanism that breaks the frozen-in condition. The results from the GEM project are shown in Fig. 1.11. The reconnected flux versus time is shown for simulations with the MHD model, the Hall model (generalized Ohm's law), the hybrid model (massless fluid electrons and particle ions) and a PIC model. Except for the MHD model, all others include the dynamics of the whistler wave and were run with the same initial set-up. The slope of the curve of reconnection flux is the reconnection rate. All models but MHD have almost indistinguishable rates and greatly exceed the MHD rate.

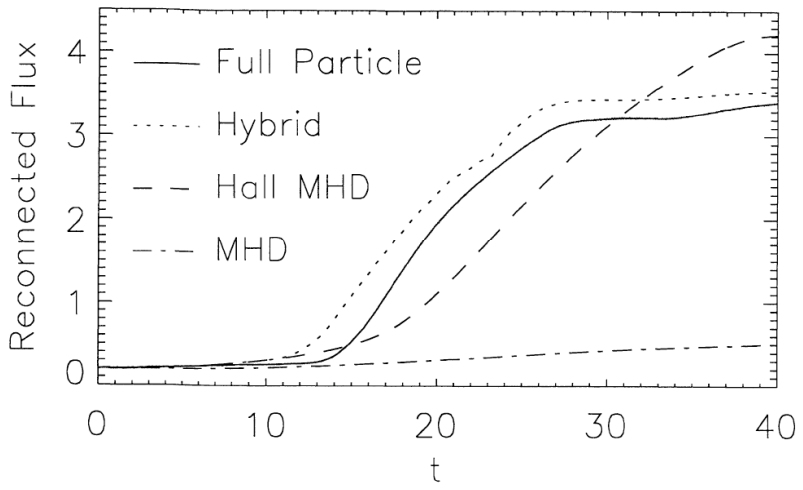

Figure 1.11: Reconnection magnetic flux versus time for various simulation model (From the paper by Birn et al. (Birn et al. 2001))

1.2.3.2 Guide Field Reconnection

The guide field is in the out-of-plane direction, along the direction of current. The structure of diffusion region formed in guide field reconnection (Fig. 1.12) is significantly different from the diffusion region formed in anti-parallel reconnection. The diffusion region in guide field reconnection is controlled by the kinetic Alfven wave (Aydemir 1992; Kleva et al. 1995; Cafaro et al. 1998). Unlike in anti-parallel reconnection, waves with a guide field are compressible, the density fluctuation is non-zero and the pressure becomes important. The generalized Ohm's law yields a dispersion relation $\omega^2 = \frac{k_y^2 c_{Ay}^2}{D}(1+\frac{k_y^2\rho_s^2}{1+\beta D})$, where v_s is the sound speed, $\rho_s = v_s/\Omega_i$ and $\beta = v_s^2/c_A^2 \ll 1$. Similar to anti-parallel reconnection, for long wavelength $k_y\rho_s \ll 1$, the dispersion relation reduces to that of the Alfven wave with $\omega^2 = k_y^2 c_{Ay}^2$. For

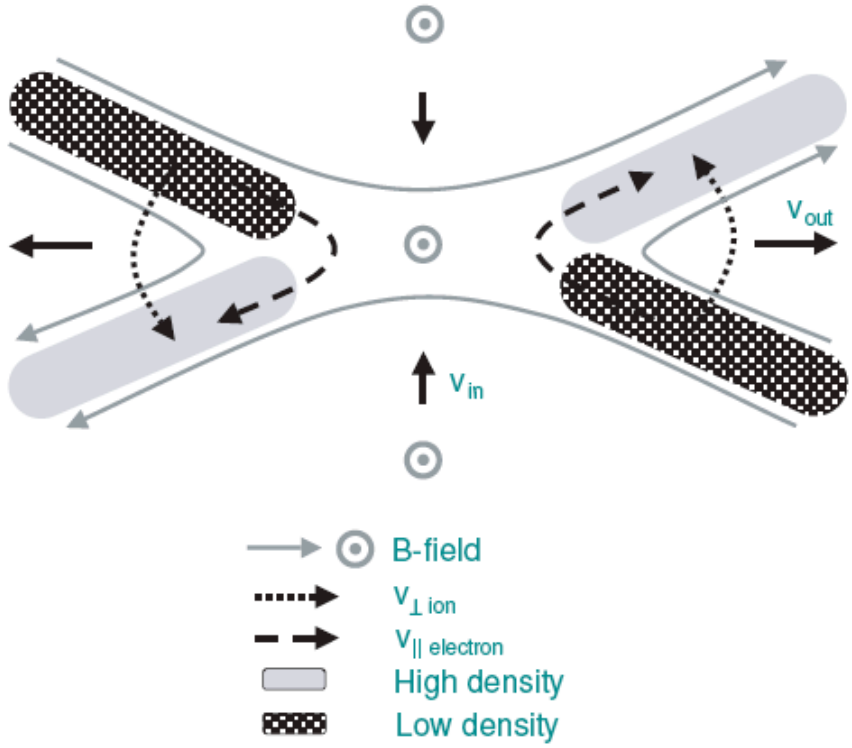

Figure 1.12: Schematic of structure of the dissipation region during reconnection with a guide field. Compression of parallel electron flows on newly reconnected field lines lead to a density asymmetry across the dissipation region in contrast to the symmetric system with no guide field. Ion polarization drift across the magnetic field to charge neutralize the electrons.(From the paper by Drake & Shay (Birn & Priest 2007))

intermediate wavelength $k_y d_e \ll 1 \ll k_y \rho_s$, it describes the kinetic Alfven wave with $\omega = k_y^2 c_{Ay} \rho_s$, which is dispersive. For short wave $k_y d_e \gg 1$, it reduces to the electron cyclotron wave as in the non-MHD reconnection without guide field. In guide field reconnection non-MHD effects become important at the length scale ρ_s.

A signature of the Alfven wave is the density asymmetry along the separatrices: the depletion of the density along two of the separatrices and enhancements along the remaining (Kleva et al. 1995; Tanaka 1996; Pritchett & Coroniti 2004; Drake et al. 2005). The guide field suppresses the unmagnetized bounce motion of electrons that controls the width of the electron current layer in anti-parallel reconnection. The resulting current sheet narrows substantially with a width close to electron Larmor radius (Hesse et al. 2002, 2004). The additional magnetic field also prevents the electrons from escaping from the x-line and the inductive electric field parallel to the magnetic field drives strong out-of-plane current because of the resulting acceleration of electrons.

1.3 Importance of Anomalous Resistivity in Fast Magnetic Reconnection

Anomalous resistivity can be induced by turbulent dissipation. This was proposed as a potential physical process to explain the sudden decrease of the conductivity observed in space plasma and fusion experiments when the electric currents pass through the plasma with very low density (Davidson & Gladd 1975; Papadopoulos & Palmadesso 1976; Galeev & Sagdeev 1984a). Anomalous resistivity is related to

the kinetic process in which the collective interactions of waves and particles effectively transfer the kinetic energy and electromagnetic energy into thermal energy. For this reason, anomalous resistivity also was regarded as a mechanism to enhance the rate of the reconnection. However, the establishment and the role of turbulence in magnetic reconnection is not yet well understood because highly complicated nonlinear microscopic physical processes are involved and its effect in experiments and observations is difficult to quantify.

In recent years, *in situ* observations in space plasma reveal that magnetic reconnection is associated with turbulence (Cattell et al. 1999; Farrell et al. 2002; Matsumoto et al. 2003; Cattell et al. 2005; Retinò et al. 2007; Sundkvist et al. 2007; Teste & Parks 2009) while experiments of magnetic reconnection also showed that strong turbulence appears together with reconnection (Ji et al. 1998; Yamada et al. 2000; Carter et al. 2002; Ji et al. 2004; Fox et al. 2008). Fig. 1.13 is the small-scale magnetic reconnection at the Earth's magnetosphere seen by Cluster(Retinò et al. 2007). Reconnection observed in such a turbulent environment implies that both turbulence and reconnection develop together.

The role of non-MHD waves in fast reconnection has been extensively investigated by simulations as introduced in the section 2. It is found that the rate of fast magnetic reconnection is insensitive to the mechanism of dissipation. However, the experiment MRX discovered a positive correlation between the magnitude of the electromagnetic fluctuations and the enhancement of the reconnection rate in a well-controlled laboratory plasma (Ji et al. 2004). These contradictory conclusions have not been resolved.

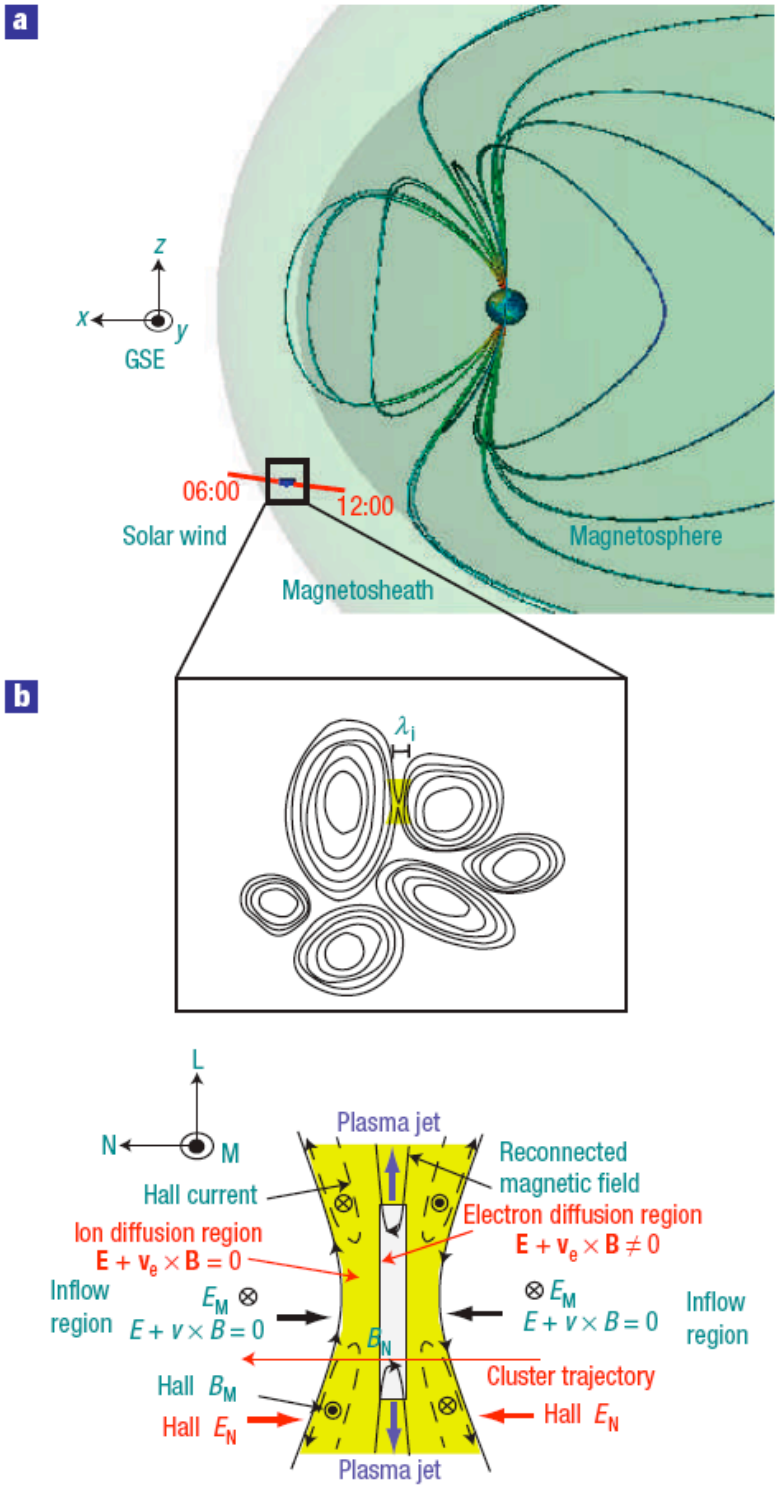

Figure 1.13: The quasi-parallel bow-shock crossing. **a**, Spacecraft orbit (red line). **b**, Schematic diagram of the current-sheet formation between magnetic islands and of magnetic reconnection in the current sheet. GSE: geocentric solar ecliptic coordinate system. CLUSTER observation (Retinò et al. 2007).

In space it is observed that energetic particles are produced during the magnetic reconnection (Øieroset et al. 2002; Imada et al. 2007; Retinò et al. 2007). The acceleration of particles requires the efficient energy transformation among magnetic energy, convective kinetic energy and thermal energy. Turbulence can enhance the energy dissipation and diffusion but how turbulence impacts reconnection is not well understood.

The study of turbulence in reconnection is a broad topic. It touches the fundamental physics of both turbulence and reconnection. Microscopic instabilities are common in space plasma and experiments and they can trigger turbulence. The related wave-particle interactions play an important role in energy transport, particle diffusion and particle acceleration. These problems have been studied extensively by quasi-linear kinetic theory and achieved fruitful results (Galeev & Sagdeev 1984a,b). The quasi-linear kinetic theory is based on the assumption that the wave frequency ω is much larger than its growth rate γ and that trapping of the particles can be neglected, which is valid if the wave perturbation is infinitely small and its spectrum is sufficiently broad. However, in many cases of instabilities occurring in space and experiments, these assumptions are not satisfied. In particular when the instabilities approach their saturation, the trapped particles and waves often have a strong interaction. In such situations, the quasi-linear theory becomes invalid and the nonlinear theory has not been formulated that can describe large perturbations.

In my thesis, I will focus on the nonlinear development of streaming instabilities, which are very common in space plasma and also are observed during reconnection in space (Cattell et al. 1999; Farrell et al. 2002; Matsumoto et al. 2003; Cattell

et al. 2005; Teste & Parks 2009). I aim to combine both simulations and analytic methods to investigate this complex nonlinear process in which amplitude of the perturbation is large and the growth rate of instabilities can be faster than the wave frequency. My thesis is organized as follows: Chapter II introduces the streaming instabilities from both linear fluid and kinetic theory; Chapter III discusses the Buneman instability in reconnection; Chapter IV focus on the nonlinear development of streaming instabilities; Chapter V addresses the nonlinear development of streaming instabilities in reconnection and Chapter VI presents the conclusions and discussions.

Chapter 2

Linear Kinetic Theory of Streaming Instabilities in Magnetized Plasma

Streaming instabilities are common in space and experimental plasma. They are driven by the relative drift between particles. The instabilities caused by the drift between ions and electrons are called ion-electron two-stream instabilities. In particular, if the electron temperature is close to that of the ions, and the electron drift relative to ions is larger than the electron thermal velocity, the instability is called Buneman instability. The ion acoustic instability, which can exist at low drift speeds, is stable for typical heliospheric plasmas where $T_i \geq T_e$. The instability caused by the relative drift between electrons is the electron-electron two stream instability. The lower hybrid instability often accompanies the Buneman instability in magnetized plasmas, which is nearly-perpendicular to the magnetic field. In this chapter, these instabilities are approached from both the kinetic and cold plasma limit.

In the kinetic approach, the particles are considered to interact and exchange energy with waves. The amplitude of a wave with a particular phase speed decreases when there are more particles interacting with the wave with velocity slower than the wave phase speed. This resonance is called Landau-damping. The amplitude of a wave with a particular phase speed increases when there are more particles inter-

acting with waves with velocity faster than the wave phase speed. This collective resonance between wave-particles is called inverse-Landau damping.

The plasma is called cold plasma when the plasma pressure can be neglected, i.e in the homogenous plasma the electrons satisfy the condition: $\sqrt{kT/m_e} \ll \omega/k$ so that the thermal velocity of electrons is much smaller than the phase speed of the wave. In a cold plasma, all of the particles at a given position move with the same velocity and can be treated as a fluid. The fluid velocity v is the mean velocity of the particles: $\mathbf{v} = \int \mathbf{v} f_j(v,x,t)dv / \int f_j(v,x,t)dv$ where j is the species of particles.

2.1 Cold Plasma Description of Streaming Instabilities in Unmagnetized Plasma

2.1.1 Buneman Instability

The Buneman instability has been studied for more than half of century since it was first discovered by Oscar Buneman, a pioneer of plasma physics and plasma simulation (Buneman 1958). He found that the mechanism of the Buneman instability was the familiar electron-electron two-stream amplification which was discovered earlier (Pierce & Hebenstrett 1949; Pierce 1949; Haeff 1949; Nergaard 1948). The collective Coulomb interactions cause instabilities which grow so rapidly that the relative motions of electrons and ions, i.e., current, are continuously damped down by conversion of directed energy into fluctuation (random) energy. The dispersion relation of this instability was derived from the two-fluid momentum equations in a

homogenous non-magnetized plasma,

$$m_e(\frac{\partial \mathbf{v}_e}{\partial t} + \mathbf{v_e} \cdot \nabla \mathbf{v}_e) = -e\mathbf{E}, \tag{2.1}$$

$$m_i(\frac{\partial \mathbf{v}_i}{\partial t} + \mathbf{v_i} \cdot \nabla \mathbf{v}_i) = e\mathbf{E}, \tag{2.2}$$

the equations of continuity and Poisson's equation:

$$\frac{\partial n_e}{\partial t} + \nabla \cdot (n_e \mathbf{v}_e) = 0, \tag{2.3}$$

$$\frac{\partial n_i}{\partial t} + \nabla \cdot (n_i \mathbf{v}_i) = 0, \tag{2.4}$$

$$\nabla \cdot \mathbf{E} = 4e\pi(n_i - n_e), \tag{2.5}$$

where n_e and n_i are the electron and ion densities, and v_e and v_i are the electron and ion fluid element velocities.

Assuming the zero-order electric field $\mathbf{E}_0 = 0$, initial density is homogenous $n_e = n_i = n_0$, initial ion drift $\mathbf{v}_{i0} = 0$, initial electron drift $\mathbf{v}_e = \mathbf{v}_{de}$, and the first-order quantities $\delta\mathbf{E}$, $\delta n_{e,i}$ and $\delta v_{e,i}$ vary as $e^{i(\mathbf{k}\cdot\mathbf{r}-\omega t)}$, the linearized equations of the cold fluid and continuity take the forms:

$$im_e(\mathbf{k} \cdot \mathbf{v}_{de} - \omega)\delta\mathbf{v}_e = -e\mathbf{E}, \tag{2.6}$$

$$-im_i\omega\delta\mathbf{v}_i = e\mathbf{E}, \tag{2.7}$$

$$(\mathbf{k} \cdot \mathbf{v}_{de} - \omega)\delta n_e + n_0\mathbf{k} \cdot \delta\mathbf{v}_e = 0, \tag{2.8}$$

$$-\omega\delta n_i + n_0\mathbf{k} \cdot \delta\mathbf{v}_i = 0, \tag{2.9}$$

and Poisson's equation takes the form,

$$i\mathbf{k} \cdot \mathbf{E} = 4\pi e(\delta n_i - \delta n_e). \tag{2.10}$$

From these we obtain

$$\mathbf{v}_e = \frac{ie\delta\mathbf{E}}{m_e(\mathbf{k}\cdot\mathbf{v}_{de} - \omega)}, \tag{2.11}$$

$$\mathbf{v}_i = \frac{-ie\delta\mathbf{E}}{m_i\omega}, \tag{2.12}$$

and

$$\delta n_e = \frac{n_0\mathbf{k}\cdot\delta\mathbf{v}_e}{\omega - \mathbf{k}\cdot\mathbf{v}_{de}}, \tag{2.13}$$

$$\delta n_i = \frac{n_0\mathbf{k}\cdot\delta\mathbf{v}_i}{\omega}. \tag{2.14}$$

We substitute these relations of the first-order quantities into the linearized Poisson's equation and rearrange them in the form $D\mathbf{E} = 0$, where D is the dielectric permittivity tensor. Using $\mid D \mid = 0$, the necessary and sufficient condition for the existence of real roots for this group of linear equations, we obtain the cold plasma dispersion relation for Buneman instability in a non-magnetized plasma:

$$y \equiv \frac{\omega_{pi}^2}{\omega^2} + \frac{\omega_{pe}^2}{(\omega - \mathbf{k}\cdot\mathbf{v}_{de})^2} = 1, \tag{2.15}$$

where $\omega_{pe} = \sqrt{4\pi n_0 e^2/m_e}$, the electron plasma frequency and $\omega_{pi} = \sqrt{4\pi n_0 e^2/m_i}$, the ion plasma frequency.

Defining $y(x)$ ($x = \omega/\omega_{pe}$), we plot $y(x)$ with different values of the parameters $\beta_z = \mathbf{k}\cdot\mathbf{v}_{de}/\omega_{pe}$ and $\alpha = \omega_{pi}^2/\omega_{pe}^2 = m_e/m_i$ in Fig. 2.1. We see that the black line ($y = 1$) is tangent to the green line with $\beta_z = 1.13$ at $\omega/\omega_{pe} \sim 0.1$ and intersects with the green line at another two points with $\omega/\omega_{pe} > 1$. The red line with $\beta_z = 0.8$ intersects with the black line at two points while the blue line with $\beta_z = 4$ intersects with the black line at four points. There are four roots of equation (2.15). The Fig. 2.1 indicates that x has one pair conjugate complex roots when $\beta_z > \beta_c$, where

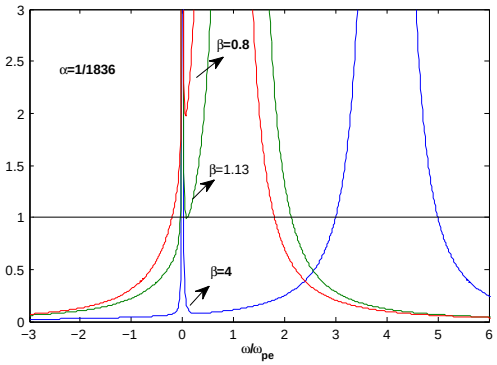

Figure 2.1: The red, green and blue lines correspond to the functions $y = \alpha/x^2 + 1/(x-\beta_z)^2$ versus $x = \omega/\omega_{pe}$ for parameter $\beta_z = \mathbf{k}\cdot\mathbf{v}_{de}/\omega_{pe} = 0.8, 1.13, 4$ and $\alpha = m_e/m_i = 1/1836$. The black solid line is $y = 1$.

β_c is the critical point at which the conjugate complex roots are equal. From Fig. 2.1, β_c is around 1.1. The likely range to have complex roots is about $\omega \ll \omega_{pe}$. The positive imaginary part of the roots $Im(x) > 0$ represents the growth of the unstable modes.

Exploring unstable modes in the frequency range $\omega_{pi} \ll \omega \ll \omega_{pe}$, we approximate the equation (2.15) as :

$$\beta_z - x = (1 - \alpha/x^2)^{-1/2} \approx 1 + \alpha/2x^2, \tag{2.16}$$

Setting $x = |x|e^{i\phi}$ for possible complex roots of the dispersion relation, and equating the imaginary parts in the approximation of equation (2.15), we obtain $|x| = (\alpha cos\phi)^{1/3}$. The growth rate γ is the imaginary part of the frequency. $Im(x) = (\alpha cos\phi)^{1/3} sin\phi$, and maximizes at $\phi \approx \pi/3$ where $\beta_z \approx 1$. Thus the maximum growth rate is $\gamma_{max} = \frac{\sqrt{3}}{2}\omega_{pe}(m_e/2m_i)^{1/3} \sim 0.056\omega_{pe}$ and the corresponding frequency is $Re(\omega) = \frac{\omega_{pe}}{2}(m_e/2m_i)^{1/3} \approx 0.032\omega_{pe}$ at $\mathbf{k}\cdot\mathbf{v}_{de} = \omega_{pe}$.

Fig. 2.2 shows the variation of the Buneman growth rate versus β_z for $\mathbf{k}||\mathbf{v}_{de}$.

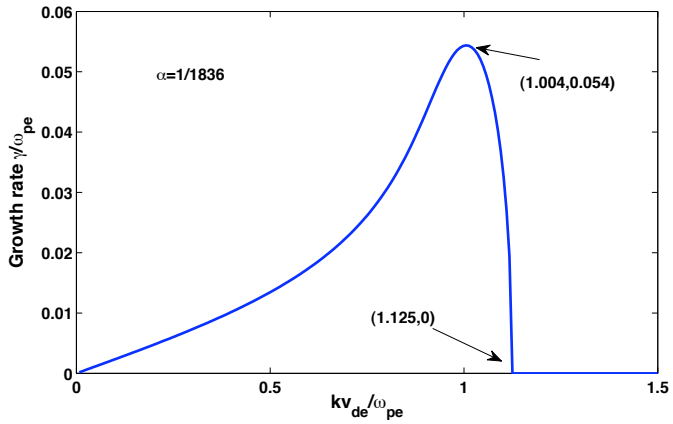

Figure 2.2: The Buneman growth rate γ/ω_{pe} versus β_z for $\alpha = m_e/m_i = 1/1836$ and $\mathbf{k}||\mathbf{v}_{de}$.

The growth rate peaks at $(\beta_z, \gamma/\omega_{pe}) = (1.004, 0.054)$. The cutoff $\beta_c = 1.125$.

This derivation suggests that the maximum growth rate is independent of v_{de}. However this is only true if k can vary freely. In reality k has a maximum value given roughly be the distance traveled by the electrons during one electron-plasma period $1/\omega_{pe}$, which is of the order of the Debye length $\lambda_D = v_{th}/\omega_{pe} \sim 1/k = v_{de}/\omega_{pe}$. Therefore, our arguments only hold when v_{de} exceeds the electron thermal velocity. This condition has been verified by many others (Papadopoulos & Palmadesso 1976; Galeev & Sagdeev 1984b,a).

2.1.2 Electron-electron Two-Stream Instability

When an electron beam is injected into cold plasma, the beam and the electrons in the cold plasma can lead to the electron-electron two-stream instability. The density ratio of the electron beam and electron background is denoted as $\alpha = n_{be}/n_e \ll 1$.

Electron-electron two stream instability can be derived and analyzed in a similar manner as the Buneman instability. The dispersion relation in the frame of the background electrons is:

$$\frac{1}{x^2} + \frac{\alpha}{(x-\beta_z)^2} = 1, \tag{2.17}$$

where x and β_z are the same as defined for the Buneman instability.

From a theorem on the roots of quartic equations, the degenerate conjugate roots of equation (2.17) require (two real roots and two equal complex roots):

$$\beta_c = (1+\alpha^{1/3})^{3/2}. \tag{2.18}$$

If $\beta_z > \beta_c$, there are no complex roots and the system is stable.

In some space plasma and lab experiments, the injected electron beam density n_{be} is very low compared to the background plasma electron density n_e. For $\alpha \ll 1$, and $\omega \ll \omega_{pe}$, we require $x \approx \beta_z$ so that the term $\alpha/(x-\beta_z)^2$ in dispersion relation (2.17) is not negligible or the dispersion relation has no complex roots.

Equation (2.17) can be written as :

$$x \approx \beta_z \pm \frac{\sqrt{\alpha}}{(1-1/\beta_z^2)^{1/2}}. \tag{2.19}$$

When $\beta_z > 1$, x is real and the group velocity of the electrostatic wave is $v_g = \frac{d\omega}{dk} = \frac{dx}{d\beta_z} v_{de} \approx v_{de}$; When $\beta_z < 1$, x is complex conjugate pair and the growth rate of unstable modes is $\gamma = \frac{\sqrt{\alpha}\omega_{pe}}{(1/\beta_z^2-1)^{1/2}}$.

When $\beta_z \approx 1$, $1/(1-1/\beta_z^2)^{1/2} \longrightarrow \infty$ and the above discussions are no longer valid. We discuss this limit in a different way. Assuming $x = 1+\delta x$, and substituting

x into equation (2.17), we have the form:

$$\frac{\alpha}{\delta x^2} - 2\delta x = 0, \tag{2.20}$$

Multiplying δx^2 to both sides of equation (2.17), and factoring the polynomial as $\delta x^3 - \alpha/2 = (\delta x - (\alpha/2)^{1/3})(\delta x^2 + (\alpha/2)^{1/3}\delta x + (\alpha/2)^{2/3})$, we have the three roots:

$$\delta x = (\alpha/2)^{1/3},$$
$$\delta x = \frac{-(\alpha/2)^{1/3} \pm i\sqrt{3}(\alpha/2)^{1/3}}{2},$$

thus the growth rate of unstable wave is $\gamma = \sqrt{3}(\alpha/2^4)^{1/3}\omega_{pe}$.

The instability with $\beta_z \leq 1$ is called the electron-electron two-stream instability. Its group velocity is around v_{de} and the faster growing mode is determined by both α and β_z.

2.2 Kinetic Description of Electrostatic Instability in Plasma

2.2.1 Dispersion Function of Electrostatic Instability for Magnetized Particles

The thermal effect on the growth of unstable waves is neglected in the two-fluid approach. They become important in a warm plasma. The investigation of thermal effects on the instability requires that we analyze the Vlasov equation. In this section, we will obtain the general dispersion relation from the Vlasov equation in magnetized plasma in the linear approximation. By including a magnetic field we also find additional instabilities, such as the lower hybrid instability which is nearly perpendicular to the magnetic field.

We assume the equlibrium electric field $\mathbf{E} = 0$ and the magnetic field $\mathbf{B} = B_z\hat{z}$ to be constant. The Vlasov equation for species j is:

$$\frac{\partial f_j}{\partial t} + \mathbf{v} \cdot \frac{\partial f_j}{\partial \mathbf{x}} + \frac{e_j}{m_j}(\frac{\mathbf{v}}{c} \times \mathbf{B}) \cdot \frac{\partial f_j}{\partial \mathbf{v}} = 0 \tag{2.21}$$

where $f_j(\mathbf{x}, \mathbf{v}, t)$ is the distribution function of species j.

In cylindrical polar coordinates, $(r,\ \phi,\ z)$, the system is symmetric about z. The distribution function f_j is only a function of $v_\perp^2$ and v_z, where $v_\perp^2 = v_x^2 + v_y^2$ and $v_z = v_z$.

For electrostatic perturbations, $\delta\mathbf{B} = 0$, we assume $\mathbf{E} = \delta\mathbf{E}$ and $f_j = f_j + \delta f_j$, where the equilibrium distribution $f_j = n_{j0} f_{j0}$, f_{j0} is normalized by the ambient density n_{j0}: $2\pi \int_0^\infty dv_\perp v_\perp \int_{-\infty}^\infty dv_z f_{j0} = 1$.

The linearized perturbation equation from the Vlasov equation (2.21) is

$$(\frac{\partial}{\partial t} + \mathbf{v} \cdot \frac{\partial}{\partial \mathbf{r}} + \frac{e_j}{m_j}(\frac{\mathbf{v}}{c} \times \mathbf{B}) \cdot \frac{\partial}{\partial \mathbf{v}})\delta f_j = -\frac{n_{j0} e_j}{m_j} \delta\mathbf{E} \cdot \frac{\partial f_{j0}}{\partial \mathbf{v}} \tag{2.22}$$

Using the full differential operator $\frac{d}{dt}$ to replace the operators within the bracket in the left side of equation (2.22), we obtain the solution of δf_j:

$$\delta f_j = -\frac{n_{j0} e_j}{m_j} \int_{-\infty}^{t} dt' \delta\mathbf{E}(\mathbf{r}', t') \frac{\partial f_{j0}(v_\perp'^2, v_z')}{\partial \mathbf{v}'} \tag{2.23}$$

where ($\mathbf{r}'$,$\mathbf{v}'$) satisfy the unperturbed orbit equations $\frac{d\mathbf{r}'}{dt'} = \mathbf{v}'$ and $\frac{d\mathbf{v}'}{dt'} = \frac{e_j}{cm_j}(\mathbf{v}' \times \mathbf{B})$, and passes through the initial point ($\mathbf{r}$,$\mathbf{v}$) at $t' = t$. It should be noted that equation (2.23) is valid for any electrostatic field with non-uniform magnetic field. However, assuming a uniform magnetic field allow further progress to be made.

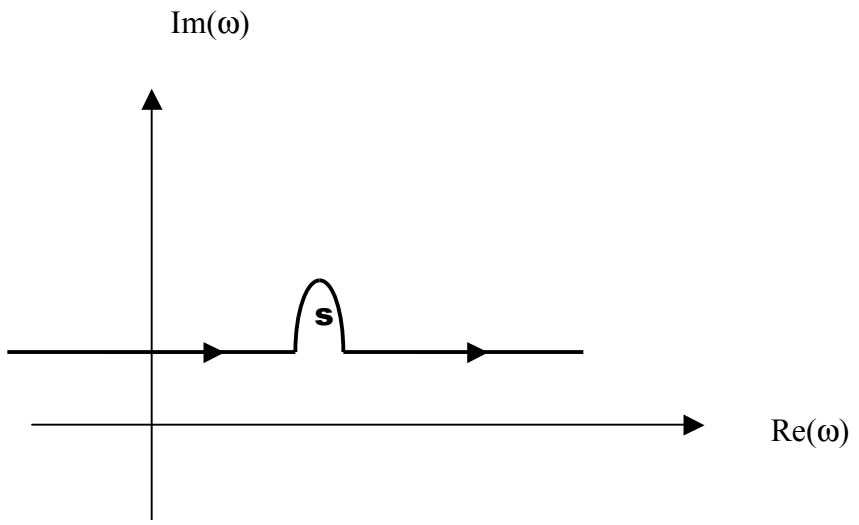

Figure 2.3: An illustration of contour C used in equation (2.24).

Let us assume $\delta\mathbf{E}$ and δf_j are represented by Fourier-Laplace transforms

$$\begin{aligned}\delta\mathbf{E} &= \int d^3\mathbf{k} e^{i\mathbf{k}\cdot\mathbf{r}} \int_C \frac{d\omega}{2i\pi} e^{-i\omega t}\widehat{\delta\mathbf{E}},\\ \delta\mathbf{f}_j &= \int d^3\mathbf{k} e^{i\mathbf{k}\cdot\mathbf{r}} \int_C \frac{d\omega}{2i\pi} e^{-i\omega t}\widehat{\delta\mathbf{f}}_j,\end{aligned} \tag{2.24}$$

where $Im(\omega) > 0$ is assumed large enough that the Laplace transform integral $\widehat{\delta\mathbf{E}}(\mathbf{k},\omega) = \int_0^\infty dt e^{i\omega t}\delta\mathbf{E}(\mathbf{r},t)$ etc. converges. The contour C in equation (2.24) runs from $-\infty + \mathbf{s}i$ to $\infty + \mathbf{s}i$ as shown in Fig.2.3, $Im(\omega) > s$.

In the $(\mathbf{k},\omega)$ space, equation (2.23) yields

$$\widehat{\delta f_j} = \frac{-n_{j0}e_j}{m_j}\int_{-\infty}^{t} dt' e^{i\mathbf{k}\cdot(\mathbf{r}'-\mathbf{r})-i\omega(t'-t)}\left(\frac{\widehat{\delta\mathbf{E}}_\perp\cdot\mathbf{v}'_\perp}{v_\perp}\frac{\partial f_{j0}(v_\perp^2,v_z)}{\partial v_\perp} + \widehat{\delta E}_z\frac{\partial f_{j0}(v_\perp^2,v_z)}{\partial v_z}\right) \tag{2.25}$$

where the explicit t' dependence in 2.25 occurs in the item $\widehat{\delta\mathbf{E}}_\perp\cdot\mathbf{v}'_\perp$ and the index of exponential function, and we have used the fact that $v'_\perp$ and v'_z are constant along the unperturbed trajectory, i.e $v_\perp = v'_\perp$ and $v'_z = v_z$.

Defining the perpendicular velocity phase ϕ at $t = t'$, we rewrite the velocity

in terms of its Cartesian components $\mathbf{v} = (v_\perp cos\phi, v_\perp sin\phi, v_z)$, then the solution to the nonperturbed orbit equation yields:

$$v'_x = v_\perp cos(\phi - \Omega_j \tau), v'_y = v_\perp sin(\phi - \Omega_j \tau), v'_z = v_z. \tag{2.26}$$

and

$$\begin{aligned} x' &= x - (v_\perp/\Omega_j)[sin(\phi - \Omega_i \tau) - sin\phi], \\ y' &= y + (v_\perp/\Omega_j)[cos(\phi - \Omega_i \tau) - cos\phi], \\ z' &= z + v_z \tau, \end{aligned} \tag{2.27}$$

where $\Omega_j = e_j B/cm_j$, the cyclotron frequency of species j, and $\tau = t' - t$.

Making use of the identity

$$e^{iasinx} \equiv \sum_{n=-\infty}^{n=\infty} J_n(a) e^{inx}, \tag{2.28}$$

where J_n is a Bessel function of the first kind of order n.

The exponential factor in the orbit integral in equation (2.25) then can be expressed as

$$\begin{aligned} e^{i\mathbf{k}\cdot(\mathbf{r}'-\mathbf{r})-i\omega\tau} &= e^{ik_z v_z - i\omega\tau + \frac{ik_\perp v_\perp}{\Omega_j}(sin\phi - sin(\phi - \Omega_i t))} \\ &= \sum_{m=-\infty}^{m=\infty} \sum_{n=-\infty}^{n=\infty} J_m(\frac{k_\perp v_\perp}{\Omega_j}) J_n(\frac{k_\perp v_\perp}{\Omega_j}) e^{i(m-n)\phi} e^{i(k_z v_z + n\Omega_j - \omega)\tau}, \end{aligned} \tag{2.29}$$

where we have assumed that the wavevector lies in the $x - z$ plane without loss of the generality (Davidson 1972).

With $v_\perp = (v_x^{'2} + v_y^{'2})^{1/2}$, it is easy to show

$$\frac{\partial f_{j0}}{\partial v_x'} = cos[\phi - \Omega_j\tau]\frac{\partial f_{j0}}{\partial v_\perp},$$
$$\frac{\partial f_{j0}}{\partial v_y'} = sin[\phi - \Omega_j\tau]\frac{\partial f_{j0}}{\partial v_\perp},$$
$$\frac{\partial f_{j0}}{\partial v_z'} = \frac{\partial f_{j0}}{\partial v_z}. \tag{2.30}$$

In the electrostatic case, $\mathbf{k}\times\mathbf{E} = 0$, thus $\mathbf{E}$ also lies in the $x-z$ plane. Using $cos(\phi-\Omega_j\tau) = 1/2[e^{i(\phi-\Omega_j\tau)} + e^{-i(\phi-\Omega_j\tau)}]$, the identity $J_{n-1}+J_{n+1} = (2n\Omega_j/k_\perp v_\perp)J_n$ and equation (2.30), equation (2.25) can be written as

$$\widehat{\delta f_j} = -\frac{n_{j0}e_j}{m_j}\sum_{m=-\infty}^{m=\infty}\sum_{n=-\infty}^{n=\infty}\frac{J_m e^{(m-n)\phi}}{\omega - n\Omega_j - k_z v_z}[\frac{n\Omega_j J_n}{k_\perp v_\perp}\frac{\partial f_{j0}}{\partial v_\perp}\widehat{\delta E}_\perp + J_n\frac{\partial f_{j0}}{\partial v_z}\widehat{\delta E}_z]. \tag{2.31}$$

To obtain the dispersion relation for electrostatic perturbations, the perturbed distribution function in equation (2.31) needs to be substituted into Poisson's equation expressed in $(\mathbf{k},\omega)$ space, i.e $k^2\widehat{\varphi} = 4\pi e_j\int d^3\mathbf{v}\widehat{\delta f_j}$. The dispersion relation is $D = 1 - 1/k^2(4\pi\int d^3\mathbf{v}\widehat{\delta f_j}) = 0$, where D is the dielectric function.

Integration over velocity space can be expressed as $\int d^3v = \int d\phi\int v_\perp dv_\perp\int dv_z$. Integrating $\widehat{\delta f_j}$ over the angle ϕ, only the terms with $m = n$ survive, and the dispersion relation becomes

$$1 + \sum_j \chi_j = 0,$$
$$\chi_j = \frac{\omega_{pj}^2}{k^2}\sum_{n=-\infty}^{n=\infty}\int d^3v\frac{J_n^2(\frac{k_\perp v_\perp}{\Omega_j})}{\omega - n\Omega_j - k_z v_z}(k_z\frac{\partial f_{j0}}{\partial v_z} + \frac{n\Omega_j}{v_\perp}\frac{\partial f_{j0}}{\partial v_\perp}). \tag{2.32}$$

where $\omega_{pj} = \sqrt{4\pi n_j e_j^2/m_j}$ and χ_j is the plasma dielectric response of species j (Davidson 1972).

2.2.2 Dispersion Function of Electrostatic Instabilities For Unmagnetized Particles

A particle is considered unmagnetized when its thermal Lamour radius $r_L = v_{th}/\Omega_j$ is much larger than the perpendicular wavelength $\mid k_\perp r_L \mid \gg 1$, and its cyclotron frequency is much slower than the wave frequency, or $\mid \omega/\Omega_j \mid \gg 1$.

In this limit, it is reasonable to assume that the unperturbed orbit of unmagnetized particles (such as ions) is a straight line $x' = x + v\tau$ and $v' = v$ on the time and length scales of interest. The equation of the perturbed distribution function can be written as

$$(\frac{\partial}{\partial t} + \mathbf{v} \cdot \frac{\partial}{\partial \mathbf{r}})\widehat{\delta f_j} = -i\frac{n_{j0}e_j}{m_j}\mathbf{k} \cdot \frac{\partial f_{j0}}{\partial \mathbf{v}}\widehat{\delta\varphi}, \tag{2.33}$$

where we have replaced $\widehat{\delta\mathbf{E}}$ by $i\mathbf{k}\widehat{\delta\varphi}$.

Using the same Fourier-Laplace transformation listed in the equation (2.24), a direct calculation of the perturbed distribution function gives

$$\widehat{\delta f_j} = -\frac{n_{j0}e_j}{m_j}\frac{\mathbf{k} \cdot \partial f_{j0}/\partial \mathbf{v}}{\omega - \mathbf{k} \cdot \mathbf{v}}\widehat{\delta\varphi}, \tag{2.34}$$

then the corresponding dielectric response is

$$\chi_j = \frac{\omega_{pj}^2}{k^2}\int d^3\mathbf{v}\frac{\mathbf{k} \cdot \partial f_{j0}/\partial \mathbf{v}}{\omega - \mathbf{k} \cdot \mathbf{v}}, \tag{2.35}$$

where $\mathbf{k} = k_\perp \hat{\mathbf{e}}_x + k_z \hat{\mathbf{e}}_z$.

2.3 Streaming Instabilities in Magnetized Plasma

2.3.1 Kinetic Description

In a magnetized plasma composed of ions and electrons, the electrons generally are magnetized but the ions can be unmagnetized since the ratio of electron and ion larmour radii $r_{Le}/r_{Li} \sim \Omega_i/\Omega_e \sim \sqrt{m_e/m_i} \ll 1$.

We have introduced the dispersion relations of electrostatic waves in magnetized and unmagnetized plasma in sections 2.2.1 and 2.2.2. From equations (2.32) and (2.35), we have the dispersion relation for a plasma with magnetized electrons and unmagnetized ions:

$$\begin{aligned} 1 + \chi_e + \chi_i &= 0, \\ \chi_i &= \frac{\omega_{pi}^2}{k^2} \int d^3\mathbf{v} \frac{\mathbf{k} \cdot \partial f_{i0}/\partial \mathbf{v}}{\omega - \mathbf{k} \cdot \mathbf{v}}, \\ \chi_e &= \frac{\omega_{pe}^2}{k^2} \sum_{n=-\infty}^{n=\infty} \int d^3v \frac{J_n^2(\frac{k_\perp v_\perp}{\Omega_e})}{\omega - n\Omega_e - k_z v_z} (k_z \frac{\partial f_{e0}}{\partial v_z} + \frac{\Omega_e}{v_\perp} \frac{\partial f_{e0}}{\partial v_\perp}). \end{aligned} \tag{2.36}$$

It is reasonable to assume that the initial distribution functions of f_{e0} and f_{i0} are Maxwellians with drifts v_{de} and v_{di} along the magnetic field $\mathbf{B} = B_z \hat{z}$,

$$\begin{aligned} f_{i0}(v_\perp^2, v_z) &= \frac{\mathbf{e}^{\frac{-v_\perp^2}{v_{ti}^2}}}{\pi^{3/2} v_{ti}^3} \mathbf{e}^{-\frac{(v_z - v_{di})^2}{v_{ti}^2}}, \\ f_{e0}(v_\perp^2, v_z) &= \frac{\mathbf{e}^{\frac{-v_\perp^2}{v_{\perp te}^2}}}{\pi^{3/2} v_{zte} v_{\perp te}^2} \mathbf{e}^{-\frac{(v_z - v_{de})^2}{v_{zte}^2}}, \end{aligned} \tag{2.37}$$

where $v_{tj}^2 = 2T_j/m_j$, T_j is temperature, m_j is the mass and j represents the species of electron or ion.

Substituting equation (2.37) into equation (2.36), we obtain the dispersion

relation for the ion-electron two stream instability:

$$
\begin{aligned}
&1 + \chi_i + \chi_e = 0, \\
&\chi_i = \frac{2\omega_{pi}^2}{k^2 v_{ti}^2}[1 + \eta_i Z(\eta_i)], \\
&\chi_e = \frac{2\omega_{pe}^2}{k^2 v_{te}^2}[1 + I_0(\lambda)e^{-\lambda}\eta_e Z(\eta_e) + \eta_e \sum_{n\neq 0} (e)^{-\lambda} I_n(\lambda) Z(\xi_n)],
\end{aligned} \tag{2.38}
$$

where $\eta_i = (\omega - k_z v_{di})/k v_{ti}$, $\eta_e = (\omega - k_z v_{de})/k_z v_{zte}$, $\lambda = k_\perp^2 v_{\perp te}^2/2\Omega_e^2$, and $\xi_n = (\omega - k_z v_{de} - n\Omega_e)/k_z v_{te}$. Z is the plasma dispersion function and I_n is the modified Bessel function of first kind of order n(Davidson 1972). These two functions are defined as

$$
\begin{aligned}
Z(\eta) &\equiv \pi^{-1/2} \int_{-\infty}^{\infty} dx \frac{\mathbf{e}^{-x^2}}{x - \eta}, \\
\int_0^\infty x J_n^2(sx) \mathbf{e}^{-x^2} dx &\equiv \frac{\mathbf{e}^{-s^2}}{2} I_n(s^2/2).
\end{aligned} \tag{2.39}
$$

The complexity of equation (2.38) makes it difficult to develop a physical picture. As an example, we will discuss the cold plasma limit of equation (2.38).

2.3.2 Cold Plasma Limit: Buneman Instability and Lower Hybrid Instability

The cold plasma limit can give us the main features of the dispersion relation (2.38). There are three methods to obtain the plasma cold limit. One is to directly derive the dispersion relation from the fluid equations as we have shown in the first section. The second is to obtain the dispersion relation from equation (2.38) by approximating the modified Bessel function $I_0(\lambda)e^{-\lambda} \longrightarrow 1$ for $\lambda \ll 1$ and the

plasma dispersion function $\zeta Z(\zeta) \longrightarrow -1 - 1/2\zeta^2$ for $\zeta \gg 1$. The third is shown below.

The velocity distribution functions in equation (4.3) become δ functions when the temperature goes to zero (the corresponding thermal velocity goes to zero):

$$f_{e0} = \frac{1}{v_\perp}\delta(v_\perp)\delta(v_z - v_{de}),$$
$$f_{i0} = \frac{1}{v_\perp}\delta(v_\perp)\delta(v_z), \tag{2.40}$$

where for simplicity we set $v_{di} = 0$.

Substituting the δ functions in equation (2.40) into the dispersion relation equation (2.38), we obtain the dispersion relation of Buneman instability in the cold plasma limit:

$$1 - \frac{\omega_{pi}^2}{\omega^2} - \frac{sin^2\theta\omega_{pe}^2}{(\omega - k_z v_{de})^2 - \Omega_e^2} - \frac{cos^2\theta\omega_{pe}^2}{(\omega - k_z v_{de})^2} = 0 \tag{2.41}$$

where θ is the angle between the wave vector $\mathbf{k}$ and magnetic field, and $k_z = kcos\theta$.

Since coupling to the ions requires $\omega \ll \omega_{pe}$, we assume $\Omega_e \gg \omega - k_z v_{de}$, so that equation (2.41) can be written as:

$$1/\Theta^2 - \alpha/x^2 - cos^2\theta/(x - \beta_{zz})^2 = 0, \tag{2.42}$$

where $\Theta^2 = 1/(1 + sin^2\theta\omega_{pe}^2/\Omega_e^2)$, $x = \omega/\omega_{pe}$, $\beta_{zz} = k_z v_{de}/\omega_{pe}$ and $\alpha = \omega_{pi}^2/\omega_{pe}^2$.

As in the evaluation of the dispersion relation of the Buneman instability (2.15), we can expand equation (2.42) to the lowest order:

$$\beta_z - x = \Theta cos\theta(1 - \alpha\Theta^2/x^2)^{-1/2},$$
$$\approx \Theta cos\theta(1 + \alpha\Theta^2/2x^2). \tag{2.43}$$

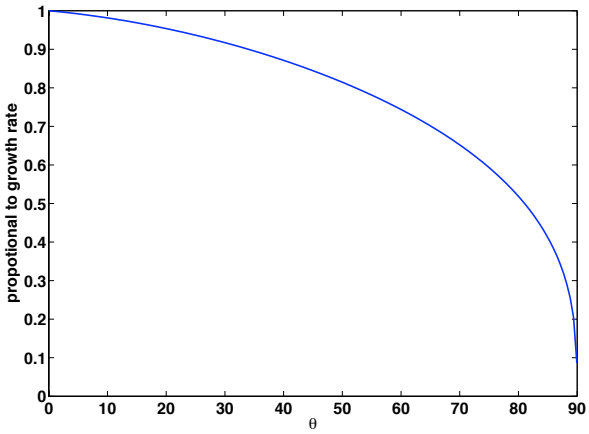

Figure 2.4: An illustration of function $cos^{1/3}\theta\Theta$ versus θ.

The complex frequency with maximum positive imaginary part is:

$$\omega = (\alpha cos\theta/2)^{1/3}\Theta\omega_{pe}e^{i\pi/3}, \tag{2.44}$$

with $kv_{de} = \Theta\omega_{pe}$.

Equation (2.44) reduces to the Buneman instability $\omega = \sqrt{3}\alpha^{1/3}\omega_{pe}/2^{4/3}$ with small $\theta \sim 0$ and reduces to the nearly-perpendicular lower hybrid instability with growth rate $\gamma = \Theta\omega_{pi} \sim \omega_{pi}/2$ with $cos\theta \sim \sqrt{\alpha} = \sqrt{m_e/m_i}$. However, equation (2.44) was obtained to lowest order in α. We need to go to higher order in α when the frequency is close to the ion plasma frequency ω_{pi}.

We demonstrate the restriction of equation (2.44) for nearly-perpendicular instability in Fig. 2.4 and Fig. 2.5. Fig. 2.4 is the evolution of the maximum growth rate in equation (2.44) with the angle θ and Fig. 2.5 is the growth rate versus the wavevector k with different angle θ from the numerical solution of the equation (2.42) using $m_i/m_e = 100$ and $\omega_{pe}/\Omega_e = 0.4$. From Fig. 2.4, we see that the maximum growth rate of the unstable mode decreases smoothly with the angle θ. The lower

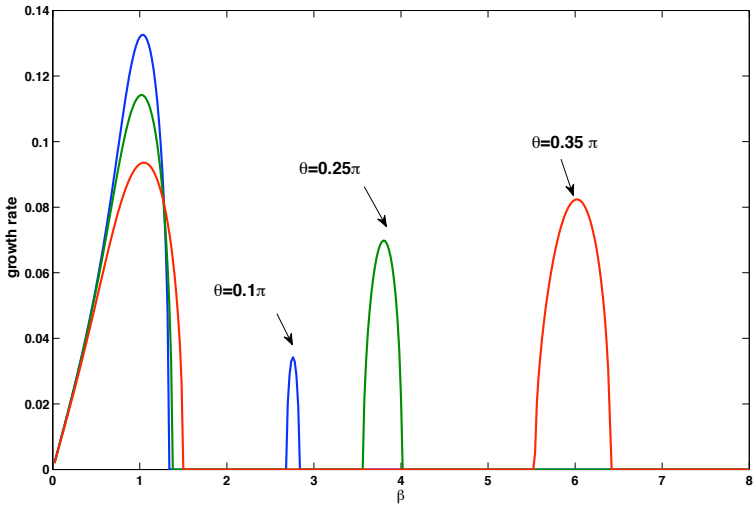

Figure 2.5: Growth rate versus $\beta = kv_{de}/\omega_{pe}$ at different angles $\theta = 0.1\pi$, 0.25π, and 0.35π, denoted by blue, green and red lines.

hybrid instability is only a limit of the Buneman instability; but in Fig. 2.5, there are two distinct unstable modes. The first mode peaks at $\beta \sim 1$ and corresponds to the Buneman instability with peaks that decrease with the angle. The peaks of the second mode increase with the angle θ and the corresponding wavenumbers increase. The second mode is the lower hybrid instability. So equation (2.44) is a good approximation for the Buneman instability with small θ and the lower hybrid instability is not the oblique limit of the Buneman instability.

2.3.3 Electron-electron Two-stream Instability

Similarly to ion-electron two-stream instability, the dispersion relation is:

$$1 + \Delta\chi_{e1} + (1-\Delta)\chi_{e2} = 0,$$

$$\chi_{e1} = \frac{2\omega_{pe}^2}{k^2 v_{te1}^2}[1 + I_0(\lambda_{e1})e^{-\lambda_{e1}}\eta_{e1}Z(\eta_{e1}) + \eta_{e1}\sum_{n\neq 0}\mathbf{e}^{-\lambda_{e1}}I_n(\lambda_{e1})Z(\xi_{ne1})],$$

$$\chi_{e2} = \frac{2\omega_{pe}^2}{k^2 v_{te2}^2}[1 + I_0(\lambda_{e2})e^{-\lambda_{e2}}\eta_{e2}Z(\eta_{e2}) + \eta_{e2}\sum_{n\neq 0}\mathbf{e}^{-\lambda_{e2}}I_n(\lambda_{e2})Z(\xi_{ne2})], \quad (2.45)$$

where Δ is the weight of the first distribution function, $\eta_{ej} = (\omega - k_z v_{ezj})/kv_{tej}$, $\eta_{ej} = (\omega - k_z v_{dej})/k_z v_{ztej}$, $\lambda_{ej} = k_\perp^2 v_{\perp tej}^2/2\Omega_e^2$, $\xi_{nej} = (\omega - k_z v_{dej} - n\Omega_e)/k_z v_{tej}$, and j denotes electron stream 1 and 2. The distribution function has been assumed to be:

$$f_{e0}(v_\perp^2, v_z) = \frac{\mathbf{e}^{\frac{-v_\perp^2}{v_{\perp te}^2}}}{\pi^{3/2}v_{\perp te}^2}\left(\frac{1-\Delta}{v_{zte1}}\mathbf{e}^{-\frac{(v_z - v_{de1})^2}{v_{zte1}^2}} + \frac{\Delta}{v_{zte2}}\mathbf{e}^{-\frac{(v_z - v_{de2})^2}{v_{zte2}^2}}\right). \quad (2.46)$$

The corresponding cold plasma limit is :

$$1 - \frac{(1-\Delta)sin^2\theta\omega_{pe}^2}{(\omega - k_z v_{de1})^2 - \Omega_e^2} - \frac{(1-\Delta)cos^2\theta\omega_{pe}^2}{(\omega - k_z v_{de1})^2}$$
$$-\frac{\Delta sin^2\theta\omega_{pe}^2}{(\omega - k_z v_{de2})^2 - \Omega_e^2} - \frac{\Delta cos^2\theta\omega_{pe}^2}{(\omega - k_z v_{de2})^2} = 0, \quad (2.47)$$

Without losing generality, let us assume $v_{de1} = 0$ and $\Omega_e > \omega_{pe} \gg \omega$ so that equation (2.47) takes the form:

$$1 + \frac{sin^2\theta\omega_{pe}^2}{\Omega_e^2} - \frac{(1-\Delta)cos^2\theta\omega_{pe}^2}{\omega^2} - \frac{\Delta cos^2\theta\omega_{pe}^2}{(\omega - k_z v_{de})^2} = 0. \quad (2.48)$$

If the density of the injected electron beam is much less than the density of the cold plasma background, i.e. $\Delta \ll 1$, then the condition for the dispersion relation having complex roots requires $\omega - k_z v_{de} \sim 0$. Under this condition the term

$\frac{\Delta cos^2\theta\omega_{pe}^2}{(\omega-k_z v_{de})^2}$ can be comparable to the term $\frac{(1-\Delta)cos^2\theta\omega_{pe}^2}{\omega^2}$. As in the discussion of 2.17, we have

$$x = \beta_z \pm \frac{\sqrt{\Delta}cos\theta}{(\Theta^2 - \frac{cos\theta^2}{\beta_z^2})^{1/2}}, \tag{2.49}$$

where $\Theta^2 = 1 + \frac{sin\theta\omega_{pe}^2}{\Omega_e^2}$. For $\beta_z < \frac{cos\theta}{\Theta}$, the roots are complex conjugates. For $\beta_z > \frac{cos\theta}{\Theta}$, the roots are real.

For $\beta_z \approx \frac{cos\theta}{\Theta}$, $\frac{\sqrt{\Delta}cos\theta}{(\Theta^2 - \frac{cos\theta^2}{\beta_z^2})^{1/2}} \longrightarrow \infty$, the above discussion becomes invalid. We will discuss this case in the small angle and large angle limits. For $\theta \sim 0$, $\beta_z \sim 1$, and we have the electron-electron two stream instability discussed in the first section. For $\theta \sim \pi/2$, $\beta_z \sim cos\theta$ and $x \sim cos\theta$, i.e $\omega \sim cos\theta\omega_{pe}$, and equation (2.48) becomes

$$\Delta + \frac{sin^2\theta\omega_{pe}^2}{\Omega_e^2} - \frac{\Delta cos^2\theta\omega_{pe}^2}{(\omega - k_z v_{de})^2} = 0. \tag{2.50}$$

There are no complex roots to equation (2.50). Therefore, the electron-electron two-stream analogue has no perpendicular instability and the growth rate has a cut-off with angle θ.

Chapter 3

Buneman Instability in Guide-Field Magnetic Reconnection

Magnetic reconnection in collisionless plasma drives strong currents near the x-line and separatrices. Satellite observations in the Earth's magnetosphere indicate that these current layers are turbulent. Electron holes, which are localized, positive-potential structures, have been linked to magnetic reconnection in the magnetotail (Farrell et al. 2002; Cattell et al. 2005) and the magnetopause(Matsumoto et al. 2003). Lower-hybrid waves and plasma waves appear in conjunction with electron holes in the magnetotail event. The dissipation associated with these turbulent wavefields may facilitate the breaking of magnetic field lines during collisionless magnetic reconnection (Galeev & Sagdeev 1984a).

During reconnection with a guide magnetic field perpendicular to the plane of reconnection, the widths of the electron current layers are of the order of the electron Larmor radius $\rho_e = v_{te}/\Omega_e$, where v_{te} is the electron thermal velocity and Ω_e is the cyclotron frequency of electrons (Hesse et al. 2004; Rogers et al. 2007). The resulting streaming velocity v_d is given by $v_d/v_{te} \propto \triangle B/(B\beta_e)$, where $\triangle B$ is the amplitude of the reconnection magnetic field and $\beta_e = 8\pi n T_e/B^2$ is the ratio of the electron and magnetic field pressure. The Buneman instability is driven unstable by electron-ion streaming when $v_d/v_{te} > 1$ (Buneman 1958; Papadopoulos & Palmadesso 1976; Drake et al. 2003). If the instability is strong enough, the wave

potential forms intense localized electric field structures called electron holes. The evolution of streaming instabilities has been previously investigated analytically and numerically (Boris et al. 1970; Davidson & Gladd 1975; Oppenheim et al. 2001; Singh et al. 2001b,a; Drake et al. 2003; Omura et al. 2003; McMillan & Cairns 2006, 2007; Goldman et al. 2008). In simulations lower hybrid turbulence is found to emerge after saturation of the parallel Buneman instability (Drake et al. 2003; McMillan & Cairns 2006, 2007). Whether the lower hybrid turbulence is a linearly unstable mode or nonlinearly driven by electron holes is unclear (McMillan & Cairns 2006, 2007). An important question is how the Buneman instability, which has a very low phase speed, can stop the runaway of high velocity electrons. The resolution of this puzzle is essential to understand how the streaming kinetic energy of electrons is transformed into electron thermal energy, what mechanism sustains electron holes after saturation of the Buneman instability, and ultimately what role turbulence plays in magnetic reconnection.

In this chapter, I will show evidence of the Buneman instability in magnetic reconnection simulations and the resulting turbulent heating which causes the anomalous resistivity. I also outline the problems we discussed above.

3.1 Buneman Instability in Magnetic Reconnection with a Guide Field

Our simulations are performed with a massively parallel Particle-In-Cell (PIC) p3d code (Zeiler et al. 2002), carried out on IBM and CRAY multiprocessor com-

puter systems. The relativistic motion of particles is described by the Lorentz equation. Faraday's law and Ampere's law are treated with a trapezoidal leapfrog scheme, and the positions and velocities of particles are stepped by the well-known Boris algorithm. The computational discretization error could accumulate and cause a secular violation of Gauss's law (an unreal electric field is produced). This numerical error is corrected by solving a Poisson's equation for a convection electric field in real space by a multigrid algorithm. All of the units used in the code are normalized: Magnetic field is measured by B_0, the asymptotic field strength outside of the current layer of the reconnecting magnetic field B_x; the electric field is measured by cB_0/c_A, $c_A = B_0/\sqrt{4\pi n_0 m_i}$ is the Alfven speed and n_0 is the asymptotic density of the plasma; mass= m/m_i and distance = $L/d_i, d_i = c/\omega_{pi}$ is the ion inertia length, ω_{pi} is the plasma frequency of ions; time= $\Omega_i t$, where $\Omega_i = eB_0/m_i c$ is the ion cyclotron frequency; velocity= v/c_A; and temperature = $kT/m_i c_A^2$.

The code uses Euclidean Cartesian Coordinates. The computational domain for our 3D simulations is $L_x = 4d_i$, $L_y = 2d_i$ and $L_z = 4d_i$, and periodic boundary conditions are adopted. The initial equilibrium is a double current layer superimposed on an ambient population of uniform density. The reconnection magnetic field component B_x is a function of the spatial coordinate y, the direction perpendicular to the current sheet:

$$\frac{B_x}{B_0} = \tanh\frac{y - L_y/4}{w_0} - \tanh\frac{y - 3L_y/4}{w_0} - 1 \tag{3.1}$$

where the coordinates x and y are parallel to the outflow and inflow for the x-line and $w_0 = 0.25d_i$, the current layer thickness. The total field $B^2 = B_x^2 + B_z^2 = 26B_0^2$

is constant, which implies the guide field varies spatially. Asymptotically, $B_z = 5B_0$ while at the x-line, $B_z = \sqrt{26}B_0$. The initial plasma density is constant and $n_e = n_i = n_0$. The temperatures of the ions and electrons are constant too and $T_e = T_i = 0.04 m_i c_A^2$. The mass ratio of ions and electrons is 100 and the speed of light $c = 20c_A$. We define the electromagnetic field on a grid of $512 \times 256 \times 512$ with an average of 20 particles per cell. The total number of particles is up to 1.3×10^9. The electron Debye length $\lambda_{de} = v_{th,e}/\omega_{pe} = 0.01 d_i$ is comparable to the grid scale, a requirement to avoid spurious electron heating.

The initial set-up of our simulation favors the occurrence of the Buneman instability rather than the ion acoustic instability, since the ion acoustic instability requires $T_e \gg T_i$. The current density is fully determined by the initial magnetic field $\nabla \times \mathbf{B} = \mathbf{j}$, which produces an initial electron drift $v_{de} = 4c_A$. The initial ion drift is zero. The width of the current sheet is restricted by the small computational box used in 3D, which in turn is restricted by current computational limitations. A thin current sheet requires a strong current density which can be understood from the jump condition of the magnetic field at the neutral line: $\triangle B_x / \triangle_{e,y} = \dfrac{4\pi}{c} j_{ez}$.

The larmor radius of ions is much larger than the scale of the electron diffusion region, hence within the electron diffusion region their dynamics can be neglected. Magnetic reconnection drives an intense magnetic-field-aligned electron beam around the x-line in 3D simulations. In the top panel of Fig.3.1 we can see that the drift velocity of electrons reached $v_{de} = 9c_A$ at $t = 3\Omega_i^{-1}$, much larger than the initial drift of $4c_A$. The strongly accelerated electron beams along the z direction at the x-line greatly exceed the Buneman instability threshold $v_{de} \gg 2v_{th,e} \approx 4c_A$

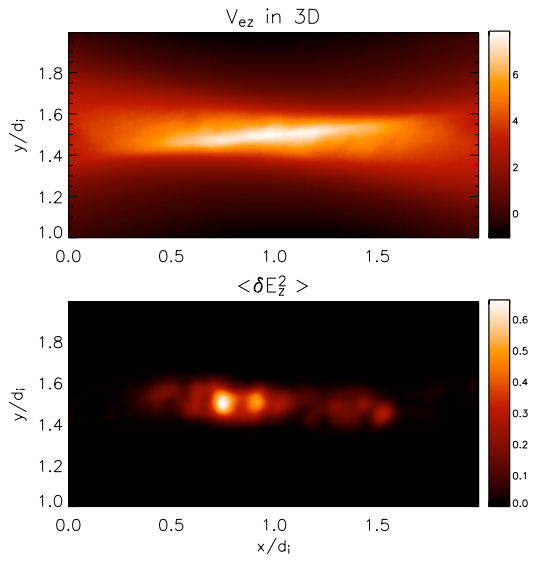

Figure 3.1: These two images are from the 3D reconnection simulation for initial temperature $T_e = 0.04$. The top one is the electron beam velocity v_{ez} around x-line at $t = 3\Omega_i^{-1}$; The bottom one is the covariance of electric field E_z, $\langle \delta E_z^2 \rangle$ when the Buneman instability starts to grow at $t = 3\Omega_i^{-1}$.

(Davidson 1984) and stimulates resonant interactions between fast electrons and the electrostatic perturbation δE_z (Fig.3.3), that leads to the growth of perturbations around the x-line (The bottom panel of Fig.3.1). The strength of $\langle \delta E_z^2 \rangle$ is around 0.5. The perturbation strength relative to the electron thermal energy $\langle \delta E^2 \rangle / (8\pi n k T_e) \sim 6 \gg 1$, an indication that the perturbations have an strong impact on the electron movement (Galeev & Sagdeev 1984a).

We show the distribution functions of electrons and ions at the x-line in Fig. 3.2 and Fig. 3.3. Compared to $f(v_{ez})$, the distribution functions of v_x and v_y show only a very small deviation from a Maxwellian distribution, implying that the Buneman instability propagates along the magnetic field at the x-line. From the linearized Vlasov equation, the fastest growing mode is $k_{gf} = \omega_{pe}/v_{de}$ with the frequency $\omega_{gf} = \frac{1}{2}(1 + i\sqrt{3})(\frac{m_e}{2m_i})^{1/3}\omega_{pe}$(Akhiezer et al. 1967; Davidson 1984). The corresponding

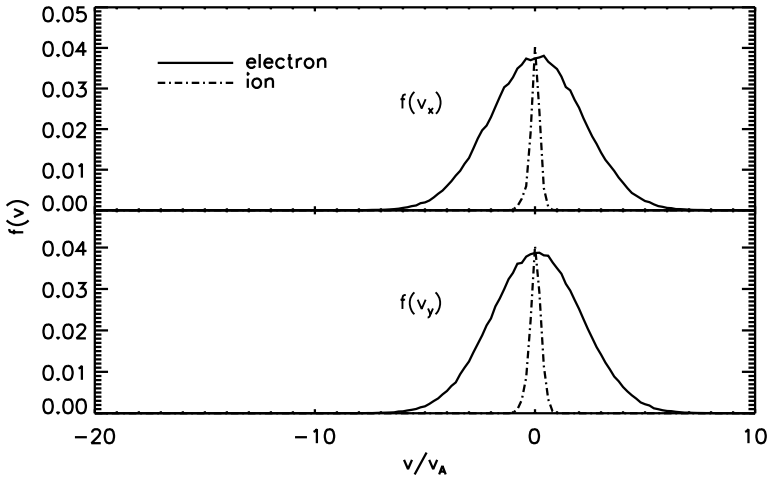

Figure 3.2: The electron and ion distribution functions of $f(v_x)$ and $f(v_y)$ around the x-line at $t = 4\Omega_i^{-1}$. The ion distribution functions are reduced by 10 times.

phase velocity of perturbed wave is $U_{res} = Re(\omega_{gf})/k_{gf} = \frac{1}{2}(\frac{m_e}{2m_i})^{1/3}v_{de}$. At $t = 3\Omega_i^{-1}$ and $t = 4\Omega_i^{-1}$, the electron beam has reached $v_{de} = 9v_A$ and $14v_A$ (Fig.3.3), and the corresponding phase velocities of the Buneman instability are $U_{res} \sim 0.8v_A$ and $1.2v_A$ respectively. The phase speeds fall in a 'plateau' extending from the velocities of the beam particles to the Maxwellian tail of the thermal particles (shown in green).

At $t = 3\Omega_i^{-1}$, the electrostatic perturbations δE_z have grown strong enough to form localized structures as displayed in Fig.3.4 which have been called electron holes(Berk & Roberts 1967). The electron holes move at a speed $v_{hole} \approx 3c_A$ which corresponds to the group velocity of the waves. In Fig. 3.4, the holes formed around the x-line ($x \sim 1$). One of the holes forms at $z = 2d_i$ and self-destruct around $z = 0$. The total distance this hole has traveled is $\triangle L_z \sim 2d_i$, and thus the hole's lifetime is $\sim \triangle L_z/v_{hole} \sim 0.6\Omega_i^{-1}$. The lifetime of the electron holes is

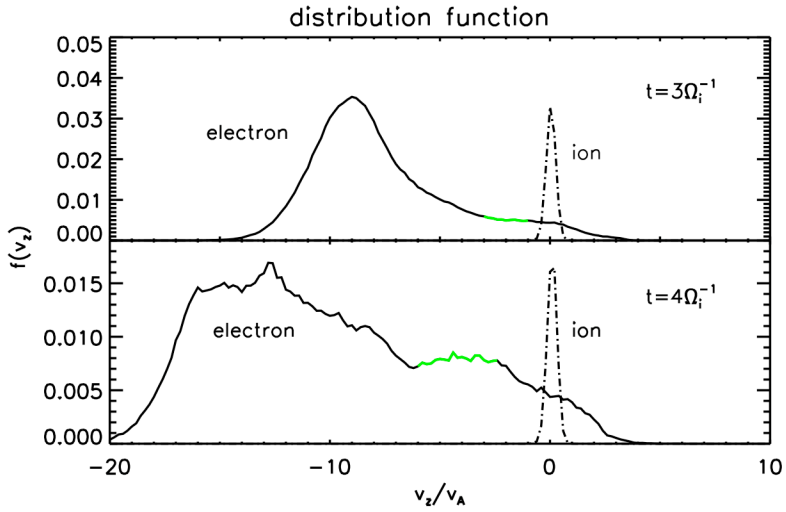

Figure 3.3: Distribution functions of electrons and ions around the x-line at $t = 3\Omega_i^{-1}$ (upper panel) and at $t = 4\Omega_i^{-1}$ (lower panel) in the 3D reconnection simulation with initial temperature $T_e = 0.04$. The normalization of the ion distribution functions in the upper and lower panels have been reduced by 70% and 90% respectively.The green color is the indicator of the resonance position of Buneman instability.

much longer than the crossing time of the electrons trapped in the potential well, $\tau_{cross} \approx \sqrt{m_e}\lambda/\sqrt{2e\delta E_z} \sim 0.02\Omega_i^{-1}$ (λ is the width of holes). Thus the electron holes are stable for a period time larger than the crossing time and can be described as BGK solutions (Sagdeev & Galeev 1969). However, because the electrons at the x-line are continuously accelerated by the reconnection electric field E_z, there exists no stationary BGK solution. New electron holes are continuously formed. The kinetic energy of the electron beam is channelled into the electron holes and then rechannelled into the electrons' thermal motion (Dupree 1983; Omura et al. 2003).

To further understand when turbulence develops and its role in 3D simulations, we also carried out two other simulations: (1) a 2D simulation in $x - y$ plane with identical parameters to those we used in the 3D simulation described above, but

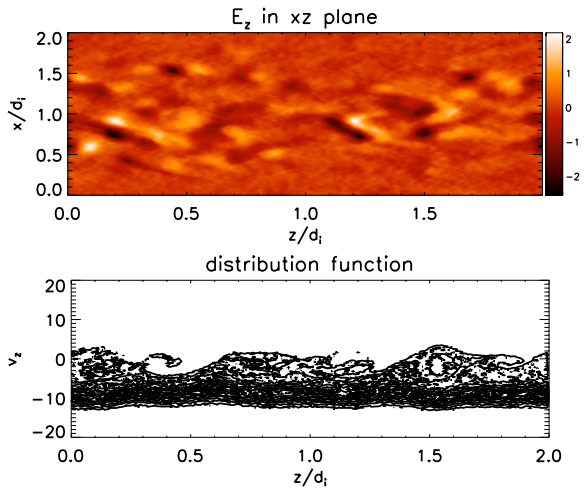

Figure 3.4: Electron holes formed around x-line at $t = 3\Omega_i^{-1}$. The top panel shows the image of E_z in $x - z$ plane; the bottom panel shows the distribution function of electrons in the phase space $z - v_z$ in the same region as in the top panel. The electrons move from right to left. The holes shown in the phase space (electron holes) correspond to the localized intense electric field. The holes forms at the right end of z and are destroyed as they move to the left end of of the graph.

with grids of 2048×1024, 100 particles per cell, and up to a total of 2×10^8 particles; and (2) a 3D simulation with higher temperature than that described above, $T_e = T_i = 0.16$ (normalized to $m_i c_A^2$). Compared to the above 3D simulations, no turbulence appear in either the 2D or the high temperature 3D simulations, though strong electron beams also form around the x-line. In the 2D simulations, the growth of current driven perturbations is not allowed since $\mathbf{k} \cdot \mathbf{v}_{de} = 0$. In the high temperature simulations, the beam velocity around the x-line reaches a maximum value $v_{de} = 10c_A$ at the end of the simulation $t = 4\Omega_i^{-1}$. This is 2.5 times $v_{e,th}$, close to the threshold of Buneman instability (Papadopoulos 1977). Therefore no instabilities developed within the duration of the simulation.

The major difference between the non-turbulent and turbulent magnetic re-

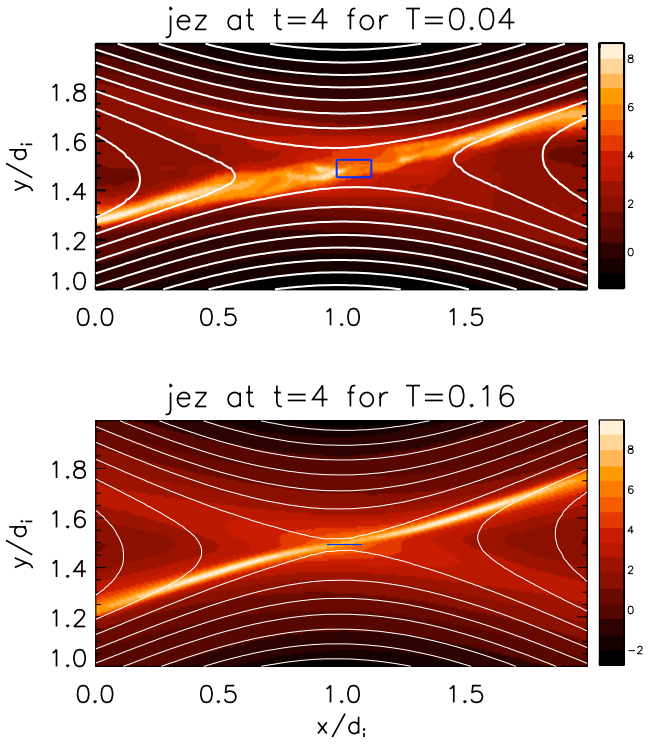

Figure 3.5: The electron current density j_{ez} (normalized to $cB_0/4\pi d_i$, averaged over z) in $x-y$ plane at $t = 4\Omega_i^{-1}$. The white lines are the magnetic field lines (averaged over z). The top is from the 3D simulations with $T_e = T_i = 0.04$. This image is averaged over 100 time steps, about $0.05\Omega_i^{-1}$. The blue square is the broadened electron current sheet at the x-line. The bottom is from the 3D simulations with $T_e = T_i = 0.16$. This image is averaged over 200 time steps, about $0.1\Omega_i^{-1}$.

connection is that the x-line in the turbulent magnetic reconnection is much broader than in non-turbulent reconnection, In Fig. 3.5, the blue square in the upper panel shows the maximum area of the current sheet around the x-line when the length of the square is fixed (the x-point is the center of the square). The blue square in the lower panel is with the same length as the blue square in the upper panel, but the width is very small because the current sheet is very thin in the high temperature reconnection.

At late time, two different spatial structures of electric field form in the $x-z$ plane: the intense round holes and oblique strips compared to the early elongated features shown. Fig. 3.6 shows the spatial structure of the electric field E_x and E_z in the $x-z$ plane in the middle of the current sheet at $t = 3\Omega_i^{-1}$. The intense round holes appear in both the electric field E_x and E_z while oblique strips are more significant in the image of E_x. The left half of the $x-z$ plane is around the x-line and the right half is around the island. Our study is focused on the x-line where the physics determines the reconnection rate.

3.2 Turbulence Effects in Guide-Field Magnetic Reconnection

The turbulence induced-dissipation acts as a drag on streaming electrons. In this section, I will focus on showing the impacts of the turbulence on the electron diffusion region as Buneman instabilities develop in reconnection simulations.

Because of the limited number of particles, the simulations contain significant computational noise which could contaminate the fluctuations from turbulence. For-

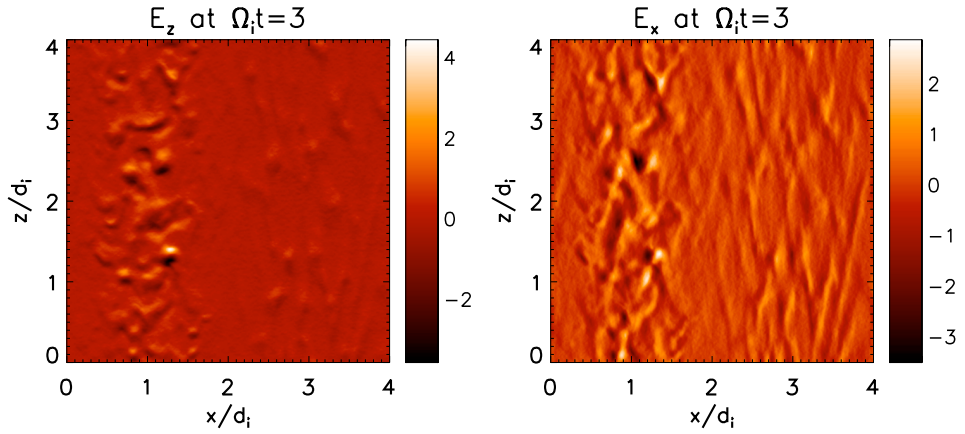

Figure 3.6: Spatial structures of electric field E_x and E_z in the mid-plane of current sheets at time $t = 3\Omega_i^{-1}$. The x-line is around $x/d_i = 1$.

tunately, the fluctuations generated by turbulence are intrinsically correlated while the computational noise is random with most of the power at high frequency. These random signals can be eliminated by averaging over time. For these reasons, we average important quantities such as the reconnection electric field, density, pressure and current density over z, and over a large number of time steps.

3.2.1 High Temperature Reconnection Simulation

First, we examine the results of the 3D high temperature simulation ($T_e = T_i = 0.16$). As noted in previous section, no turbulence develops. The reconnection geometry is independent of z and we can use a z-average to approximate an ensemble-average. The z-averaged z-component of the generalized Ohm's Law in

equation (1.21) is:

$$\overline{n}_e\overline{E}_z \simeq -m_e\overline{n}_e\frac{\partial\overline{U}_{ez}}{\partial t} - (\frac{\partial\overline{\mathcal{P}}_{exz}}{\partial x} + \frac{\partial\overline{\mathcal{P}}_{eyz}}{\partial y})$$
$$-m_e\overline{n}_e(\overline{U}_{ex}\frac{\partial\overline{U}_{ez}}{\partial x} + \overline{U}_{ey}\frac{\partial\overline{U}_{ez}}{\partial y}) + \frac{1}{c}(\overline{j}_{ex}\times\overline{B}_y - \overline{j}_{ey}\times\overline{B}_x), \tag{3.2}$$

where $\mathcal{P}_{exz}$ and $\mathcal{P}_{eyz}$ are generally called the non-gyrotropic pressure because at the x-line the coordinate z is aligned with the local magnetic field. If the pressure is projected onto the magnetic field line, the parts of parallel and perpendicular to the magnetic field are called gyrotropic pressure, the reminder is called the non-gyrotropic pressure.

Using the data averaged over 200 time-steps, every term of equation 3.2 is calculated as a function of y averaged over a small region around the x-line (20 grids). The results are displayed in Fig. 3.7 at two different times. At $t = 4\Omega_i^{-1}$, the non-gyrotropic pressure term (pink line) makes the primary contribution to balance the reconnection electric field at the x-line. The Ohm's law at late time can be approximated by

$$\overline{n}_e\overline{E}_z \sim -\frac{\partial\overline{\mathcal{P}}_{exz}}{\partial x} - \frac{\partial\overline{\mathcal{P}}_{eyz}}{\partial y}. \tag{3.3}$$

The convective portion of the inertia (green line) which peaks at both sides of the peak of the pink line is caused by the inflow of cold electrons (Swisdak et al. 2005; Ricci et al. 2002). The inertia (blue line) is close to zero.

However, at $t = 2\Omega_i^{-1}$, the inertia dominates (blue line) while the non-gyrotropic pressure and convection are negligible. Thus, the Ohm's law at early time can be approximated by

$$\overline{n}_e\overline{E}_z \sim -m_e\overline{n}_e\frac{\partial\overline{U}_{ez}}{\partial t}. \tag{3.4}$$

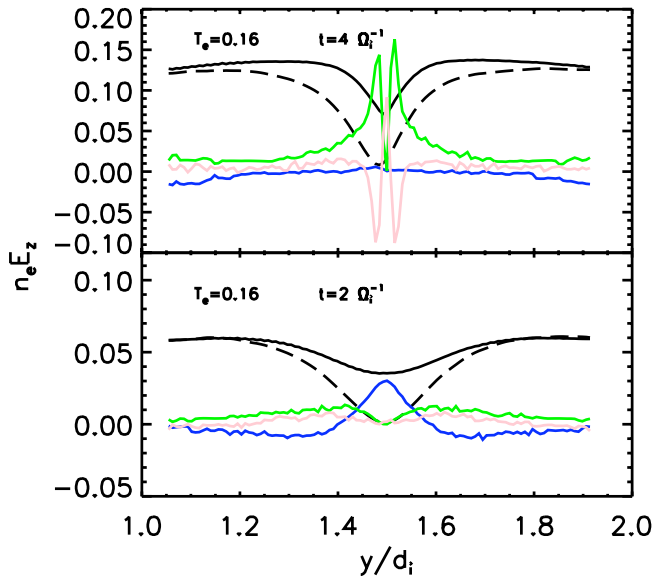

Figure 3.7: High temperature non-turbulent 3D simulation (averaged over 200 time steps): cuts through the x-line showing various terms balancing the electric force in equation (3.2). The top figure is at $t = 4\Omega_i^{-1}$. The electric force (black solid line) is balanced by the divergence of the non-gyrotropic pressure (pink line) at the x-line. The bottom is at $t = 2\Omega_i^{-1}$, the electric force is balanced by the inertia (blue line) at the x-line. The green line denotes the convective inertia, and the black dashed line denotes the z component of $\mathbf{j}_e \times \mathbf{B}$.

Initially, the homogenous density and temperature cause the divergence of the non-gyrotropic pressure to be zero. The simulation clearly shows the evolution of the non-gyrotropic pressure and convective inertia. The evolution of the convective inertia term is caused by the increase of the inflow of electrons to the x-line. The cause for the rise of the non-gyrotropic pressure has been discussed by Hesse et al (Hesse et al. 2004).

3.2.2 Low Temperature Reconnection Simulation

To demonstrate the effects of turbulence, we approximate the Ohm's law for low temperature reconnection as follows:

$$\overline{n}_e\overline{E}_z \sim -m_e\overline{n}_e\frac{\partial\overline{U}_{ez}}{\partial t} - (\frac{\partial\overline{\mathcal{P}}_{exz}}{\partial x} + \frac{\partial\overline{\mathcal{P}}_{eyz}}{\partial y})$$
$$-m_e\overline{n}_e(\overline{U}_{ex}\frac{\partial\overline{U}_{ez}}{\partial x} + \overline{U}_{ey}\frac{\partial\overline{U}_{ez}}{\partial y}) + \overline{\delta n\delta E_z} + \frac{1}{c}(\bar{j}_{ex}\overline{B}_y - \bar{j}_{ey}\overline{B}_x), \tag{3.5}$$

where $\overline{\delta n\delta E_z}$ comes from the z-average term $\overline{n_eE_z} \approx \overline{n_e}\overline{E_z} + \overline{\delta n_e\delta E_z}$. This is the turbulence drag force, which reflects the interactions between waves and particles, and is the most important electrostatic turbulent effect.

To evaluate Ohm's law, the simulation data is averaged over 100 time-steps and over 20 gridpoints in the x-direction around the x-line. The time steps cover a total time interval of $0.05\Omega_i^{-1}$. This time scale is small compare to the instability growth time and the evolution time of the overall reconnection pattern.

Fig. 3.8 shows the terms in equation (3.5) as a function of y, the inflow direction. The top three panels show the results of the 3D simulations at t = 4,3.5,2 Ω_i^{-1}. They indicate that the inertial term becomes less and less important with time

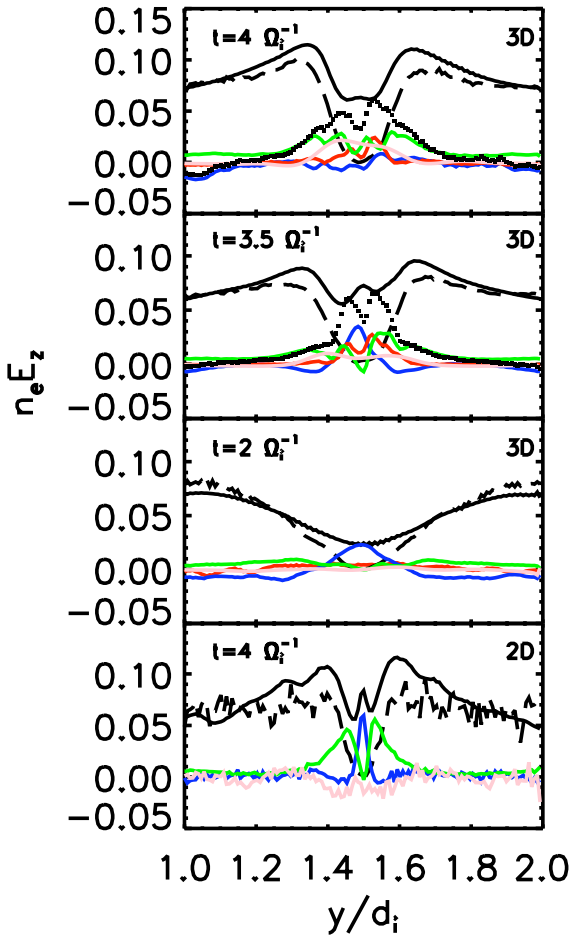

Figure 3.8: Low temperature turbulent 3D simulations (averaged over 100 time steps): cuts through the x-line showing various terms balancing the electric force in equation (3.5). The top three are from 3D simulations at time $t = 4, 3.5, 2\Omega_i^{-1}$, and the bottom is from a 2D simulation at $t = 4\Omega_i^{-1}$. $\overline{n}_e\overline{E}_z$ is shown by the solid black lines. The blue, red, green and pink lines denote the inertia, drag force, convective inertia term and the divergence of non-gyrotopic pressure. The dashed lines denote the $(\mathbf{j}_e \times \mathbf{B})_z$ term. The black squares in the top two panels denote the total of all of the colored lines.

while the turbulence becomes more and more important. At $t = 2\Omega_i^{-1}$, prior to the onset of the Buneman instability, the resemblance to the 3D high temperature simulation is clearly seen: inertia supports the reconnection field and the other terms are almost zero. At $t = 3.5\Omega_i^{-1}$, the instability has reached its peak and the turbulence effects appear: the drag force, convective inertia term and the divergence of non-gyrotropic pressure grow strong enough to compete with the inertia ($m_e\overline{n}_e\frac{\partial\overline{U}_{ez}}{\partial t}$). As the bulk energy of electrons at the x-line is being dissipated into heat by the strong exchange of energy between the resonant electrons and waves, the acceleration of electrons decreases and as a result the inertia ($m_e\overline{n}_e\frac{\partial\overline{U}_{ez}}{\partial t}$) decreases. The growth of waves increases the drag force. The turbulent heating along the magnetic field (close to z direction) raises the z component of the temperature and also raises the contribution from the pressure. The strong turbulence induces strong diffusion of particles around the x-line which broadens and blurs the x-line. This causes the peaks of the convective inertial and divergence of the pressure tensor around x-line to broaden. At $t = 4\Omega_i^{-1}$, the turbulence effects dominate and inertia goes down to zero. Compared to the high temperature ($T_e = 0.16$) simulation, the drag force varies around the x-line, indicating that strong spatial correlations among particles have built up, and the x-line becomes very blurred and asymmetric (Fig.3.5). The variation of the non-gyrotropic pressure around the x-line becomes smoother than the corresponding non-gyrotropic pressure in the high temperature reconnection simulation. Similarly, the two peaks of convection term become much broader, indicating very intense thermal energy and momentum transport are taking place around x-line. Away from the x-line, the $\mathbf{j}_e \times \mathbf{B}$ term balances the electric field.

For comparison, we also show the results from the low temperature 2D simulation at $t = 4\Omega_i^{-1}$ in the bottom panel of figure 3.8. In this case, the inertia dominates equation (3.5) and the equation reduces to $\overline{E}_{ez} \simeq -m_e \dfrac{\partial \overline{U}_{ez}}{\partial t}$ at x-line.

We further illustrate the evolution of the turbulence by showing in Fig. 3.9 the time evolution of each term in equation (3.5) around the x-point. The data are averaged over the blue box shown in Fig 3.5. In the 3D low temperature simulation (the top panel), it is clear that the drag force and the convection term go up together around $t = 3\Omega_i^{-1}$ when the Buneman instability occurs, reach their peaks around $t = 3.3\Omega_i^{-1}$, and then decay. The pressure divergence also increases after the onset of the instability. The deceleration of the electron bulk motion caused by turbulence heating can be seen in the decrease of the inertia term at late time. The contribution from the $\mathbf{j}_e \times \mathbf{B}$ term is ~ 0, the small deviation is caused by the magnetic field inside the blue box not being exactly zero. On the other hand, in 2D low temperature simulations, the acceleration of electrons goes up with time and the inertial term balances the electric field (figure 3.9, lower panel).

To depict the turbulence effects on the non-gyrotropic pressure, the vector fields of $\overline{\mathcal{P}}_{exz}$ and $\overline{\mathcal{P}}_{eyz}$ around the x-line in the low temperature simulations are displayed in Fig. 3.10. At $t = 2\Omega_{ci}^{-1}$, the non-gyrotropic pressure field appear very random in the 2D simulation, but already show vortices in the 3D simulation. At $t = 4\Omega_{ci}^{-1}$, structures in the vector fields in both 2D and 3D simulations can be identified. In the 2D simulation, the vector fields are parallel, and the divergence of the non-gyrotropic pressure around the x-line ($(x, y) \sim (1.05, 1.49)$) is close to zero. In the 3D simulations, the vectors are bent by turbulence around the x-line

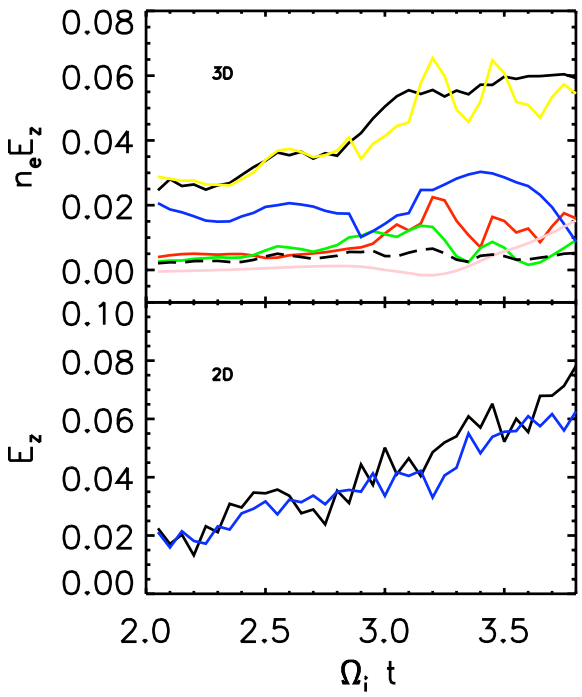

Figure 3.9: Low temperature simulations (averaged over 100 time steps): time evolutions of various term in equation (3.5). The top from 3D and the bottom from 2D for reference. In 3D, the black solid line denotes the electric force. The red, green, pink lines denote the drag force, the convective inertia term and the divergence of the non-gyrotropic pressure. The inertia is shown by the blue line. The black dashed line is for the term $(\mathbf{j}_e \times \mathbf{B})_z$. The total of all of the terms supporting electric force in equation (3.5) is shown by the yellow line. In 2D Ohm's law at the x-line is reduced to $m_e \dfrac{\partial \overline{U}_{ez}}{\partial t} = -\overline{E}_z$. The solid black line is electric field and the blue line is the inertia.

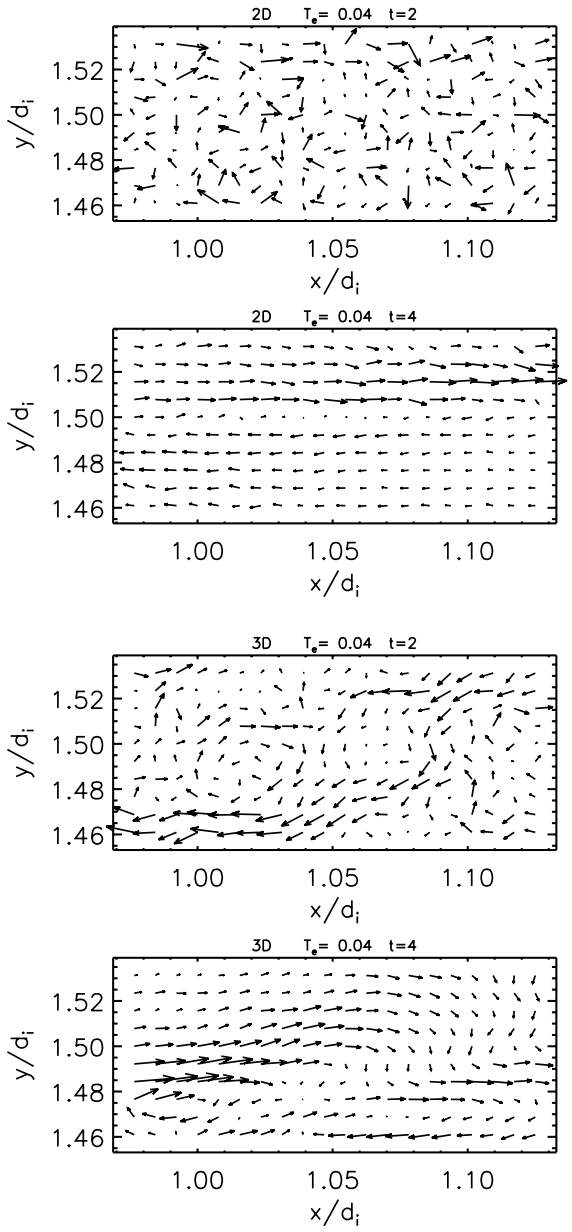

Figure 3.10: The vector fields of $\overline{\mathcal{P}}_{exz}$ and $\overline{\mathcal{P}}_{eyz}$ around the x-line. The top two panels are from 2D low temperature simulations and the bottom two from the 3D low temperature simulations.

$((x, y) \sim (1.05, 1.49))$. At $\Omega_i t = 2$, the vectors entering the x-line and the vectors going out of the x-line seem to balance so the divergence of P_{exz} and P_{eyz} is close to zero. At $\Omega_i t = 4$, the vectors entering the x-line from the upper left are larger than the vectors leaving from the lower right. Thus the total flux enters the x-line, and the divergence of non-gyrotropic pressure is negative, which is the sign required to balance the reconnection electric field.

3.3 Problems in Turbulent Guide-Field Reconnection

In turbulent reconnection, the drag force is an important indicator of the role of turbulence. However, it is unclear what causes the evolution of the non-gyrotropic pressure in both high and low temperature 3D simulations. In the case of low temperature 2D reconnection with a strong guide field the non-gyrotropic pressure is negligible. It is also unclear why turbulence broadens the dissipation region.

To answer these questions, we must address the nature of the instabilities that develop during reconnection and how they impact the electron dynamics near the x-line. The linear theory of the Buneman instability can not explain the nonlinear evolution.

In Fig. 3.3, the green part of the electron distribution function of $f(v_z)$ shows the location where electrons resonate with the waves driven by the Buneman instability. However, beyond the green part, the electrons also have strong resonant interactions with waves at much higher velocity, from $v_z \sim -5$ to $-15c_A$ and cause

the distortion of $f(v_z)$ from that which is expected from a Maxwellian accelerated by a parallel electric field. The kinetic energy of high velocity electrons is channelled into heat and the energetic electrons are dragged toward lower velocity. It is unclear what instabilities are responsible for this behavior. From Fig. 3.6, we see the strip-like structures. Are these structures caused by the oblique Buneman instability or by some other instability? We observe that electron holes have different velocities, why? What instabilities continuously produce new electron holes?

Linear kinetic theory can help us interpret time local simulation behavior if we know the particle velocity distribution functions at that time. Particle-in-cell simulations provide us the evolved distribution functions so that it is possible for us to combine the simulations and linear theory to investigate the turbulence. Understanding the development of these instabilities is the key to making progress on turbulence heating and energy transport. In next chapter, I will explore in great detail the nature of the instabilities that develop.

Chapter 4

Nonlinear Development of Streaming Instabilities in Low β Plasma

In Chapter II, the linear theory of streaming instabilities was introduced. In Chapter III, PIC simulations of magnetic reconnection with strong guide field were presented. The Buneman instability occurs around the x-line at early time in the 3D low temperature magnetic reconnection simulations. At late time, the streaming instabilities have deviated from the linear Buneman instability whose low phase speed can't produce a wave-electron resonance at high velocity. The nonlinear evolution after the saturation of the Buneman instability will be discussed in this chapter using kinetic theory and PIC simulations.

In magnetic reconnection, the inductive electric field accelerates the particles around the x-line, and the $\mathbf{E}\times\mathbf{B}$ and the thermal streaming velocities drive the particles away from the x-line. This complex behavior makes it difficult to understand the development of streaming instabilities. To separate the effects of reconnection from the development of streaming instabilities, we carry out new 3D PIC simulations of streaming instabilities driven in a current sheet similar to that around the x-line in magnetic reconnection. The development of streaming instabilities are studied for two cases $\omega_{pe}/\Omega_e < 1$ and $\omega_{pe}/\Omega_e > 1$.

To investigate the nonlinear development of instabilities and to trace the evo-

lution of instability, we construct a double Maxwellian model to fit the distribution functions measured at different times in the simulations, and then substitute the modeled distribution function into the dispersion relation to obtain the unstable modes. In the case of $\omega_{pe}/\Omega_e < 1$, two distinct phases of the dynamics are discovered. In the first the parallel Buneman instability grows and traps the lower velocity streaming electrons. In the second the high velocity electrons drive two distinct forms of turbulence: the parallel electron-electron two-stream instability and the lower hybrid instability. The high parallel phase speed of these waves allows them to resonate with high energy electrons and transfer momentum to the ions and low velocity electrons. The electron two-stream instabilities continuously sustain the electron holes while the lower hybrid instability causes the perpendicular interactions between ions and waves which lead to transverse heating of the ions. In the case of $\omega_{pe}/\Omega_e > 1$, the evolution time scale is shorter than that in the case of $\omega_{pe}/\Omega_e < 1$ since the growth rate of the various instabilities scale with ω_{pe}. Three evolution stages are revealed. In the first stage the Buneman instability grows and decays sharply. In the second stage, the medium velocity electrons drive the lower hybrid instability and electron-electron two-stream instability. The lower hybrid instability dominates during this stage. In the third stage, the high velocity electrons drive the lower hybrid instability, which prevents the growth of the electron two-stream instability. Instead, the Buneman instability reappears. The overlapping of resonance velocity of the lower hybrid instability and the Buneman instability enables momentum to be transferred from the high velocity electrons to low velocity electrons. This stochastic process in phase space sustains the growth

of the Buneman instability and weakens the lower hybrid instability.

4.1 Double-Drifting Maxwellian Model

Collective wave-particle interactions lead to a peak on the velocity distribution which can be approximated by a Maxwellian distribution function. This indicates that the multiple-Maxwellian function should fit the evolving velocity distribution which is distorted by the turbulence thermalization. A double-drifting Maxwellian is a simple model, but is found to be quite accurate.

4.1.1 Double-drifting Distribution Function and Dispersion Relation

The general dispersion relation of electrostatic waves in magnetized plasma can be written as (see Chapter 2):

$$1 + \sum_j \chi_j = 0,$$

$$\chi_j = \frac{\omega_{pj}^2}{k^2} \sum_{n=-\infty}^{n=\infty} \int d^3v \frac{J_n^2(\frac{k_\perp v_\perp}{\Omega_j})}{\omega - n\Omega_j - k_z v_z} (k_z \frac{\partial f_{j0}}{\partial v_z} + \frac{n\Omega_j}{v_\perp} \frac{\partial f_{j0}}{\partial v_\perp}). \tag{4.1}$$

where f_{j0} is the distribution function of species j and normalized by the ambient density and χ_j is the dielectric response of species j. $Im(\omega) > 0$ is assumed. The parallel direction is along the constant magnetic field $\mathbf{B} = B\hat{z}$, $k^2 = k_z^2 + k_\perp^2$, $v^2 = v_z^2 + v_\perp^2$, and $\Omega_j = e_j B/cm_j$. J_n is the Bessel function of the first kind with order n.

A species is considered unmagnetized when perturbations are considered with perpendicular wavelength much shorter than the characteristic thermal Larmor ra-

dius of the species ($r_{Lj} = v_{tj}/\Omega_j$) and frequency much larger than the cyclotron frequency of the species, i.e. $k_\perp v_\perp/\Omega_j \gg 1$ and $\omega/\Omega_j \gg 1$. Then the corresponding dielectric response can be approximated by (see Chapter 2):

$$\chi_j = \frac{\omega_{pi}^2}{k^2} \int d^3\mathbf{v} \frac{\mathbf{k} \cdot \partial f_{j0}/\partial \mathbf{v}}{\omega - \mathbf{k} \cdot \mathbf{v}} \tag{4.2}$$

To analyze our simulations, we need simplify the dispersion relation (4.1) for species of ions and electrons. The first important step is to construct reasonable distribution functions for the ions and electrons. In our simulations electron distribution functions are more strongly distorted than those of the ions, since the bounce frequency of electrons in resonant waves is much higher than that of ions. Therefore, a double-drifting Maxwellian is chosen for electrons and single-drifting Maxwellian is chosen for ions:

$$\begin{aligned} f_i &= \frac{\mathbf{e}^{\frac{-v_\perp^2}{v_{ti}^2}}}{\pi^{3/2} v_{ti}^3} \mathbf{e}^{-\frac{(v_z - v_{di})^2}{v_{ti}^2}}, \\ f_e &= \frac{\mathbf{e}^{\frac{-v_\perp^2}{v_{\perp te}^2}}}{\pi^{3/2} v_{\perp te}} \left[\frac{1-\delta}{v_{zte1}^2} \mathbf{e}^{-\frac{(v_z - v_{de1})^2}{v_{zte1}^2}} + \frac{\delta}{v_{zte2}^2} \mathbf{e}^{-\frac{(v_z - v_{de2})^2}{v_{zte2}^2}} \right]. \end{aligned} \tag{4.3}$$

where δ is ratio of the weight of the two drifting Maxwellian of electrons, $v_{\perp te}^2 = 2T_{\perp e}/m_e$, $v_{zte1}^2 = 2T_{ze1}/m_e$, and $v_{zte2}^2 = 2T_{ze2}/m_e$, v_{de1} and v_{de2} are electron drifts. $v_{t_i}^2 = \frac{2T_i}{m_i}$ and v_{di} is the ion drift.

We replace f_{i0} and f_{e0} in equation (4.1) by the ion and electron drifting Maxwellian distribution functions in equation (4.3). Assuming the ions are unmagnetized and the electrons are magnetized, using $\mathbf{k} \cdot \mathbf{v}/(\omega - \mathbf{k} \cdot \mathbf{v}) = 1 - \omega/(\omega - \mathbf{k} \cdot \mathbf{v})$

for both ions and electrons, and integrating, we obtain

$$
\begin{aligned}
1 + \chi_i + \chi_{e1} + \chi_{e2} &= 0, \\
\chi_i &= \frac{2\omega_{pi}^2}{k^2 v_{ti}^2}[1 + \eta_i Z(\eta_i)], \\
\chi_{e1} &= \frac{2(1-\delta)\omega_{pe}^2}{k^2 v_{te1}^2}[1 + I_0(\lambda)e^{-\lambda}\zeta_1 Z(\zeta_1) + \zeta_1 \sum_{n\neq 0}(e)^{-\lambda} I_n(\lambda) Z(\xi_1)], \\
\chi_{e2} &= \frac{2\delta\omega_{pe}^2}{k^2 v_{te2}^2}[1 + I_0(\lambda)e^{-\lambda}\zeta_2 Z(\zeta_2) + \zeta_2 \sum_{n\neq 0}(e)^{-\lambda} I_n(\lambda) Z(\xi_2)]. \qquad (4.4)
\end{aligned}
$$

where $\eta_i = (\omega - k_z v_{iz})/k v_{ti}$, $\zeta_1 = (\omega - k_z v_{z1})/k_z v_{zte1}$, $\zeta_2 = (\omega - k_z v_{z2})/k_z v_{zte2}$, $\lambda = k_\perp^2 v_{\perp te}^2/2\Omega_e^2$, Ω_e is the local electron cyclotron frequency, and $\xi_1 = (\omega - k_z v_{z1} - n\Omega_e)/k_z v_{te1}$, $\xi_2 = (\omega - k_z v_{z2} - n\Omega_e)/k_z v_{te2}$. Z is the plasma dispersion function and I_n is the modified first kind Bessel function of order n. These two function are defined as

$$
\begin{aligned}
Z(\eta) &\equiv \pi^{-1/2}\int_{-\infty}^{\infty} dx \frac{\mathbf{e}^{-x^2}}{x-\eta} \\
\int_0^\infty x J_n^2(sx)\mathbf{e}^{-x^2} dx &\equiv \frac{\mathbf{e}^{-s^2}}{2} I_n(s^2/2) \qquad (4.5)
\end{aligned}
$$

where I_n is the modified Bessel function of order n.

In equation (4.4), no approximation has been made. We now assume that the electrons are strongly magnetized so that the perpendicular wavelength is long comparing to the thermal electron Larmor radius $r_{Le} = v_{\perp te}/\Omega_e$, i.e. $\lambda = \frac{k_\perp^2 r_{Le}^2}{2} \ll 1$. With this assumption, the summation of Bessel functions of non-zero order in χ_{e1} and χ_{e2} can be neglected. The dispersion relation simplifies to

$$
\begin{aligned}
&1 + \frac{2\omega_{pi}^2}{k^2 v_{ti}^2}[1 + \eta_i Z(\eta_i)] \\
&+ \frac{2(1-\delta)\omega_{pe}^2}{k^2 v_{te1}^2}[1 + I_0(\lambda)e^{-\lambda}\zeta_1 Z(\zeta_1)] + \frac{2\delta\omega_{pe}^2}{k^2 v_{te2}^2}[1 + I_0(\lambda)e^{-\lambda}\zeta_2 Z(\zeta_2)] = 0 \qquad (4.6)
\end{aligned}
$$

Equation (4.6) reduces to the dispersion relation of the two-fluid plasma model (cold plasma limit) when the temperature is sufficiently low so that $\omega - k_z v_{de} \gg k_z v_{zte}$ and the electrons are sufficiently strongly magnetized with $\omega - k_z v_{de} \ll \Omega_e$. Furthermore the modified Bessel function $I_0 e^{-\lambda}$ reduces to $1 - \lambda$ for $\lambda \ll 1$ and the plasma dispersion function $\zeta Z(\zeta)$ to $-1 - 1/2\zeta^2$ for $\zeta \gg 1$. The cold plasma dispersion relation is then obtained (let $\delta = 0$):

$$1 - \frac{\omega_{pi}^2}{\omega^2} + \frac{sin^2\theta\omega_{pe}^2}{\Omega_e^2} - \frac{cos^2\theta\omega_{pe}^2}{(\omega - k_z v_{de})^2} = 0 \tag{4.7}$$

There are two distinct cases for the roots of the cold plasma dispersion relation. One is for parallel propagation and the other is nearly perpendicular propagation. In the limit of $\theta \sim 0$, the Buneman instability (Galeev & Sagdeev 1984b) peaks around $k_{fg} v_{de} \sim \omega_{pe}$, with a frequency $Re(\omega) = \frac{k_{fg}}{2}(\omega_{pi}^2/2\omega_{pe}^2)^{\frac{1}{3}}|v_{de}|$ and a maximum growth rate $\gamma = \sqrt{3}\omega_{pe}(\omega_{pi}^2/2\omega_{pe}^2)^{\frac{1}{3}}$, where the subscript fg denote the fast-growing mode. The other maximum mode is the lower hybrid instability. It is nearly perpendicularly propagating with $cos\theta \sim \sqrt{m_e/m_i}$, where $\omega = \omega_{pi}/(1 + \omega_{pe}^2/\Omega_e^2)^{1/2}$.

4.1.2 Group Velocity of Perturbations and Turbulent Field Angle

The group velocity of waves is the velocity with which the variations in the envelopes of wave amplitude propagate through space. It is defined as $v_g \equiv \nabla_{\mathbf{k}}\omega(\mathbf{k})$, where $\nabla_{\mathbf{k}}$ is the gradient in $\mathbf{k}$ space and $\omega(\mathbf{k})$ is the dispersion relation (Stix 1962). To calculate the group velocity from the dispersion relation (4.6), we assume without loss of generality that the $\mathbf{k}$ vector lies in the $x-z$ plane, and express $\mathbf{k} = (k_x, 0, k_z)$. The group velocity can be computed from equation (4.6) using $\mathbf{v_g} = \hat{\mathbf{e}}_z \frac{\partial\omega}{\partial k_z} + \hat{\mathbf{e}}_x \frac{\partial\omega}{\partial k_x}$.

Some useful relations and equations are used during the derivation:

$$\partial I_0(\lambda)/\partial\lambda = I_1(\lambda),$$

$$\partial Z(\eta)/\partial\eta = -2(1+\eta Z(\eta)), \tag{4.8}$$

and

$$\begin{aligned}
\nabla_{\mathbf{k}}\frac{1}{k} &= -\frac{k_x}{k^3}\hat{\mathbf{e}}_x - \frac{k_z}{k^3}\hat{\mathbf{e}}_z,\\
\nabla_{\mathbf{k}}\frac{1}{k^2} &= -\frac{2k_x}{k^4}\hat{\mathbf{e}}_x - \frac{2k_z}{k^4}\hat{\mathbf{e}}_z,\\
\nabla_{\mathbf{k}}\omega &= v_{gx}\hat{\mathbf{e}}_x + v_{gz}\hat{\mathbf{e}}_z,\\
\nabla_{\mathbf{k}}k_x &= \hat{\mathbf{e}}_x, \nabla_{\mathbf{k}}k_z = \hat{\mathbf{e}}_z,\\
\nabla_{\mathbf{k}}\eta_i &= (\frac{v_{gx}}{kv_{ti}} - \frac{\omega k_x}{k^3 v_{ti}})\hat{\mathbf{e}}_x + (\frac{v_{gz}}{kv_{ti}} - \frac{\omega k_z}{k^3 v_{ti}})\hat{\mathbf{e}}_z,\\
\nabla_{\mathbf{k}}\zeta_1 &= \frac{v_{gx}}{kv_{zte1}}\hat{\mathbf{e}}_x + \frac{1}{k_z v_{zte1}}(v_{gz} - \frac{\omega}{k_z})\hat{\mathbf{e}}_z,\\
\nabla_{\mathbf{k}}\zeta_2 &= \frac{v_{gx}}{kv_{zte2}}\hat{\mathbf{e}}_x + \frac{1}{k_z v_{zte2}}(v_{gz} - \frac{\omega}{k_z})\hat{\mathbf{e}}_z,\\
\nabla_{\mathbf{k}}\lambda &= \frac{v_{tex}^2 k_x}{\Omega_e^2}\hat{\mathbf{e}}_x.
\end{aligned} \tag{4.9}$$

The resulting expression for the group velocity is

$$\begin{aligned}
v_{gx} &= v_{de1}\frac{\frac{\alpha x_\omega sin\theta}{\alpha_i^3}A + \frac{2\alpha\beta sin\theta}{\alpha_i^2}B + 2\beta sin\theta C + sin\theta\beta e^{-\lambda}(2I_0 - \frac{\alpha_{ex}^2\beta^2\omega_{pe}^2}{\Omega_e^2}(I_1 - I_0))D}{\frac{\alpha\beta}{\alpha_i^3}A + \frac{\beta I_0 e^{-\lambda}}{cos\theta}E},\\
v_{gz} &= v_{de1}\frac{\frac{\alpha x_\omega cos\theta}{\alpha_i^3}A + \frac{2\alpha\beta cos\theta}{\alpha_i^2}B + 2\beta cos\theta C + 2cos\theta\beta I_0 e^{-\lambda}D + \frac{x_\omega\omega_{pe}}{\Omega_e cos^2\theta}I_0 e^{-\lambda}E}{\frac{\alpha\beta}{\alpha_i^3}A + \frac{\beta I_0 e^{-\lambda}}{cos\theta}E}.
\end{aligned} \tag{4.10}$$

where

$$A = Z(\eta_i) + \eta_i Z'(\eta_i),$$

$$B = 1 + \eta_i Z(\eta_i),$$

$$C = \frac{1-\delta}{\alpha_{ez1}^2} + \frac{\delta}{\alpha_{ez2}^2},$$

$$D = \frac{\zeta_1 Z(\zeta_1)(1-\delta)}{\alpha_{ez1}^2} + \frac{\zeta_2 Z(\zeta_2)\delta}{\alpha_{ez2}^2},$$

$$E = (Z(\zeta_1) + \zeta_1 Z'(\zeta_1))(1-\delta)/\alpha_{ez1}^3 + (Z(\zeta_2) + \zeta_2 Z'(\zeta_2))\delta/\alpha_{ez2}^3, \tag{4.11}$$

and

$$x_\omega = \omega/\omega_{pe}, \beta = kv_{de1}/\omega_{pe}, \alpha = \omega_{pi}^2/\omega_{pe}^2,$$

$$\alpha_i = v_{ti}/v_{de1}, \alpha_{ez1} = v_{te1}/v_{de1}, \alpha_{ez2} = v_{te2}/v_{de1}. \tag{4.12}$$

The angle ψ between the group velocity of the propagating waves and the magnetic field is given by

$$tan\psi = Re(v_{gx})/Re(v_{gz}) \tag{4.13}$$

4.2 Nonlinear Development of Streaming Instabilities In Low β Plasma with $\Omega_e/\omega_{pe} > 1$

4.2.1 Two Distinct Phases of Nonlinear Evolution

We carry out 3D PIC simulations with strong electron drift in an inhomogenous plasma with a strong guide field. The initial state mimics the current sheet near an

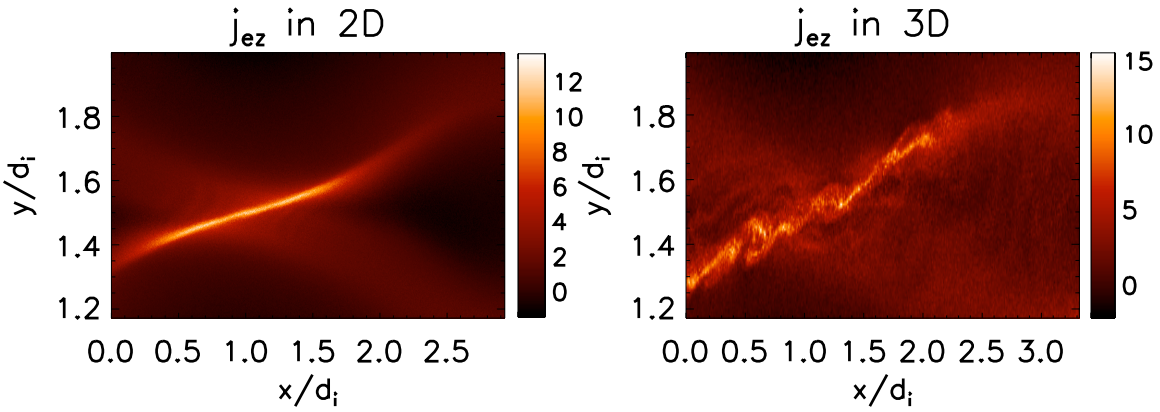

Figure 4.1: The current sheets in magnetic reconnection with a strong magnetic field at $\Omega_i t = 3$. In 2D simulations no turbulence develops while in 3D simulations strong turbulence develops around the x-line.

x-line at late time in 2D simulations of reconnection (Drake et al. 2003) as shown in Fig. 4.1.

Since we apply no external perturbations to initiate reconnection and the time scale for reconnection to occur naturally in the simulation is much longer than the growing time scale of other instabilities, reconnection does not develop. The initial conditions for our simulation are based on (Drake et al. 2003). We specify the reconnecting magnetic field to be $B_x/B_0 = \tanh[(y - L_y/2)/w_0]$, where B_0 is the asymptotic amplitude of B_x outside of the current layer, and w_0 and L_y are the half-width of the initial current sheet and the box size in the y direction, respectively. The guide field $B_z^2 = B^2 - B_x^2$ is chosen so that the total field B is constant. In our simulation, B is taken as $26^{1/2}B_0$. Thus, we are in the limit of a strong guide field such that $\Omega_e = 2.5\omega_{pe}$, where ω_{pe} is the electron plasma frequency. The initial temperature is $T_e = T_i = 0.04 m_i c_A^2$, the ion to electron mass ratio is 100, the speed of light c is $20c_A$, and $c_A = B_0/(4\pi n_0 m_i)^{1/2}$ is the Alfvén speed. The simulation domain

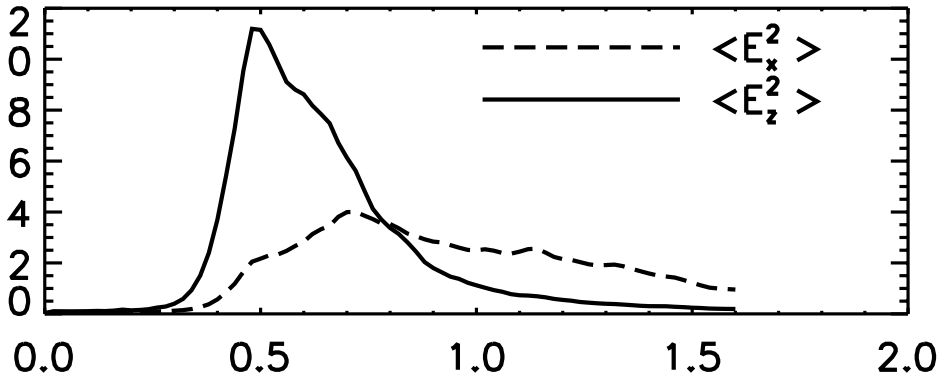

Figure 4.2: The time evolution of $\langle E_x^2 \rangle$ (dashed line) and $\langle E_z^2 \rangle$ (solid line) averaged over the midplane of the current sheet.

has dimensions $L_x = L_y = d_i = c/\omega_{pi}$, and $L_z = 8d_i$, where ω_{pi} is the ion plasma frequency. The initial electron drift along $\hat{z}$ is $10c_A$, close to that of the current layer around the x-line of 2D reconnection simulations reported earlier (Drake et al. 2003). The initial ion drift is $-0.9c_A$. The drift speed in these simulations is around three times the electron thermal speed $v_{te} \sim 3c_A$, above the threshold to trigger the Buneman instability.

Within an ion cyclotron period the intense electron stream drives a strong Buneman instability in our simulation. In Fig. 4.2, we show the time development of $\langle E_x^2 \rangle$ and $\langle E_z^2 \rangle$, where $\langle\rangle$ denotes an average over the midplane of the current sheet. As the instability develops, the Buneman waves clump to form localized electron holes (Fig. 4.3). At the same time, the electric field also becomes stretched and forms elongated oblique stripes in the $x - z$ plane. This behavior is reflected in the delayed growth of $\langle E_x^2 \rangle$ in Fig. 4.2.

In Fig. 4.3, we show snapshots of the components E_x and E_z of the electric field at the midplane of the current layer at $\Omega_i t = 0.4, 1.2$. At $\Omega_i t = 0.4$, some intense

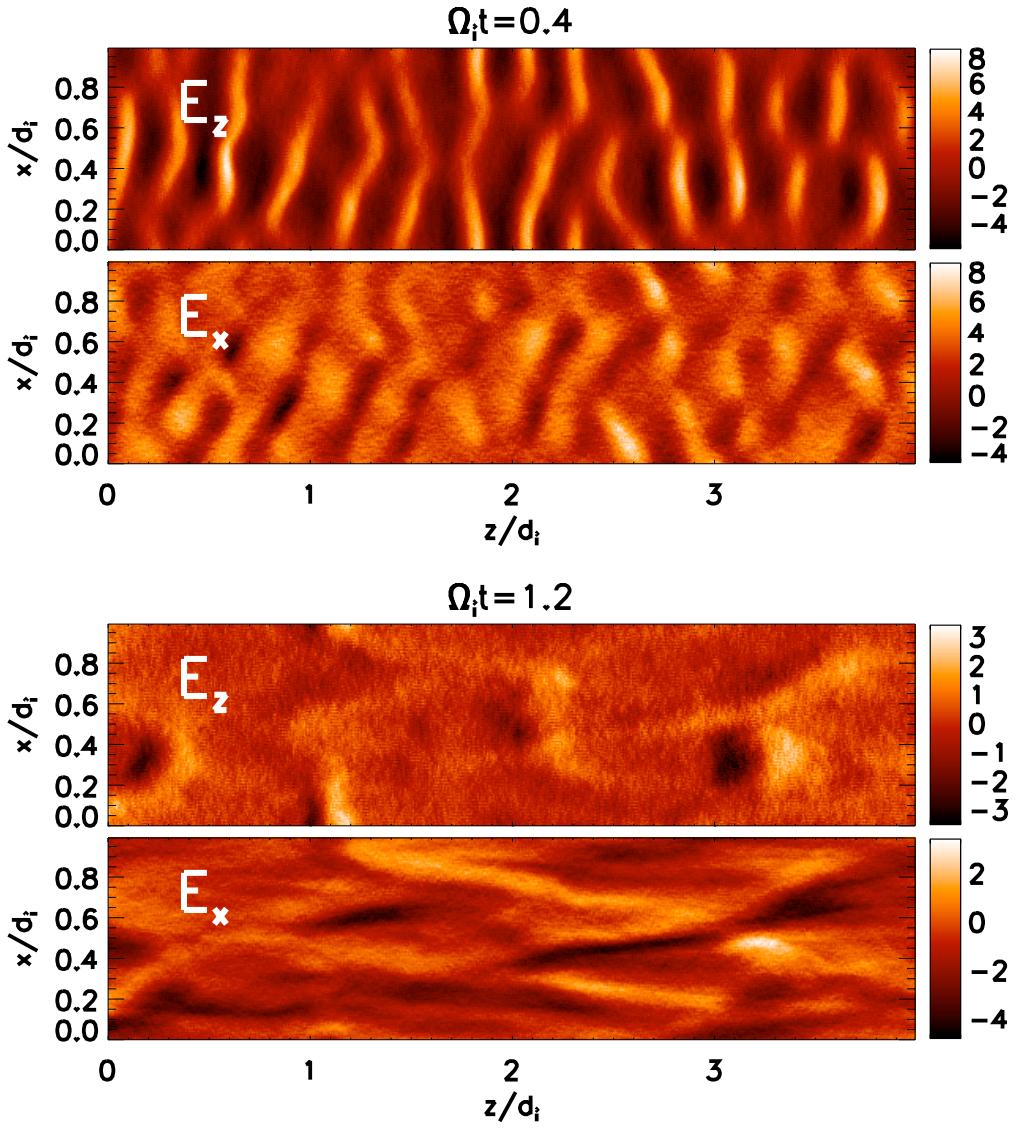

Figure 4.3: the spatial structure of the parallel electric field E_z and the transverse electric field E_x at $\Omega_i t = 0.4, 1.2$

long and thin layers of electric field E_x and E_z form along the x direction in the $x-z$ plane and move parallel to the magnetic field, approximately in the z direction. Some thin layers moving faster than others and overtake the ones before them, and at the same time break up into shorter layers along x and reform new spatial structures wider in z direction. We call these localized intense structures electron holes. The parallel speed of some electron holes reaches $8-10c_A$. This process continues until two distinct spatial structures finally appear at late time $\Omega_i t = 1.2$: the strongly localized structure (electron holes) and long oblique structures as seen in earlier magnetic reconnection simulations (Drake et al. 2003). Comparing the structures of E_x and E_z at $\Omega_i t = 0.4$ and $\Omega_i t = 1.2$, the differences are significant. At $\Omega_i t = 0.4$, the spatial structures of E_x and E_z are quite similar to each other though the E_x structures are not as localized in z. The wavelength in the x direction is very long which implies $k_x \sim 0$. At $\Omega_i t = 1.2$, the spatial structure of E_Z is dominated by the electron holes and E_x is dominated by the long oblique stripes whose $\mathbf{k}$ vectors are oriented about 80^0 relative to the magnetic field.

The power spectra (a) and (b) of E_x and E_z in Fig. 4.4 reveal that at $\Omega_i t = 0.4$ the power spectra of both E_x and E_z are peaked around $(k_x d_i, k_z d_i) \sim (0, 20)$ which corresponds to the electric field parallel layers in Fig. 4.3. In spectrum (d) of Fig 4.4, the wavenumber k_z of the nearly parallel mode deceases to $k_z d_i \sim 10$ and is broadly centered with a width $\Delta k_x d_i \sim 10$. This corresponds to the round electron holes at $\Omega_i t = 1.2$ in Fig. 4.3. At $\Omega_i t = 0.4$, a weak peak appear in the spectrum of E_x (in (a)) does not appearing in the spectrum of E_z (in (b)) around $(k_x d_i, k_z d_i) \sim (10, 5)$. This peak becomes stronger at $\Omega_i t = 1.2$ in the spectra of both E_x and E_z, but

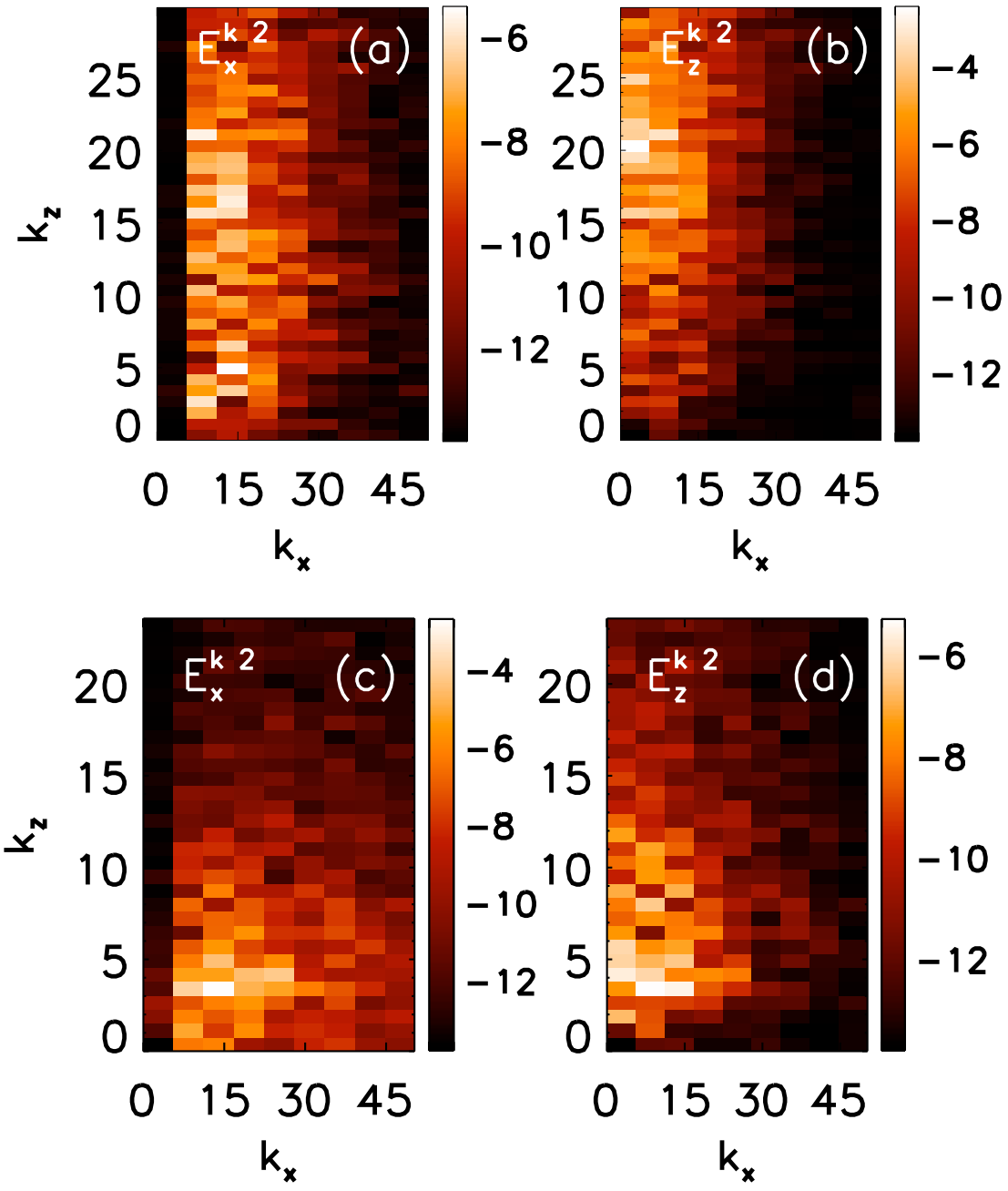

Figure 4.4: The 2D power spectra $|E_x(k_x, k_z)|^2$ and $|E_z(k_x, k_z)|^2$ of the parallel electric field E_z and the transverse electric field E_x at $\Omega_i t = 0.4$ in (a),(b) and 1.2 in (c), (d) shown on logarithmic scale.

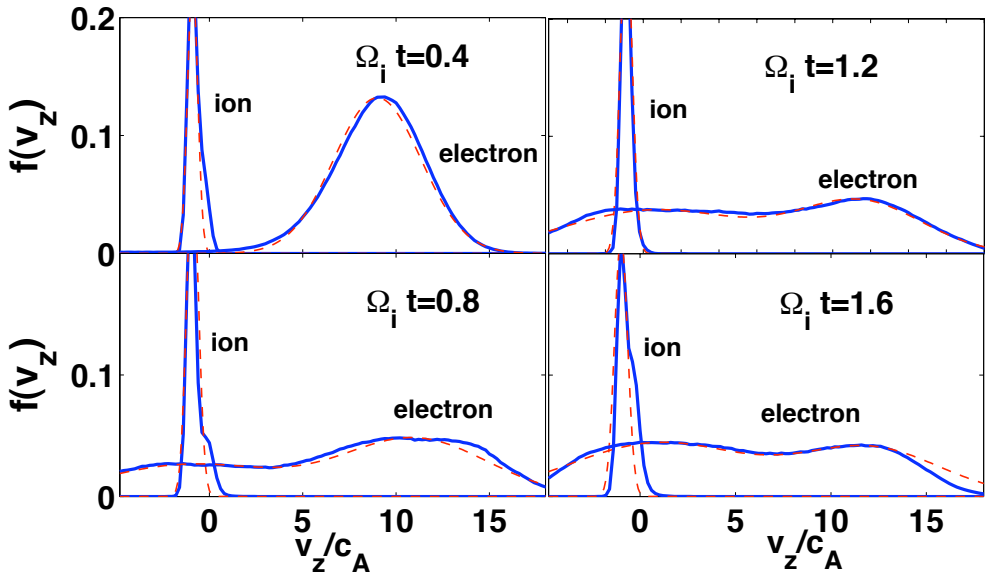

Figure 4.5: Distribution functions $f(v_z)$ of ions and electrons from the PIC simulation at $\Omega_i t = 0.4, 0.8, 1.2, 1.6$ are shown by the blue lines, with the ion distribution function reduced by a factor of 4; the theoretical fitting with double drifting Maxwellians is shown by the dashed red lines.

is less well defined in E_z ((c) and (d) in Fig. 4.4). This mode corresponds to the appearance of long oblique stripes in Fig. 4.3 at late time. The spectra suggest that two modes have developed at late time, which we will examine in further detail.

In the cold plasma limit, the phase velocity of the Buneman instability is $(m_e/(2m_i))^{1/3}|v_{ez}|/2 - v_{di} \sim -0.25c_A$ (Galeev & Sagdeev 1984b). The electrons with velocity around this phase velocity can be trapped. Evidence for trapping can be seen from the change in the electron distribution functions between $\Omega_i t = 0.4$ and 0.8 in Fig. 4.5. The distribution function at $\Omega_i t = 0.8$ has a broad peak centered around the expected Buneman phase speed. Some of the high velocity electrons actually increase their velocity v_z early in the simulation because they are accelerated locally by the induced electric field E_z that maintains the net current in the layer. At time $\Omega_i t = 1.2$ and 1.6, the electrons at higher velocity are dragged

to lower velocity, which can't be explained by the wave-particle interactions with the Buneman instability. In our simulation, the average drift velocity of electrons decreases by a factor of two from the initial value $\sim 10c_A$ to $\sim 5c_A$ at $\Omega_i t = 1.6$.

To understand the late time behavior of the electrons, we investigate the phase speed of E_z by stacking cuts of $E_z(z)$ at time intervals $\Omega_i t = 0.02$. The image shown in Fig. 4.6 (a) traces the motion of the peaks and valleys of the waves. The slopes of the curves formed by the peaks or valleys show the evolution of the phase speed in the z direction. The slopes of these curves increase with time, indicating that the parallel phase speed v_{pz} of the waves increases. The v_{pz} increases from a very small value at $\Omega_i t = 0.4$ when the instability onsets to $6c_A$ at $\Omega_i t = 0.8$, and near $10c_A$ at the end of the simulation. The phase speed of E_x along z behaves similarly to E_z, but is faster at late time (the slopes of E_x are steeper). Thus, we suggest that the increasing phase speed of the turbulence at late time allows the electrons with high velocity to be dragged to lower velocity through wave-particle interactions. The early trapping of electrons by the instability saturates Buneman and allows new instabilities to grow.

An interesting feature of the waves in our simulation is the growth of two distinct classes of modes parallel and nearly-perpendicular to the magnetic field. We explore the nature of the late-time instabilities by investigating the unstable wave spectra with particle distributions that match those measured in the simulations.

We choose double drifting Maxwellians for electrons, and a single drifting Maxwellian for ions. The dispersion relation obtained in equation (4.6) is for waves with $\Omega_i \ll \omega \ll \Omega_e$. Assuming the wavevector $\mathbf{k}$ lies in the plane $x - z$, i.e.

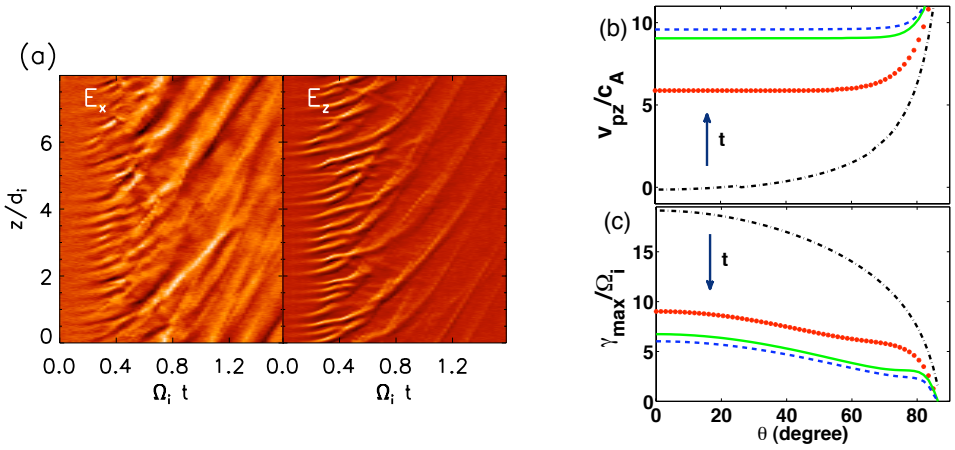

Figure 4.6: In (a) cuts of E_x and E_z versus z and time from the simulation. The slope of the curves is the phase speed v_{pz} in the simulation rest frame. In (b) and (c) solutions of the dispersion relation using the fittings of distribution functions shown in Fig. 4.5 at $\Omega_i t = 0.4, 0.8, 1.2, 1.6$. In (b) is the parallel phase speed versus the angle θ between the wavevector $\mathbf{k}$ and the magnetic field at the four times. In (c) are the corresponding maximum growth rates γ_{max} versus θ.

$\mathbf{k} = (k_x, 0, k_z)$, the dispersion relation takes the form:

$$1 + \frac{2\omega_{pi}^2}{k^2 v_{ti}^2}[1 + \zeta_i Z(\zeta_i)] + \frac{2\delta\omega_{pe}^2}{k^2 v_{te1}^2}[1 + I_0(\lambda)e^{-\lambda}\zeta_{e1} Z(\zeta_{e1})] + \frac{2(1-\delta)\omega_{pe}^2}{k^2 v_{te2}^2}[1 + I_0(\lambda)e^{-\lambda}\zeta_{e2} Z(\zeta_{e2})] = 0,$$

where $\zeta_i = (\omega - k_z v_{di})/k v_{ti}$, $\zeta_{e1} = (\omega - k_z v_{de1})/k_z v_{zte1}$, $\zeta_{e2} = (\omega - k_z v_{de2})/k_z v_{zte2}$, $\lambda = k_x^2 v_{xte}^2/2\Omega_e^2$, δ is the weight of high velocity drifting Maxwellian, Z is the plasma dispersion function and I_0 is the modified Bessel function of the first kind with order zero. The thermal velocity of species j is defined by $v_{tj}^2 = 2T_{tj}/m_j$ and drift speed by v_{dj}, which is parallel to the magnetic field (z direction). The ion temperature is taken to be isotropic.

It should be noted that our simulation is highly non-linear while our model is based on linear theory. This approach is reasonable, however, because we can fit the real time distribution functions from the simulation for input into the dispersion

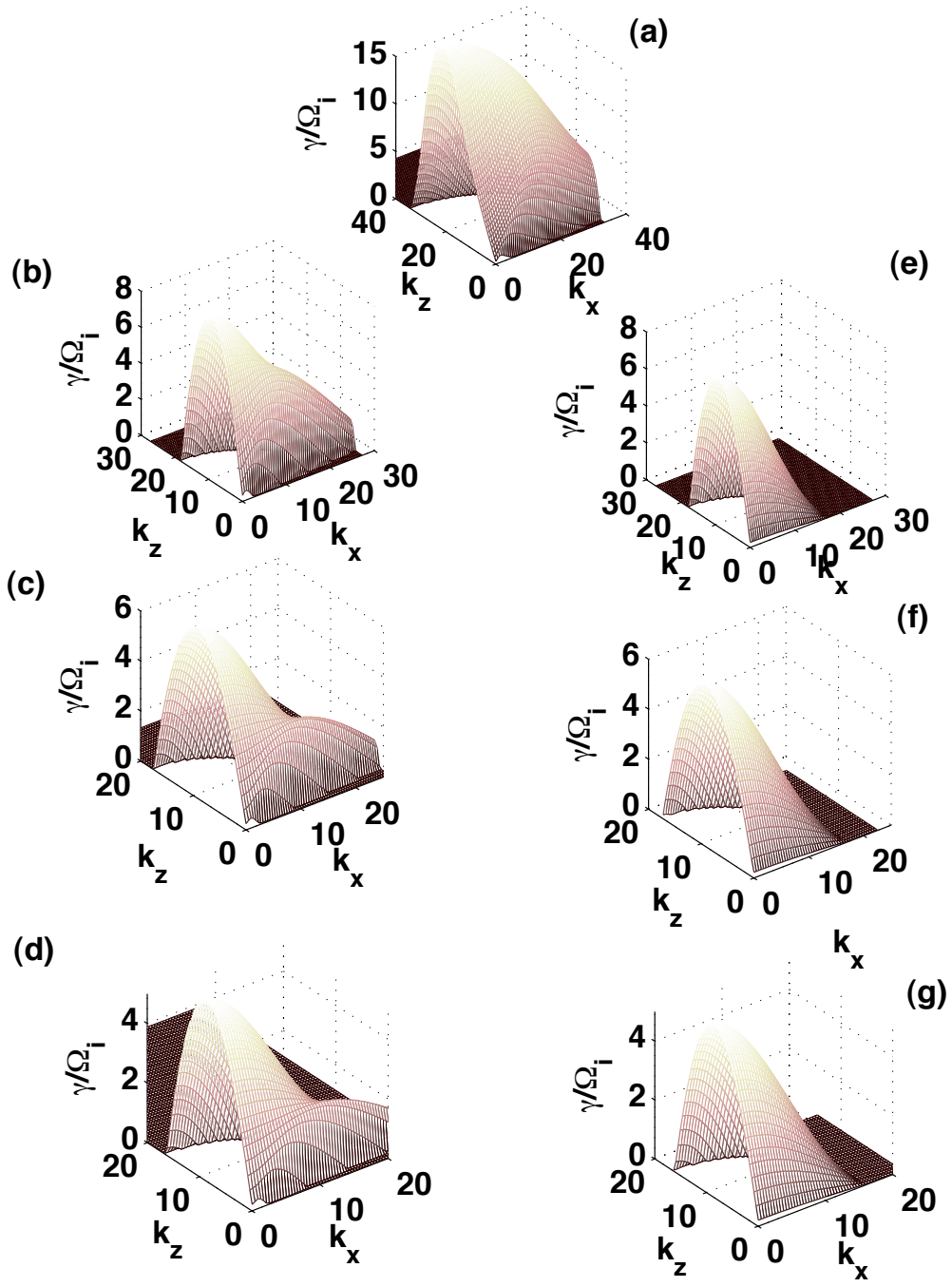

Figure 4.7: The 2D theoretical spectrum from kinetic theory using the fittings of distribution functions of electrons and ions shown in Fig. 4.5. In (a) is the spectrum at $\Omega_i t = 0.4$ when the electron distribution is still a single drifting Maxwellian. In (b), (c) and (d) are the spectra at $\Omega_i t = 0.8, 1.2$ and 1.6 using the fittings of distribution functions of both electrons and ions. In (e), (f) and (g) are the spectra again at $\Omega_i t = 0.8, 1.2, 1.6$ but neglecting the ions.

Table 4.1: Parameters of Model Dist. Funs.

	v_{zte1}	v_{zte2}	v_{de1}	v_{de2}	v_{ti}	v_{di}	δ
$\Omega_i t$=0.4	3.3		9		0.38	-0.9	0
$\Omega_i t$=0.8	5.5	6.6	11	-1	0.45	-0.9	0.6
$\Omega_i t$=1.2	4.6	7	11.5	0.7	0.45	-0.9	0.49
$\Omega_i t$=1.6	5.2	6.6	12.1	1	0.48	-0.9	0.41

relation in Eq. (4.6) to obtain the wave modes. In Fig. 4.5, we show that the real time distribution functions of electrons (blue line) can be very well fit with a double drifting Maxwellian (dashed red line). The parameters of the fittings are listed in Table 4.1. From the table we see the weight of high velocity electrons decreases with time which indicates electrons are dragged from high velocity to low velocity as the system evolves. Solving Eq. (4.6) numerically, we show the growth rate of unstable modes in the (k_x, k_z) plane at $\Omega_i t = 0.4, 0.8, 1.2, 1.6$ in Fig. 4.7 (a,b,c,d).

From Fig. 4.5 (a), we see at $\Omega_i t = 0.4$, around the onset of the Buneman instability, the electron distribution function is well approximated by a single drifting Maxwellian. The unstable modes shown in the spectrum in Fig. 4.7 (a) are characteristic of the Buneman instability. The dominant mode is parallel with $k_z \sim 20$ and with a large growth rate $\gamma \sim 15\Omega_i$. At $\Omega_i t = 0.8$, the low velocity band of the electron distribution rises up, and interestingly, a new mode emerges at $k_x d_i \sim 20$ and $k_z d_i \sim 5$ in the spectrum in Fig. 4.7 (b). The stronger mode is peaked at $k_x d_i \sim 0$ and $k_z d_i \sim 10$. At $\Omega_i t = 1.2$, the electron distribution function in Fig. 4.5 (c) has a

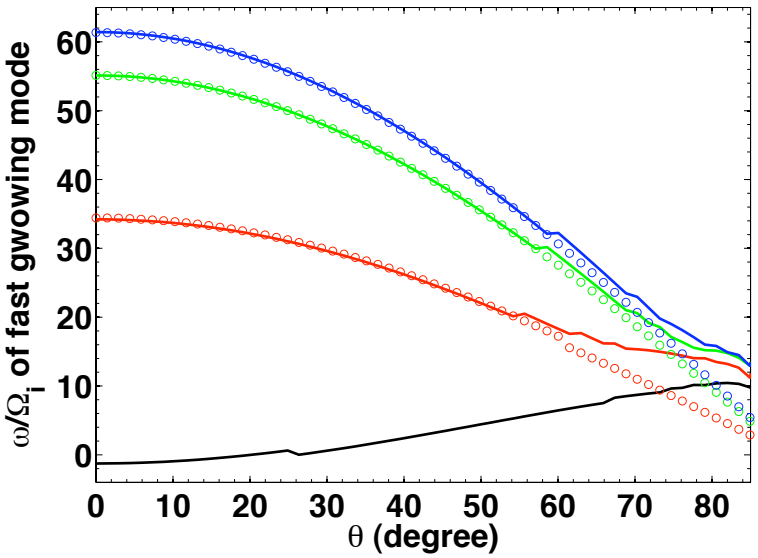

Figure 4.8: The frequency of fast growing mode at time $\Omega_i t = 0.4, 0.8, 1.2, 1.6$ versus the angle θ. The circles are the frequency neglecting the contribution from the ions.

double-peak. Two distinct modes appear in Fig. 4.7 (c). These unstable spectra are consistent with the spectra of E_z and E_x we show in Fig. 4.4. At late time $\Omega_i t = 1.6$, both modes become weaker as shown in Fig. 4.7 (d).

Do these two modes belong to the general class of Buneman instabilities or do they represent the emergence of a new class of instabilities? We have shown that the electrons can be modeled with double drifting Maxwellians suggesting that an electron-electron two-stream instability might develop. To investigate this possibility, we solve the dispersion relation in Eq. (4.6) by removing the contribution from the ions. The unstable modes for the two-stream instability at $\Omega_i t = 0.8, 1.2, 1.6$ are shown in Fig. 4.4 (e), (f) and (g). Indeed, the growth rates of the two-stream instability correspond exactly to the stronger mode shown in Fig. 4.4 (b), (c) and (d), respectively. The corresponding frequency at $\Omega_i t = 0.4, 0.8, 1.2, 1.6$ is shown in Fig. 4.8.

The frequencies of electron-electron two-stream instability at $\Omega_i t = 0.8, 1.2, 1.6$ obtaining by just considering the electrons are shown by circles. The frequencies shown by the solid lines are obtained with including the contributions of all the electrons and ions. The circles are in coincidence with the solid lines at small θ and diverge from the solid lines at larger θ. The frequency of the two-stream mode increases with time and is about $0.35\omega_{pe}$ in the ion rest frame at $\Omega_i t = 1.6$.

The weaker mode is not present in Fig. 4.4 (e), (f) and (g) and must involve the ions. Its wavevector is nearly perpendicular to the direction of the magnetic field. The corresponding frequency for this mode can be obtained from the solid line at large θ in Fig. 4.8. All the solid lines reach a similar frequency around $\sim 16\Omega_i$ with $\theta \sim 90^0$, which is close to the lower-hybrid frequency in the cold plasma limit, $\omega_{lh} = \omega_{pi}/(1 + \omega_{pe}^2/\Omega_e^2)^{1/2} + k_z v_{di} \sim 15\Omega_i$. We thus conclude that the weaker mode is in fact a current driven lower hybrid instability, which was discussed earlier by McMillan and Cairns (McMillan & Cairns 2006, 2007). The Buneman instability in our simulation has evolved into a dual state of electron two-stream and lower hybrid instabilities. The stripes appearing at late time are caused by the lower hybrid instability. The angle between the strips of the E_x and magnetic field is determined by the group velocity $90^0 - atan(\frac{Re(v_{gx})}{Re(v_{gz})}) \sim 80^0$.

The drag on high velocity electrons requires wave-particle interactions with waves of high phase speed. We show the phase speed of electrostatic waves in Fig. 4.6 (b) using the dispersion relation in Eq. (4.6) and the model distribution function functions shown by the red-dashed line in Fig. 4.5. At a given angle θ between the wavevector $\mathbf{k}$ and magnetic field $\mathbf{B}$, the maximum growth rate is calculated with

respect to the magnitude of k and is shown in Fig. 4.6 (c). The resulting parallel phase speed v_{pz} versus θ is shown in Fig. 4.6 (b). The four lines are the phase speed calculated at times $\Omega_i t = 0.4, 0.8, 1.2, 1.6$ (black dash-dotted, red dotted, green solid and blue dashed, respectively). The phase speed increases with time, especially at small values of θ, transitioning from the Buneman to the electron two-stream instability. The phase speeds at small θ are around $0, 6, 9$ and $10c_A$, consistent with the simulation data in Fig. 4.6 (a). The phase speeds at large θ are much larger than at small θ even at $\Omega_i t = 0.4$, but as shown in Fig. 4.6 (c) the corresponding maximum growth rate at this early time is small compared with the Buneman instability. The growth rates at large angle become comparable to the rates at small angle at late time, which is consistent with the development of transverse modes in the simulations at late time.

4.2.2 Electron-electron Two-Stream Instability and the Coherent Formation of Electron Holes

The electron-electron two-stream instability takes over from the Buneman instability at late time and continuously sustains the formation of electron holes. The increasing parallel phase speed enables the wave to resonate with electrons at high velocity. The simulations show that the electron holes moving faster overtake the slower electron holes, which then causes the electron holes to break up.

Fig. 4.9 shows the evolution of the electron holes in the midplane of the current sheet ($x - z$ plane). At $\Omega_i t = 0.4$, the perturbed electric field E_z propagates parallel

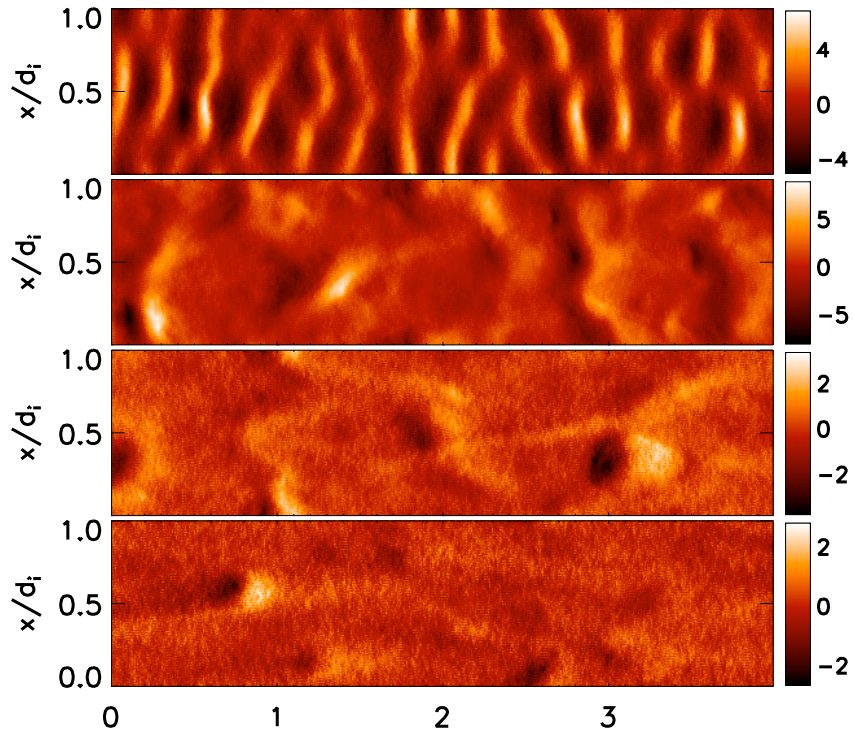

Figure 4.9: The spatial structures of the electric field E_z in the midplane of the current sheet ($x-z$ plane) at times $\Omega_i t = 0.4, 0.8, 1.2, 1.6$ from the top of the panel to the bottom, respectively.

to the magnetic field, and forms many strong intense localized structures. At $\Omega_i t = 0.8$, these localized structures have coalesced. At $\Omega_i t = 1.6$, most of the electron holes have disappeared. The extended structures of the electric field E_z at $\Omega_i t = 0.4$ have a lifetime of around $0.06\Omega_i^{-1}$ while the round holes at $\Omega_i t = 0.8$ remain for $0.3\Omega_i^{-1}$. The bounce time $\tau_b = 1/\omega_b = \sqrt{\frac{m_e}{2ek_z^2|\phi|}}$ where ω_b is the bounce frequency and $|\phi|$ is the amplitude of the electric potential. At $\Omega_i t = 0.4$, $E_z \sim k_z\phi \sim 4c_A B_0/c$ and $k_z \sim 20/d_i$. Thus $\tau_b \sim 0.01\Omega_i^{-1}$ while the life time of the holes is $0.06\Omega_i^{-1}$ and the lifetime is of the same order. Thus the electron holes are not very stable though the electric field is strong. At $\Omega_i t = 0.8$, $E_z \sim 5c_A B_0/c$ and $k_z \sim 10/d_i$. Thus $\tau_b \sim 0.01\Omega_i^{-1}$, compared to the life time of the holes of $0.3\Omega_i^{-1}$. The electron holes are very stable and can be represented by the Bernstein-Greene-Kruskul (BGK) solutions (Bernstein et al. 1957).

The BGK electron holes are self-sustained electrostatic structures. The growing electric field traps the electrons resonating with the waves. They satisfy the 1D stationary Vlasov equation:

$$v\frac{\partial f}{\partial x} + \frac{e}{m_e}\frac{\partial \phi}{\partial x}\frac{\partial f}{\partial v} = 0, \tag{4.14}$$

where ϕ is the electrostatic potential, and f is the electron distribution.

The BGK equation is written in the rest wave frame in which the velocity of an electron hole v_h, the group velocity v_g and phase velocity v_p of the wave packet are equal, i.e $v_h = v_g = v_p$. v_h is defined as:

$$v_h = \int_{-\infty}^{\infty} dvdxvf(v,x). \tag{4.15}$$

v_h is the average movement of the the trapped electrons. These trapped electrons

co-move with the electrostatic wave packet, thus v_h equal v_g, however, v_g does not equal v_p since in general electron holes are not BGK modes and dispersive.

The difference between the phase velocity v_{pk} and group velocity v_{gk} of the waves produces a key condition on the existence of electron holes. An electron trapped by an electrostatic wave with (ω, k) propagating with v_{pk} in a wave packet satisfies

$$\frac{m_e}{2}(v - v_{pk})^2 - e|\phi_k| \leq 0, \tag{4.16}$$

and therefore

$$v \leq v_{pk} \pm \sqrt{\frac{2e|\phi_k|}{m_e}}, \tag{4.17}$$

where $|\phi_k|$ is the amplitude of the electric potential. The time τ_b required for an electron to be trapped is given by $\tau_b = 2\pi/\omega_b$ with $\omega_b = k_b\sqrt{\frac{2e|\phi_k|}{m_e}}$ where k_b is the wave number of the electron hole. In order for trapping to occur, and therefore for the electron hole to form, the trapping must take place before the difference between the group and phase velocities causes the wave amplitude at the particle position to become small, that is $|v_{gk} - v_{pk}|\tau_b < 2\pi/k_b$.

Therefore we obtain

$$|v_g - v_p| \leq \sqrt{\frac{2e|\phi|}{m_e}} = w_b/k_b, \tag{4.18}$$

where the subscript k is dropped.

Both equation (4.17) and (4.18) are the required conditions for the formation of stable electron holes. It means that the phase speed should be close to the group velocity or the electric field can't effectively trap the particles and fails to form an electron hole. $v_g \sim v_p$ is the coherent condition for the formation of BGK holes.

We have seen that the electron holes continue to form through the entire duration of our simulations. The parallel electron-electron two-stream instability dominates the Buneman instability at late time and sustains the electron holes. The phase speed of the two-stream instability is much larger than the Buneman instability which indicates that inverse Landau-damping occurs at high velocity. How does the increase of phase speed affect the trapping of electrons and the formation of electron holes?

Fig. 4.10 shows the theoretical parallel group velocity v_{gz} and parallel phase speed v_{pz} of the fast growing mode versus the angle θ between the wave vector and the magnetic field at times $\Omega_i t = 0.4, 0.8, 1.2, 1.6$, denoted by black dash-dotted, red dotted, green solid and blue dashed lines. Similar to the parallel phase speed v_{pz}, the group velocity v_{gz} increases in a similar pace. The parallel group velocity is $2c_A$ at $\Omega_i t = 0.4$ and is about $5.5c_A$ at $\Omega_i t = 0.8$ The group velocity is consistent with the velocities of the electron holes in our simulations.

The formation of electron holes requires $|v_{pz} - v_{gz}| \leq \sqrt{\frac{2e|\phi|}{m_e}}$ (equation (4.18)) where $|\phi| \sim E_z/k_z$. At $\Omega_i t = 0.4$, from Fig. 4.9, the upper limit of the formation condition is $\sqrt{\frac{2e|\phi|}{m_e}} = 6c_A$ and from Fig. 4.10 $|v_{pz} - v_{gz}| \sim 2c_A$ so the ratio of $\sqrt{\frac{2e|\phi|}{m_e}}$ and $v_{pz} - v_{gz}$ is 0.3, which satisfies the formation condition for electron holes. At $\Omega_i t = 0.8$, the upper limit of the formation condition is $\sqrt{\frac{2e|\phi|}{m_e}} = 10c_A$ and $|v_{pz} - v_{gz}| \sim 1c_A$ so the corresponding ratio is 0.1. At $\Omega_i t = 1.2$, the upper limit of the formation condition $\sqrt{\frac{2e|\phi|}{m_e}} = 6c_A$ and $|v_p - v_g| \sim 1c_A$ so the corresponding ratio is around 0.16. At $\Omega_i t = 1.6$, the formation condition $\sqrt{\frac{2e|\phi|}{m_e}} = 5c_A$ and $|v_{pz} - v_{gz}| \sim 1c_A$ so the corresponding ratio is 0.2. The formation condition for the

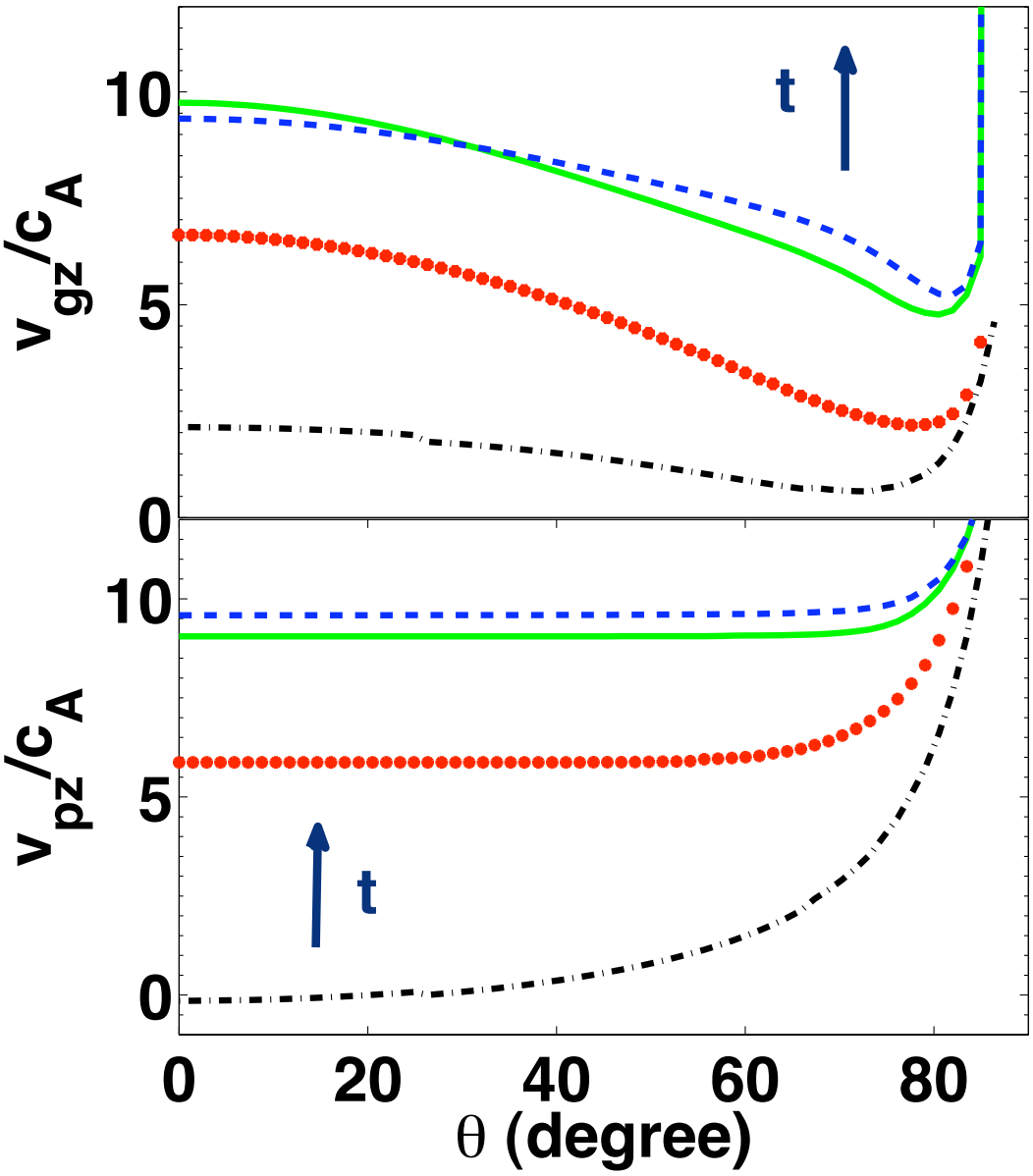

Figure 4.10: The group velocity and phase velocity of the fast growing mode versus the angle θ at time $\Omega_i t = 0.4, 0.8, 1.2, 1.6$ denoted by black dash-dotted, red dotted, green solid and blue dashed line, respectively.

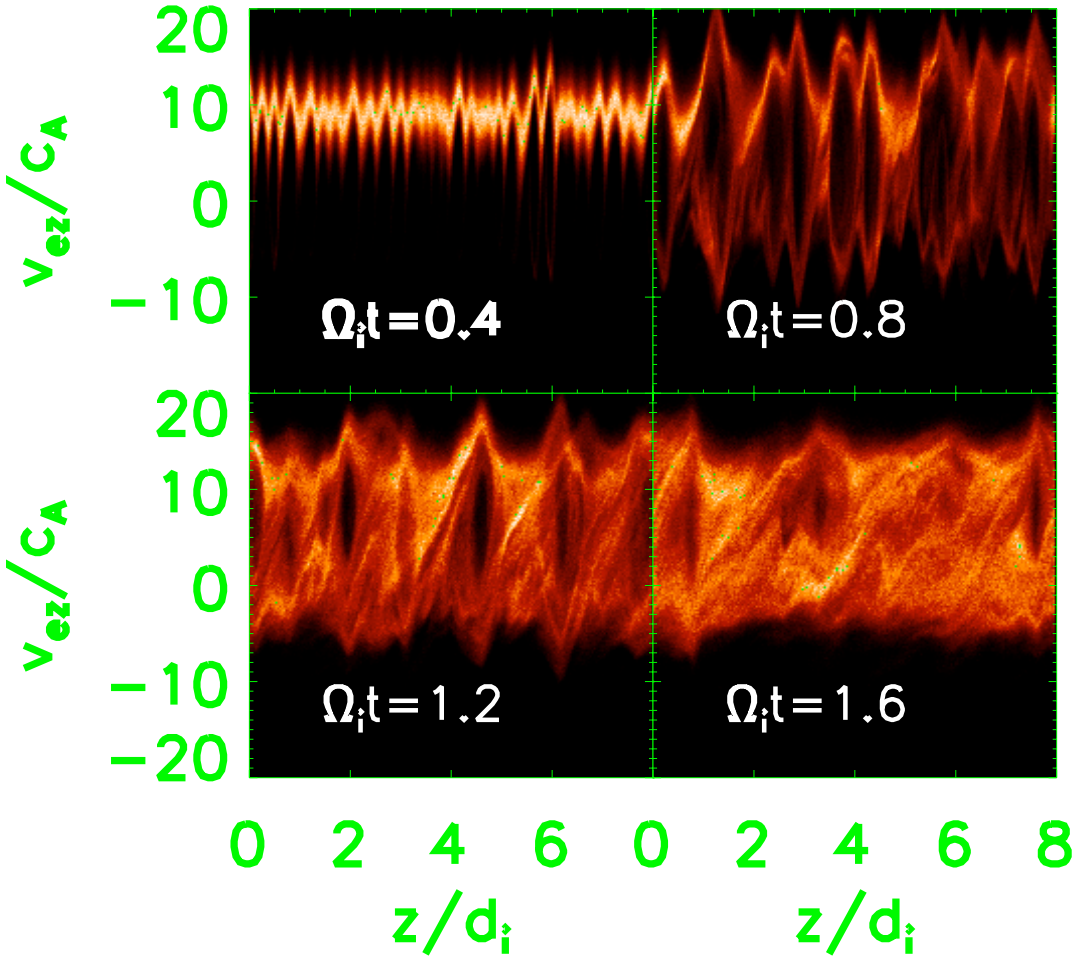

Figure 4.11: Electron distributions $f_e(\mathbf{x}, \mathbf{v})$ in phase space (z, v_{ez}) at time $\Omega_i t = 0.4, 0.8, 1.2, 1.6$

.

electron holes are satisfied at all times and v_{pz} is close to v_{gz}. Thus the electron holes at late time are good approximations of the BGK model.

Fig. 4.11 shows the electron distribution function in the phase space $z - v_{ez}$ at $\Omega_i t = 0.4, 0.8, 1.21.6$. Electrons circulate in the phase space. At the midpoint of the position of the holes, the potential is a minimum and the relative velocity of the trapped electrons and the holes reaches a maximum. At the maximum position of the holes, the relative velocity of the trapped electrons reaches a minimum. Thus

the trajectories of the trapped electrons in phase space are closed. If the potential well is not strong enough to trap the electrons, the electron trajectory in the phase space can't close. At $\Omega_i t = 0.4$, trapping of electrons is not evident. At $\Omega_i t = 0.8$, trapping of the electrons is evident since the particle number is nearly constant on the constant energy surface ($\frac{m_e}{2}(v - v_{pz})^2 - e\phi = constant$). At $\Omega_i t = 1.2$, though holes with similar width still exist, the electron's movement has become more diffuse. At $\Omega_i t = 1.6$, the electron holes form a wider diffusion layer. The diffusion of the electrons is likely caused by the lower hybrid instability interaction with the high velocity electrons at a similar phase speed. The contribution of the lower hybrid instability is weak and its contribution to the parallel electric field $E_z = cot(\theta)E_x \sim 0.1E_x$. The resulting condition for the trapping of the electrons is $|v_p - v_g| < 2c_A$, but the difference between the phase velocity and group velocity is about $5c_A$ at late time (see Fig. 4.10). Thus the lower hybrid instability is not strong enough to trap electron. Though the frequency of the lower hybrid instability is much lower than the frequency of the electron two-stream instability and its action on the electrons is weak, the interaction of these instabilities causes the trajectories of the trapped electrons to be stochastic (Sagdeev et al. 1988).

The width of the electron holes in phase space is consistent with the wavelength of the instability. At $\Omega_i t = 0.4$, $k_z \sim 20/d_i$, its corresponding wavelength is $0.3d_i$ which is close to the width of holes in Fig 4.11. At time $\Omega_i t = 0.8$, the width of the holes increases by a factor of two while the wave number of the instability decrease to $k_z = 10/d_i$. Its corresponding wavelength is $0.3d_i$ which is again close to the width of holes in Fig 4.11.

Our simulations show that the condition $v_{pz} - v_{gz} < \omega_b/k_z$ is the important condition for the formation of the electron holes. The group velocity coherently increases with the phase velocity of the waves so that the electron holes are sustained. The system can self-regulate the physical process of wave-particle interactions.

4.3 Nonlinear Development of Streaming Instabilities in Low β Plasma with $\omega_{pe}/\Omega_e > 1$

In space magnetized plasmas are often in the regime $\omega_{pe}/\Omega_e > 1$. The development of streaming instabilities in this limit is therefore important. The cold plasma limit of the growth rate for the Buneman instability is proportional to $(\frac{m_e}{m_i})^{\frac{1}{3}}\omega_{pe}$ and for the electron-electron two-stream instability is proportional to ω_{pe}. Thus in a magnetized plasma with $\omega_{pe}/\Omega_e > 1$, both instabilities develop and saturate on a very short time scale. In this case does the growth rate of electron-electron two stream instability suppress the Buneman instability at late time as in the case with $\omega_{pe}/\Omega_e > 1$ or does something new occur? Would the lower hybrid instability become weaker or stronger? What roles do the instabilities play in the electron and ion heating? These problems are poorly understood.

We carry out new simulations to investigate these problems. The initial set up of the new simulation is similar to the simulations in the case of $\omega_{pe}/\Omega_e < 1$ except the light speed is increased to $c = 80c_A$ and the plasma frequency is increased to $\omega_{pe} = 800\Omega_i$ compared to the earlier case where $c = 20c_A$ and $\omega_{pe} = 200\Omega_i$. The magnetic field configurations in these two cases are the same.

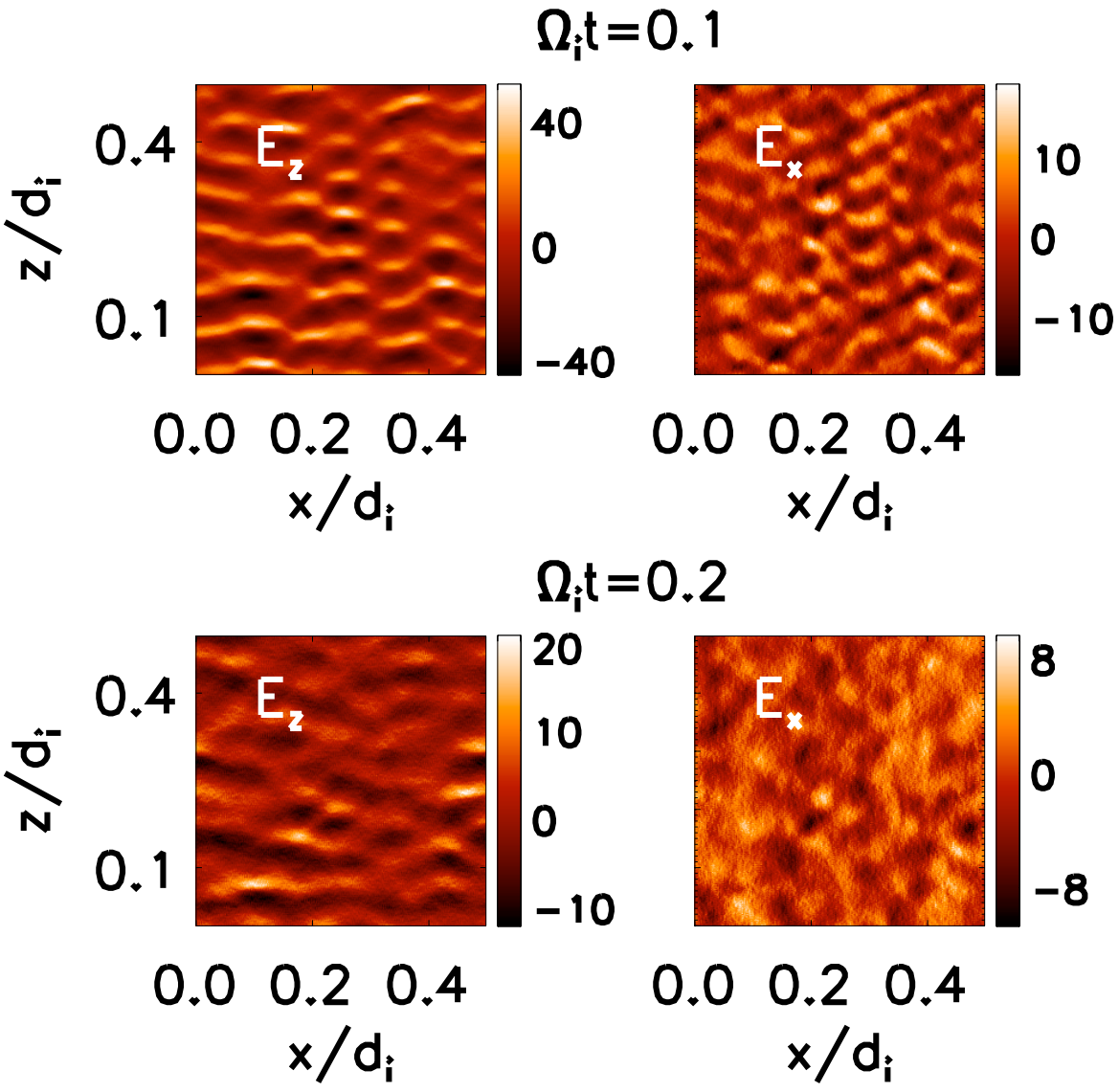

Figure 4.12: Spatial structures of E_z and E_x in the midplane of the current sheet ($x-z$ plane) at time $\Omega_i t = 0.1, 0.2$.

The evolution time scale of instabilities in this case is about 10 times shorter than that in the case $\omega_{pe}/\Omega_e < 1$. At time $\Omega_i t = 0.05$, bipolar electric field E_z structures have developed and propagate along the magnetic field. At time $\Omega_i t = 0.1$, some new features appear while parallel thin bipolar structures still dominate the spatial structures of E_z and E_x (Fig 4.12). Some localized parts of the bipolar fields grow intense and extend in z. In the image of E_x, the waves become oblique. At time $\Omega_i t = 0.2$, the localized bipolar structures remain. The E_x waves become almost perpendicular to the magnetic field and the structures mix. The extended strips seen in earlier simulations are absent.

Fig. 4.13 shows the power spectra of E_x and E_z in the midplane of the current sheet $(x - z)$. At time $\Omega_i t = 0.05$, both E_x^k and E_z^k show a parallel mode with $k_z d_i \sim 100$ which corresponds to the bipolar structures seen in Fig. 4.12. At $\Omega_i t = 0.1$, in Fig. (c) & (d), E_x^k reveals a new strong mode with $(k_x d_i, k_z d_i) \sim (35, 12)$ with $(\delta k_x d_i, \delta k_z d_i) \sim (10, 5)$. The mode is most clean in the spectrum of E_z^k. A new weak mode appears near $(k_x d_i, k_z d_i) \sim (0, 25)$ in the E_z spectrum; At $\Omega_i t = 0.2$, in Fig. (e) & (f), both spectra almost spread over the whole range of k_z.

While the spatial structures mix, the electron distributions look clean. At $\Omega_i t = 0.05$, the electron distribution function remains Maxwellian. At $\Omega_i t = 0.1$, a long tail appears on the negative velocity side of the electron distribution function. At $\Omega_i t = 0.2$, more high energetic electrons move down to the lower band and the long tail rises up and extends to high velocity, around $10 c_A$.

We again analyze the simulations using the double Maxwellian model to determine which instability dominates as the system develops in time. We use the

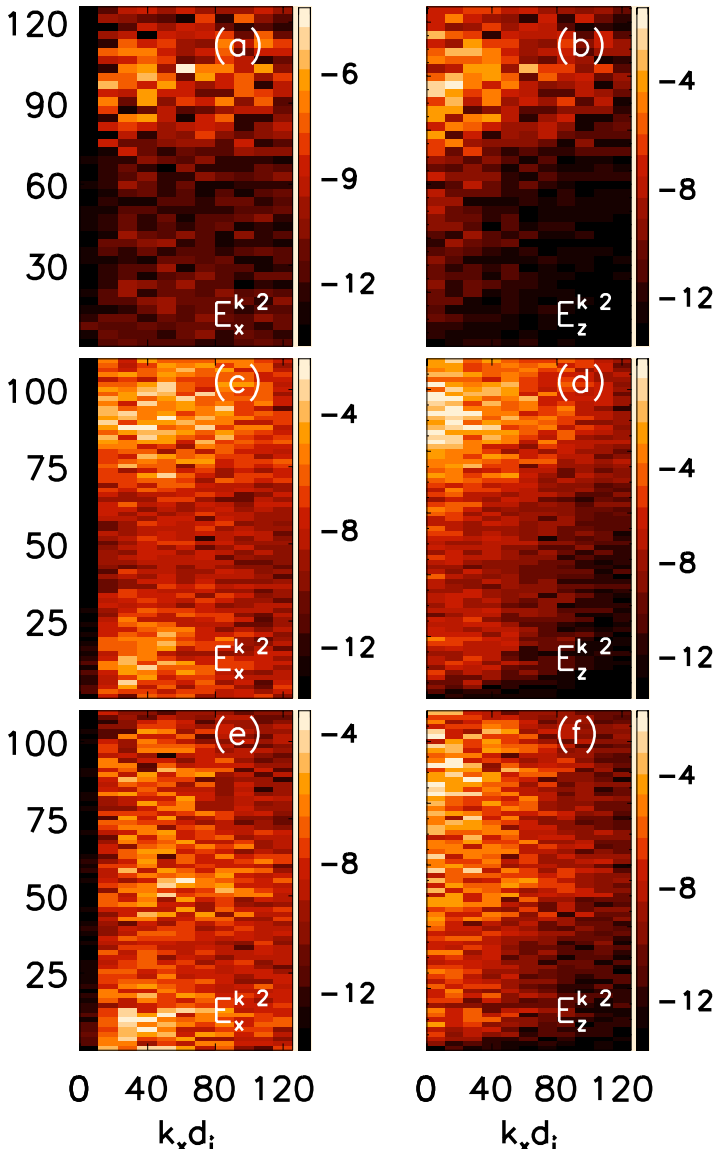

Figure 4.13: Power spectra $|E_x(k_x, k_z)|$ and $|E_z(k_x, k_z)|$ of E_x and E_z spatial structures in the midplane of the current sheet $(x - z)$ at time $\Omega_i t = 0.05, 0.1, 0.2$, from the top to the bottom of the panel, respectively.

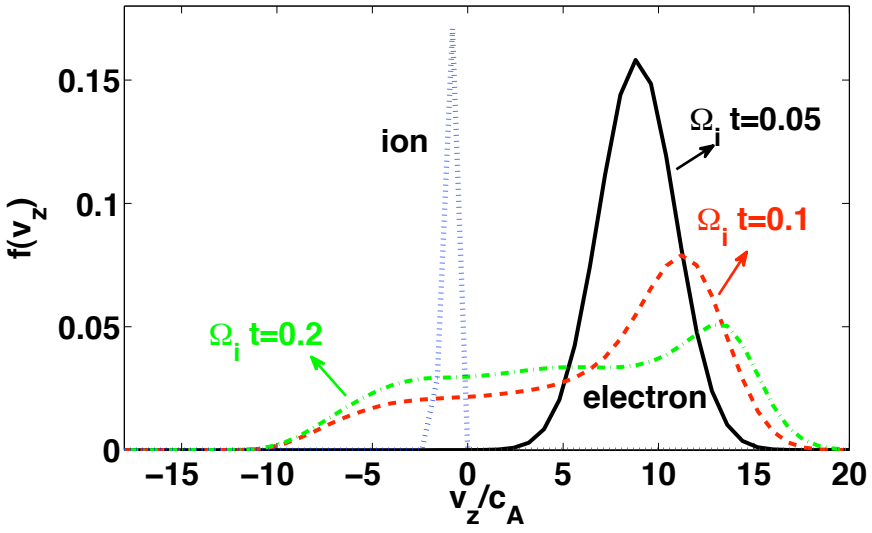

Figure 4.14: Electron and ion distribution functions. Blue Dotted line denotes the ion distribution function. Black solid line, red dashed line and green dash-dotted line denote the electron distribution functions at times $\Omega_i t = 0.05, 0.1, 0.2$, respectively.

dispersion function obtained in equation (4.6) which is applicable for waves with $\Omega_i \ll \omega \ll \Omega_e$:

$$1 + \frac{2\omega_{pi}^2}{k^2 v_{ti}^2}[1 + \zeta_i Z(\zeta_i)] + \frac{2(1-\delta)\omega_{pe}^2}{k^2 v_{te1}^2}[1 + I_0(\lambda)e^{-\lambda}\zeta_{e1}Z(\zeta_{e1})] + \frac{2\delta\omega_{pe}^2}{k^2 v_{te2}^2}[1 + I_0(\lambda)e^{-\lambda}\zeta_{e2}Z(\zeta_{e2})] = 0,$$

where $\zeta_i = (\omega - k_z v_{di})/kv_{ti}$, $\zeta_{e1} = (\omega - k_z v_{de1})/k_z v_{zte1}$,$\zeta_{e2} = (\omega - k_z v_{de2})/k_z v_{zte2}$, $\lambda = k_x^2 v_{xte}^2/2\Omega_e^2$, δ is the weight of low velocity drifting Maxwellian, Z is the plasma dispersion function and I_0 is the modified Bessel function of the first kind with order zero. The thermal velocity of species j is defined by $v_{tj}^2 = 2T_{tj}/m_j$ and the drift speed by v_{dj}, which is parallel to the magnetic field (z direction).

The model parameters are shown in table (4.2). The weight of the low velocity drifting Maxwellian δ increases quickly with time, which means that electrons are dragged to low velocity from high velocity. The thermal velocity of the low velocity

Table 4.2: Parameters of Model Dist. Funs.

	v_{zte1}	v_{zte2}	v_{de1}	v_{de2}	v_{ti}	v_{di}	δ
$\Omega_i t$=0.05	2.8		9		0.5	-0.8	0
$\Omega_i t$=0.1	3.5	9.3	11.2	1.25	0.5	-0.8	0.47
$\Omega_i t$=0.2	3.3	10.5	13.4	4.1	0.5	-0.8	0.76

drifting Maxwellian sharply rises. The thermal velocity of the high velocity electron drifting Maxwellian increases but remains quite small. This indicates that only a small amount of kinetic energy is converted into thermal energy of high velocity electrons.

Fig. 4.15 shows the unstable modes at times $\Omega_i t = 0.05, 0.1, 0.2$ obtained from the double drifting Maxwellian model in (k_x, k_z) space. Fig. 4.15 (a) is the growth rate at $\Omega_i t = 0.05$ using both electrons and ions when the electron distribution is a single Maxwellian. One dominant mode appears at $(k_x d_i, k_z d_i) \sim (0, 90)$ with width $(\delta k_x d_i, \delta k_z d_i) \sim (50, 30)$, which is close to the wavelength obtained from the cold plasma limit of the Buneman instability $k \sim \omega_{pe}/v_{de} \sim 80/d_i$. However, this mode is not the classical Buneman instability because its maximum growth rate $\gamma_{max}/\Omega_i \sim 80$ is much larger than the wave frequency $\omega_{fg}/\Omega_i \sim 10$ (frequency is shown in Fig. 4.16). The frequency of fastest growing mode ω_{fg} is much bigger than the classical limit $Re(\omega) = \frac{\omega_{pe}}{2}(m_e/2m_i)^{1/3} + k_z v_{di} \sim -40\Omega_i$ (the Doppler effect is large, because of the ion drift $v_{di} = -0.8c_A$). The Buneman instability saturates in a very short time scale $1/\gamma_{max} \sim 0.01\Omega_i^{-1}$.

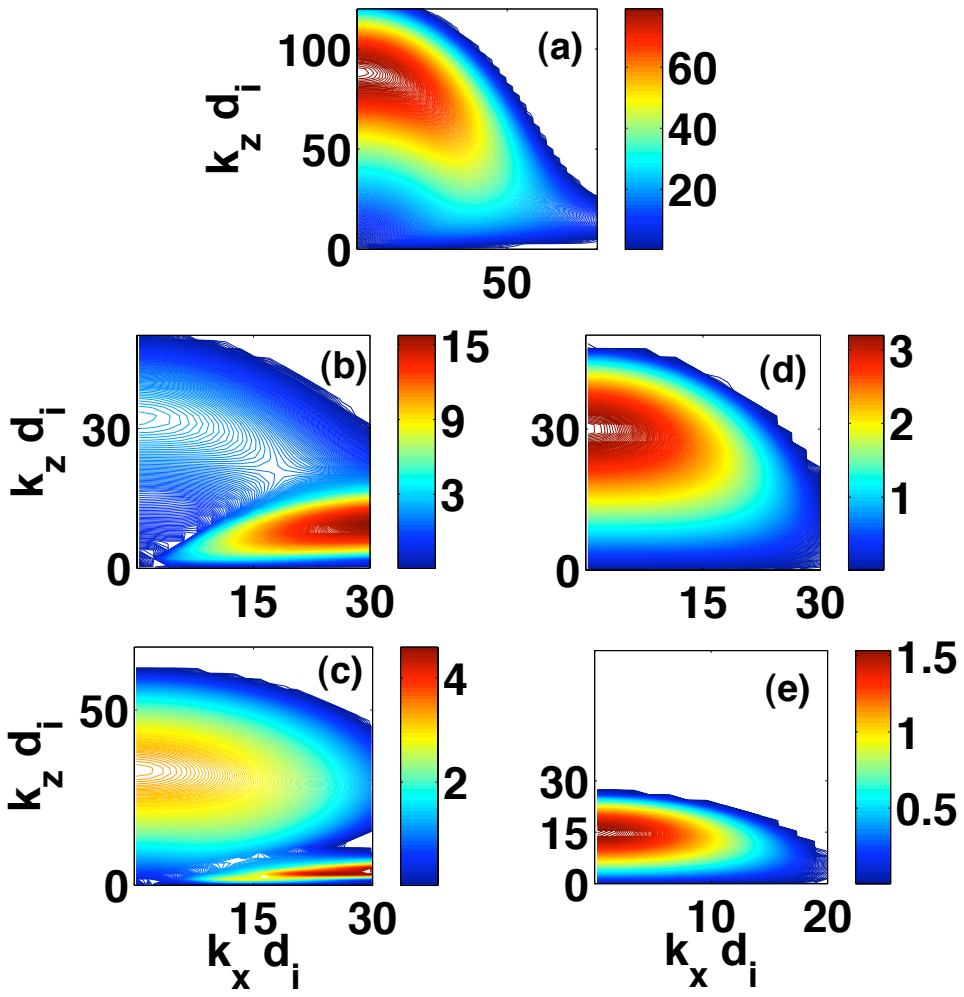

Figure 4.15: The 2D theoretical growth rates of unstable modes obtained by the double drifting Maxwellian model in (k_x, k_z) space. In (a), the spectrum at time $\Omega_i t = 0.05$ when the electron distribution function is a single Maxwellian; in (b) & (c), the spectra at $\Omega_i t = 0.1$ & 0.2 using both the electron and ion distribution functions; and in (d) & (e), the spectra at $\Omega_i t = 0.1$ & 0.2, but neglecting ions.

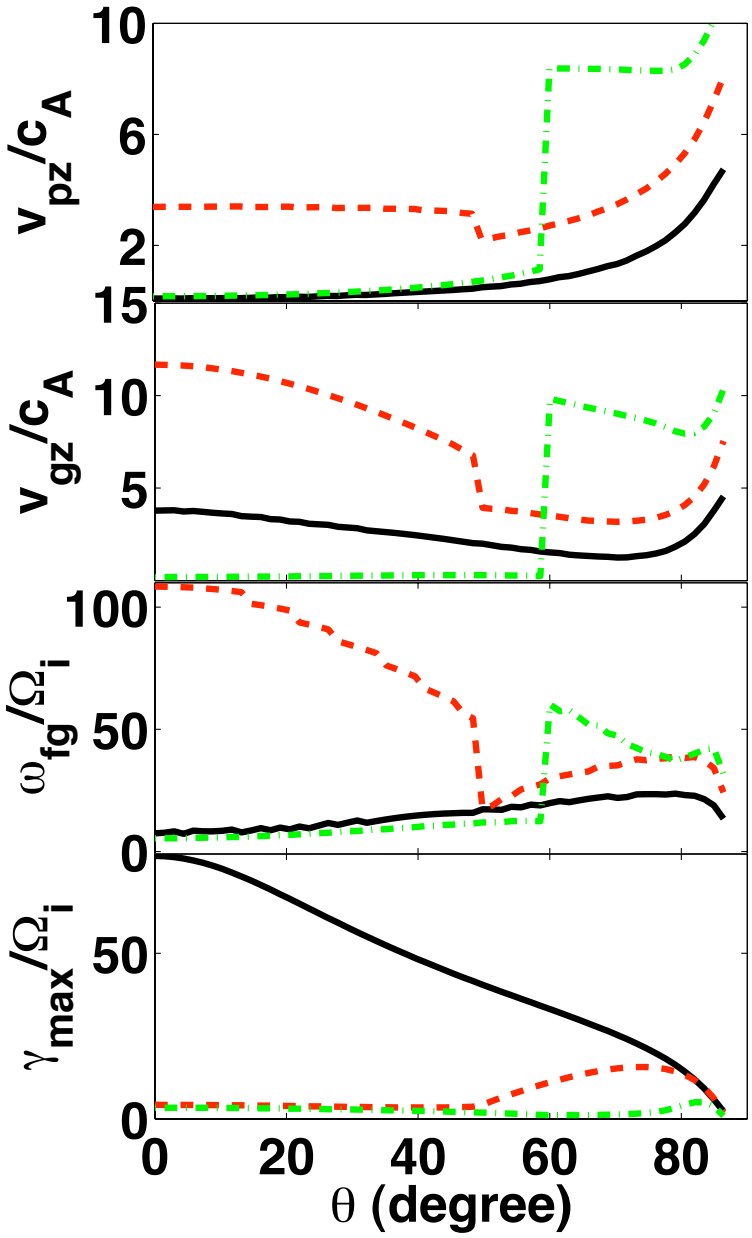

Figure 4.16: Theoretical phase velocity v_{pz}, group velocity v_{gz}, frequency ω_{fg} and maximum growth rate γ_{max} of fast growing mode versus angle θ between the wave vector and magnetic field. Black solid line, red dashed line and green dash-dotted line denote the moments at $\Omega_i t = 0.05, 0.1, 0.2$, respectively.

At $\Omega_i t = 0.1$, two modes appear in Fig. 4.15 (b). The weak one is a parallel mode, centered at $(k_x d_i, k_z d_i) \sim (0, 32)$ with $(\delta k_x d_i, \delta k_z d_i) \sim (15, 20)$ and the strong one is nearly-perpendicular, centered at $(k_x d_i, k_z d_i) \sim (30, 10)$. The maximum growth rate of the nearly-perpendicular mode is 5 times larger than the weak mode. To investigate if this parallel mode is electron-electron two-stream instability, we calculate the spectrum again without using ions. The result is shown in Fig. 4.15 (d). We see the spectrum of the two-stream instability can reproduce the spectrum of the parallel instability. Thus we conclude that the electron-electron two-stream instability overtakes the Buneman instability at $\Omega_i t = 0.1$, although its growth rate is 20 times smaller than the Buneman instability at earlier time. The two-stream instability is also a fully kinetic mode rather than a mode that can be described by a fluid model. What is the strong oblique mode? This mode involves both electrons and ions. Its frequency is about $40\Omega_i$ as shown in Fig. 4.16 by the red-dashed line at $\theta \sim 80^0$, which is around the frequency of the lower hybrid wave obtained in the cold plasma limit $\omega_{lh} = \omega_{pi}/(1 + \omega_{pe}^2/\Omega_e^2)^{1/2} + k_z v_{di} \sim 34\Omega_i$.

At $\Omega_i t = 0.2$, there are two modes in Fig. 4.15 (c). These two modes are of comparable strength and are centered at similar places in (k_x, k_z) space as the modes at $\Omega_i t = 0.1$. Are these two modes the same as before? The spectrum using only electrons is shown in (e). It is obvious that the spectrum of the electron two-stream instability is different from the parallel mode in (c) which produces a peak at $k_z d_i \sim 15$, half of the k_z in (c). The phase speed and frequency of the parallel mode shown by the green dash-dotted line in Fig. 4.16 decreases to the values they had at $\Omega_i t = 0.05$. This data implies that the parallel mode is again the Buneman

instability. This new Buneman instability is a fully kinetic result and far from the Buneman instability at $\Omega_i t = 0.05$ which has $k_z d_i \sim 80$. The nearly-perpendicular mode can be evaluated from the frequency shown by the green dash-dotted line in Fig. 4.16. Similar to the red dashed line, the green dash-dotted line also decreases to $40\Omega_i$ at $\theta \sim 80^0$. Thus the nearly-perpendicular mode is still the lower hybrid instability.

Until now we have had no difficulties in understanding the spectra extracted from the simulations. The Buneman instability, with $k_z d_i \sim 90$ occurs at $\Omega_i t = 0.05$, is subsequently taken over by the electron two-stream instability and finally a new Buneman instability with $k_z d_i \sim 30$ arises. The spatial structure produced by the electron two-stream is weak and transient, leaving fewer hints as to its structure. The lower hybrid instability produce the strips almost parallel to the magnetic field which is indicated by the mode with $(k_x d_i, k_z d_i) \sim (35, 12)$ in Fig. 4.15. At $\Omega_i t = 0.2$, the new Buneman instability contributes to the new parallel mode with $(k_x d_i, k_z d_i) \sim (0, 50)$ appearing in Fig. 4.15 (f). These successive instabilities occur within a time scale $0.2\Omega_i^{-1}$. One rises before another one dies out, and thus the spectra evolves rapidly.

However, a question that needs to be answered is what feeds the Buneman instability and causes it to replace the two-stream instability and keep growing at late time? The phase speed of the Buneman instability is near zero and it should decay after saturation if there were no source of free energy. This question is related to the process of wave-particle interactions and the resulting momentum transport.

Fig. 4.16 shows the phase velocity v_{pz}, group velocity v_{gz}, frequency ω_{fg} and

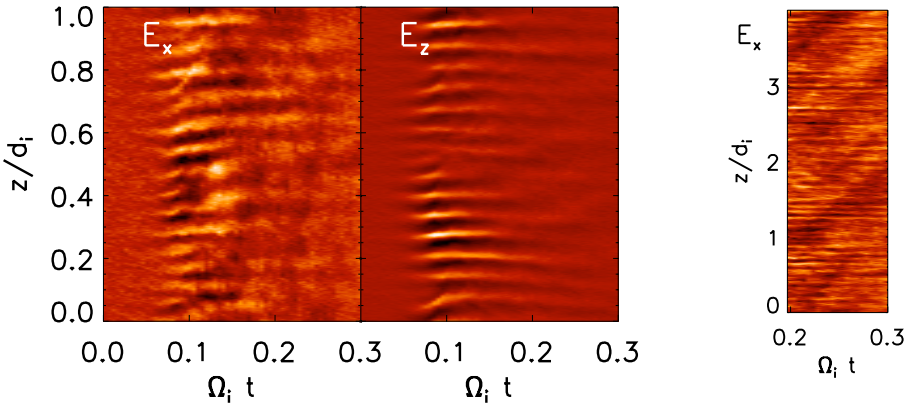

Figure 4.17: Parallel phase speed v_{pz} obtained from the simulation by stacking the cuts of E_x and E_z along z at different times. The slope of the curves is the phase speed. The image at left is for the time interval $0.3\Omega_i^{-1}$ and z from $0-1$. The image at the right is the phase speed v_{pz} shown by E_x during the time interval from $0.2-0.3\Omega_i^{-1}$ and z from $0-4$.

maximum growth rate γ_{max} of the fast growing mode versus the angle θ between the wave vector and magnetic field. The black solid line, red dashed line and green dash-dotted line denote the times $\Omega_i t = 0.05, 0.1, 0.2$. We see that the phase speed of the parallel mode is about zero at $\Omega_i t = 0.05$ when the Buneman instability dominates. Then the phase speed v_{pz} jumps to about $3c_A$ when the electron two-stream instability takes over from the Buneman instability at $\Omega_i t = 0.1$. Finally the Buneman instability replaces the two-stream instability and the phase speed v_{pz} drops to zero again. The changing of the phase speed is consistent with what we obtained from the simulations shown in Fig. 4.17, which is obtained by stacking the cuts of $E_z(x,z)$ and $E_x(x,z)$ along the z direction in the midplane of the current sheet $(x-z)$.

Let us look at the phase speed of the lower hybrid instability which is $5c_A$ at $\Omega_i t = 0.1$ and rises to $8c_A$ at $\Omega_i t = 0.2$. The phase speed of the lower hybrid instabil-

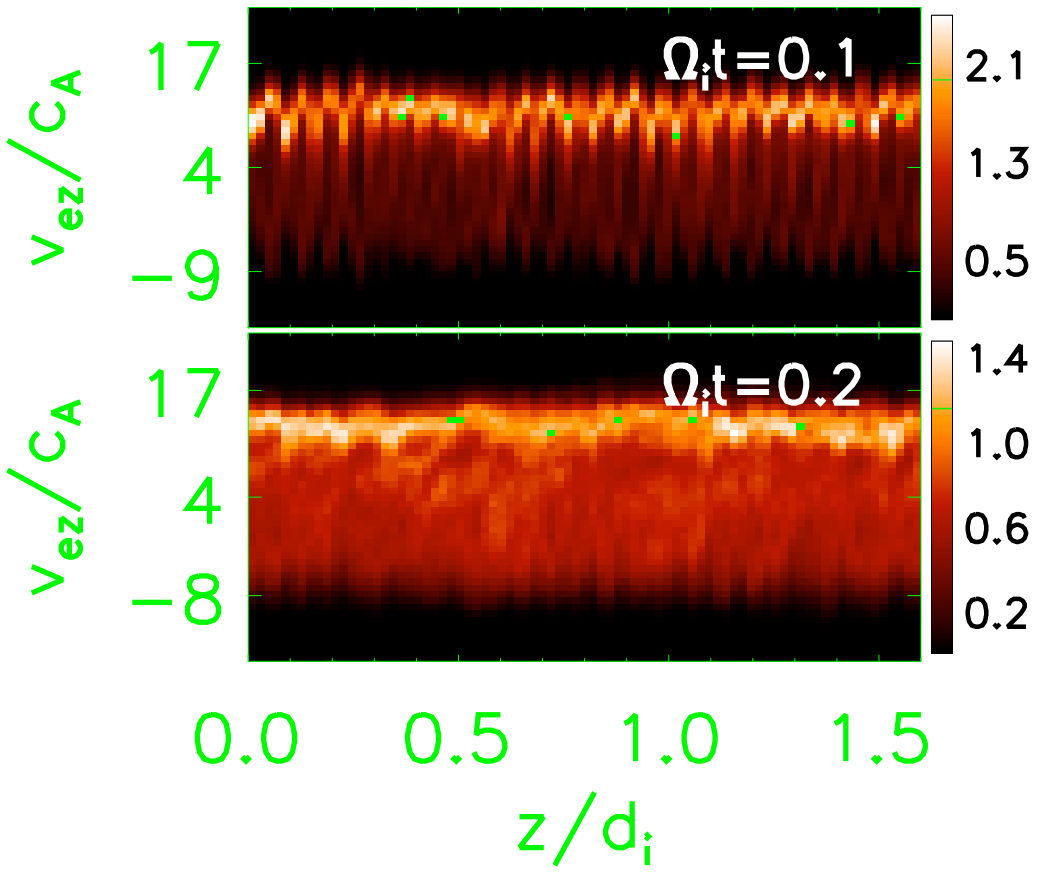

Figure 4.18: Images of electron distributions in phase space (z, v_{ez}) at $\Omega_i t = 0.1, 0.2$.

ity is just above that of the two-stream instability so this instability might suppress the two-stream instability. In the case of $\omega_{pe}/\Omega_e > 1$ the lower hybrid instability was weaker and the phase speed was much larger so the lower hybrid instability was not able to suppress the two-stream mode. We conclude that the lower hybrid dominates at late time when $\omega_{pe}/\Omega_e > 1$. To investigate if the lower hybrid instability has a non-negligible contribution to the parallel momentum transport among electrons, we study the impact of streaming instabilities occurring in the simulations on the formation of electron holes. At $\Omega_i t = 0.05$, from Fig. 4.16 (denoted by black solid lines), we have $|v_{gz} - v_{pz}| \sim 4c_A$, and $E_z \sim 16c_A B_0/c$ with $k_z d_i \sim 90$, then the electron bounce frequency is about $\omega_b/k_z \sim \sqrt{2eE_z/(k_z m_e)} \sim 6c_A$, thus $|v_{gz} - v_{pz}| < \omega_b/k_z$ which marginally satisfies the condition for the formation of electron holes. At $\Omega_i t = 0.1$, $|v_{gz} - v_{pz}| \sim 10c_A$ as obtained from the red dashed lines and E_z increases to $40c_A B_0/c$. The $k_z d_i$ of the two stream instability is about 30 so the corresponding bounce frequency $\omega_b/k_z \sim 16c_A$. Thus $|v_{pz} - v_{gz}| \ll \omega_b/k_z$ and electron holes can form as shown in Fig. 4.18. At $\Omega_i t = 0.2$, $|v_{gz} - v_{pz}| \sim 0$ (denoted by green dash-dotted lines), which is the coherent condition for the strong formation of electron holes. However, though the electron holes continue to survive, the electrons inside the holes are fully randomized as shown in Fig. 4.18. However, since the electrons are so hot it may be difficult to identify coherent structures in such phase space plot.

What causes the thermalization of electrons in phase space at late time? We have shown that the Buneman instability can produce a strong coherent structure in E_z at $\Omega_i t = 0.2$. Is it possible that the strong lower hybrid instability is responsible

for the thermalization? From the theoretical results shown in Fig .4.16, we find that $|v_{pz} - v_{gz}| \sim 0$ for the lower hybrid instability at all time, which is the condition for the stable electron holes. The parallel phase velocity of E_x within the time interval $0.2 - 0.3\Omega_i^{-1}$ is displayed in Fig. 4.17. We see two type of curves. One is horizontal which indicates $v_{pz} \sim 0$, and the other is oblique with $v_{pz} \sim 10c_A$. However, the component of E_z caused by lower hybrid instability is very small for $\theta \sim 80^0$ and in general its frequency is much lower than the two-stream instability. At $\Omega_i t = 0.1$, the frequency of the electron two-stream is about $100\Omega_i$ and the lower hybrid instability is $\sim 40\Omega_i$. Therefore the lower hybrid instability acts weakly on the electrons even though the resonant velocity of the two modes are close to one other (two-stream instability v_{pz} is about $3c_A$ while that of the lower hybrid instability is about $4c_A$). However, at $\Omega_i t = 0.2$, the frequency of the lower hybrid instability is much higher than the Buneman instability (green dash-dotted lines in Fig. 4.16) and the phase speed of the Buneman instability is about zero while the lower hybrid instability is about $10c_A$. These conditions make it possible for the lower hybrid instability to interact with the electrons at $v_{pz} \sim 10c_A$ as the Buneman instability interacts with the electrons at low velocity.

How are the electrons are thermalized by these coupled interactions? The interaction velocity range of the Buneman instability is about $v \sim v_{pz} \pm \sqrt{\frac{2eE_z}{k_z m_e}} \sim \pm 10c_A$ and the interaction velocity range of the lower hybrid instability is about $v \sim v_{pz} \pm \sqrt{\frac{2eE_x cot\theta}{k_x m_e}} \sim 10 \pm 4c_A$ which ranges from $6 - 14c_A$. Thus the velocity resonances overlap over $6 - 10c_A$, which allows the low velocity electrons to gain momentum from high velocity electrons. This is consistent with the electron distribution function in

Fig. 4.14 where the long tail caused by the wave-electron resonances is observed to extend to high velocity at late time.

4.4 Conclusion

We have studied both the cases with $\omega_{pe}/\Omega_e < 1$ and $\omega_{pe}/\Omega_e > 1$.

In the case of $\omega_{pe}/\Omega_e < 1$, we have shown that in strongly magnetized plasmas, both theory and 3D simulations reveal two distinct phases. First, the parallel Buneman instability grows and traps low velocity electrons. Second, the Buneman instability evolves into two distinct instabilities: the parallel two-stream instability and the nearly-perpendicular lower hybrid instability. The two-stream instability continuously sustains the electron holes that first formed due to the Buneman instability while the lower hybrid instability drives turbulence in the perpendicular direction. The high phase speed of the waves at late time couples the highest velocity streaming electrons to the ions and low velocity electrons.

In the case of $\omega_{pe}/\Omega_e > 1$, we have observed three distinct phases of the development of streaming instabilities from both kinetic theory and 3D simulations. First, the Buneman instability develops and quickly decays. Second, the Buneman instability is taken over by a weak electron two-stream instability and strong lower hybrid instability. Third, the electron two-stream instability stops growing, and instead, a new Buneman instability with longer wavelength overtakes and grows with a growth rate comparable to that of the lower hybrid instability. The lower hybrid instability interacts with high velocity electrons and transfers the momentum

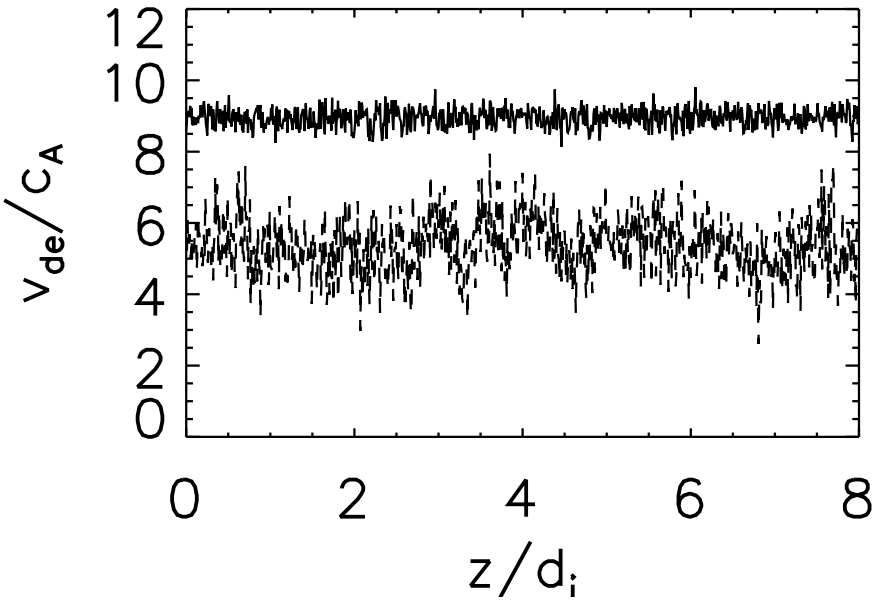

Figure 4.19: Cuts of the electron drift $v_{de} = -j_{ez}/en_e$ in the midplane $x - z$ of the current sheet at $\Omega_i t = 0.4, 1.6$ in the solid and dashed lines, respectively.

to low velocity electrons in phase space to feed the growth of the Buneman instability.

During reconnection the electron two-stream and lower hybrid instabilities might prevent high velocity electrons runaway, facilitating the breaking of the frozen-in condition required for fast reconnection. Through the turbulence, the kinetic energy of electron streaming is converted into the thermal energy of electrons. The drift velocity drops while the thermal velocity of electrons increases significantly. Fig. 4.19 shows the cuts of current along z at midplane $x - z$ of current sheet at $\Omega_i t = 0.4, 1.6$. The drift velocity of the electrons drops from the initial value at $10c_A$ to $6c_A$ within a time interval of $1.2\Omega_i^{-1}$ through turbulence induced drag.

Chapter 5

Nonlinear Development of Streaming Instabilities in 3D Magnetic Reconnection

We have discussed 3D PIC simulations of magnetic reconnection in Chapter III. In the low temperature simulations of 3D magnetic reconnection with a guide field, the Buneman instability occurs around the x-line at the beginning of the simulations. A major difference between the simulation of magnetic reconnection with a guide field and the simulations introduced in Chapter IV is the reconnection electric field produced around the x-line in magnetic reconnection simulations. This reconnection electric field accelerates electrons and drives an intense beam. How the development of streaming instabilities are affected by the acceleration of electron streams is poorly understood (Omura et al. 2003; Rowland et al. 1981). In this chapter we will perform detailed analysis of the evolving development of streaming instabilities in the simulations of the low temperature magnetic reconnection that we have discussed in Chapter III.

In this chapter, we show that Buneman instabilities occur at the beginning of the magnetic reconnection simulations but then the Buneman instability decays and the lower hybrid instability dominates. Electron-electron two stream instabilities do not develop. Parallel to the magnetic field, the lower hybrid waves resonate with the electrons at higher velocity and form electron holes which move at high speed

along the magnetic field. Late in time the lower hybrid instability drags electrons to low velocity, which again drives the Buneman instability. The instability forms electron holes which move slowly along magnetic field. The overlapping of resonance of the Buneman instability and the lower hybrid instability feeds the growth of the Buneman instability and stabilizes the lower hybrid instability. Perpendicular to the magnetic field, the lower hybrid waves resonantly interact with the ions and enables the transfer tmomentum from electrons to ions.

5.1 Lower Hybrid Instability Dominating Evolution

At the beginning of simulations, the Buneman instability is driven by the electron streaming around x-line. The resonance velocity is around $[m_e/(2m_i)]^{1/3}v_{de} \sim -0.68c_A$, where the initial electron drift velocity v_{de} is $-4c_A$. From the electron distribution function at $\Omega_i t = 1$ in Fig. 5.1, we see a bump caused by inverse-Landau damping appearing around the resonance velocity.

The Buneman instability creats strong bipolar structures and these bipolar structures evolve into two distinct structures at late time. In Fig. 5.2, at $\Omega_i t = 3$, the spatial structures of the electric field E_z around the x-line ($x \sim 1d_i$) is characterized by the round holes while the spatial structures of electric field E_x is characterized by the oblique strips. The similar structures appeared before in the simulations with $\omega_{pe}/\Omega_e < 1$ introduced in Chapter IV. A natural question is whether these structures are caused by the same physical processes?

Fig. 5.3 shows the power spectra of $|E_x(k_x, k_z)|^2$ and $|E_z(k_x, k_z)|^2$. The power

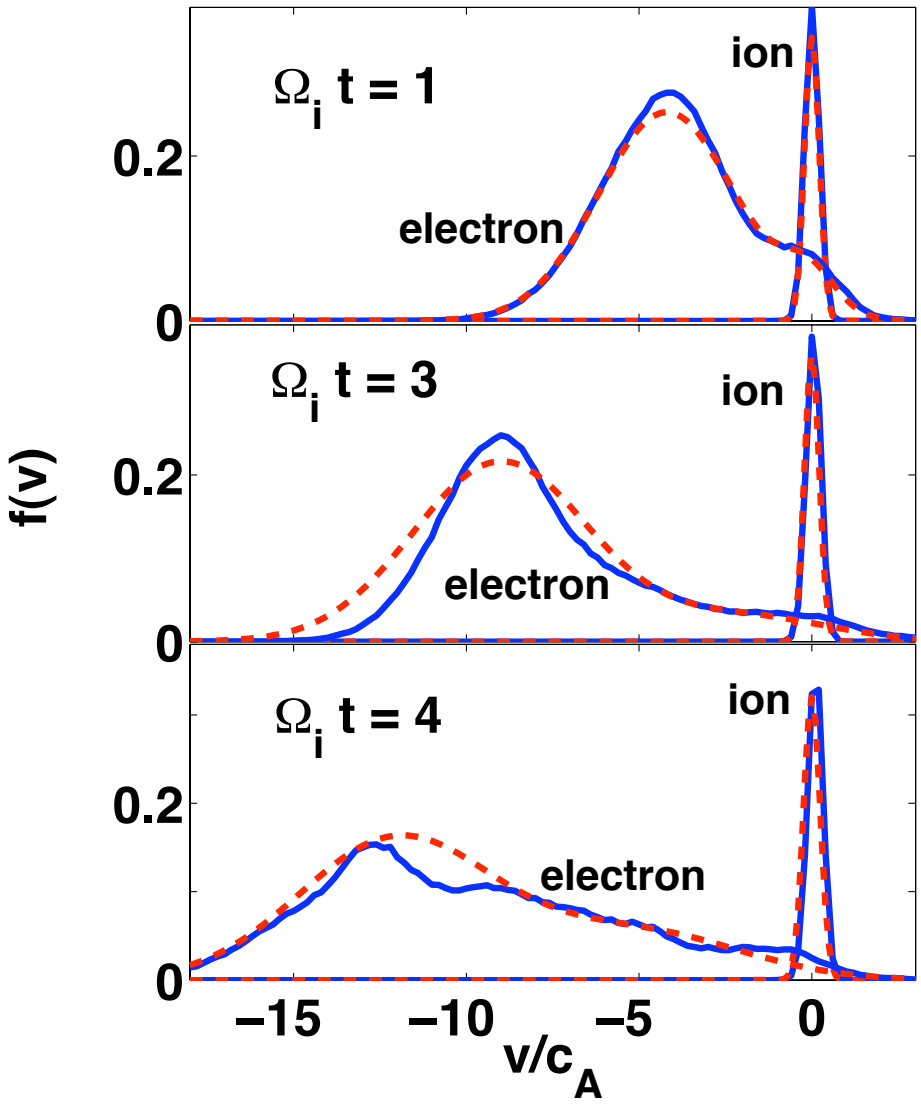

Figure 5.1: Electron and ion distribution functions around the x-line at $\Omega_i t = 1, 3, 4$. The blue solid lines are the distribution functions from the magnetic reconnection simulations and the red dashed lines are the theoretical fitting by the double-drifting Maxwellian model.

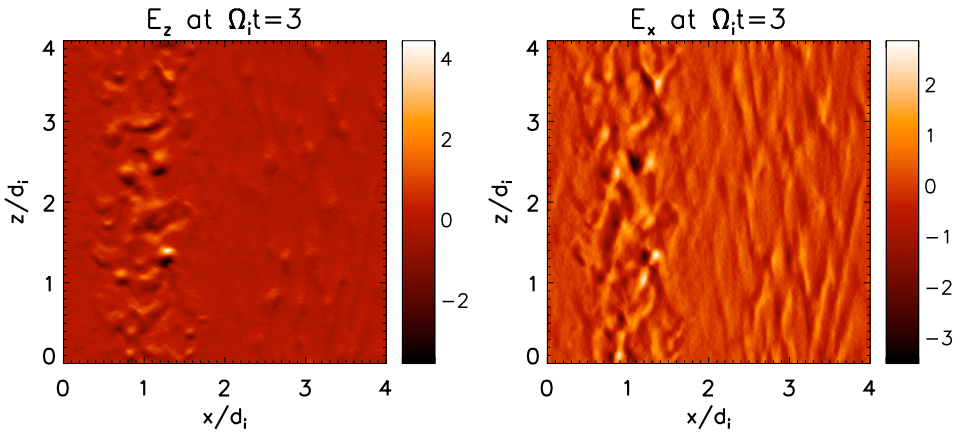

Figure 5.2: Spatial structures of E_x and E_z at $\Omega_i t = 3$ in the midplane of the current sheet $(x - z)$.

spectra of E_z shown by Fig. 5.3 (b, d, e) has a peak around $(k_x d_i, k_z d_i) \sim (0, 20)$ with width $(\delta k_x d_i, \delta k_z d_i) \sim (10, 10)$. Another peak has a large $k_\perp$ with $(k_x d_i, k_z d_i) \sim (30, 10)$.

To learn more about the two unstable bands appearing during reconnection, in Fig. 5.4 we plot cuts of $E_x(z)$ and $E_z(z)$ along z around the x-line at a series of times. The movement of the peaks and valleys form curves. The slope of these curves is the phase speed v_{pz}. Before $\Omega_i t = 1$, the slopes calculated from both E_x and E_z are around $v_{pz} \sim -1 c_A$, which is close to the resonance phase speed of Buneman instability. At late time, two different phase speed appear, one is about $-0.3 c_A$ and the other is about $-6 c_A$ which means there are two different waves acting on the electrons. This is substantially different from the results we obtained in the corresponding simulations in chapter IV. What are these waves and what role do they play in the formation of the electron holes?

To investigate the detailed physics, we calculate the theoretical spectra using

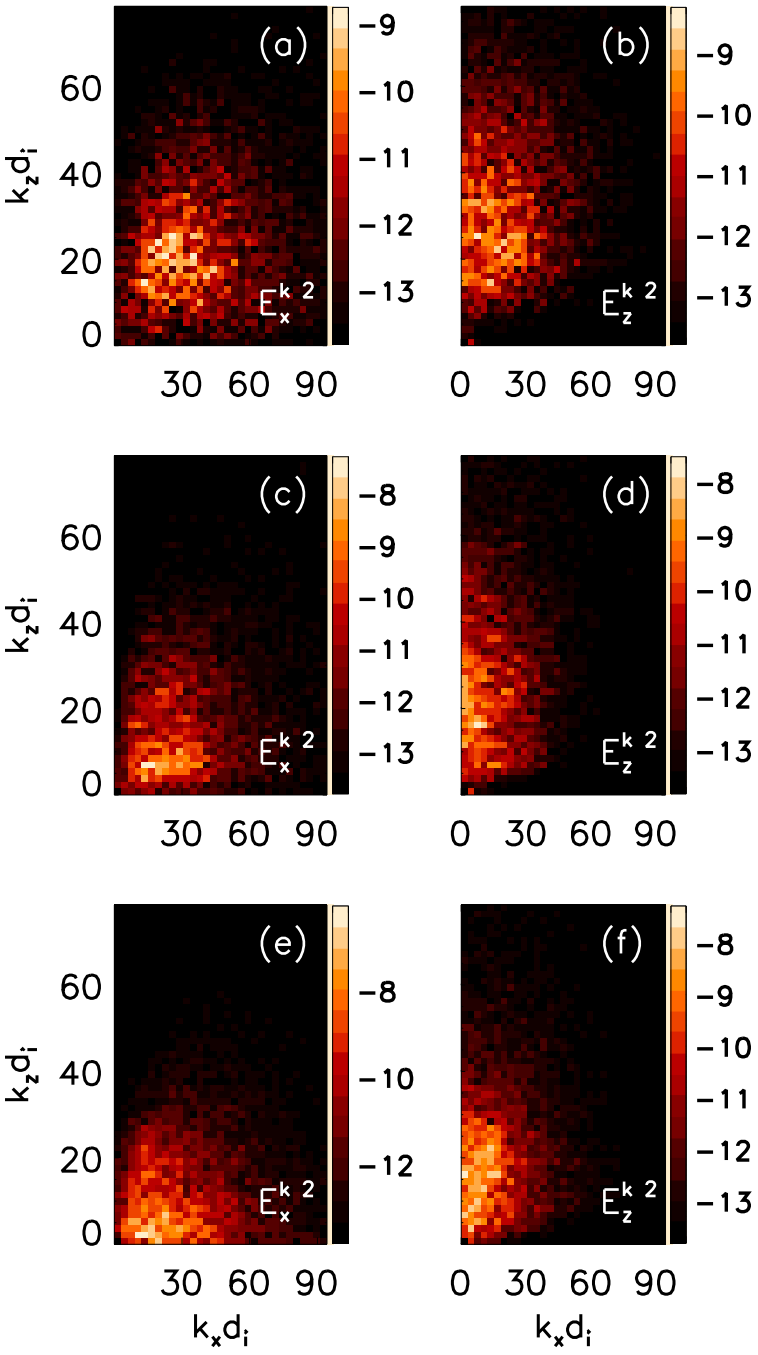

Figure 5.3: 2D power spectra $|E_x(k_x, k_z)|^2$ and $|E_z(k_x, k_z)|$ at $\Omega_i t = 1, 3, 4$ in the midplane of the current sheet $(x - z)$, denoted by (a,b), (c,d), (e,f), respectively. The power spectra are shown in logarithmic scale.

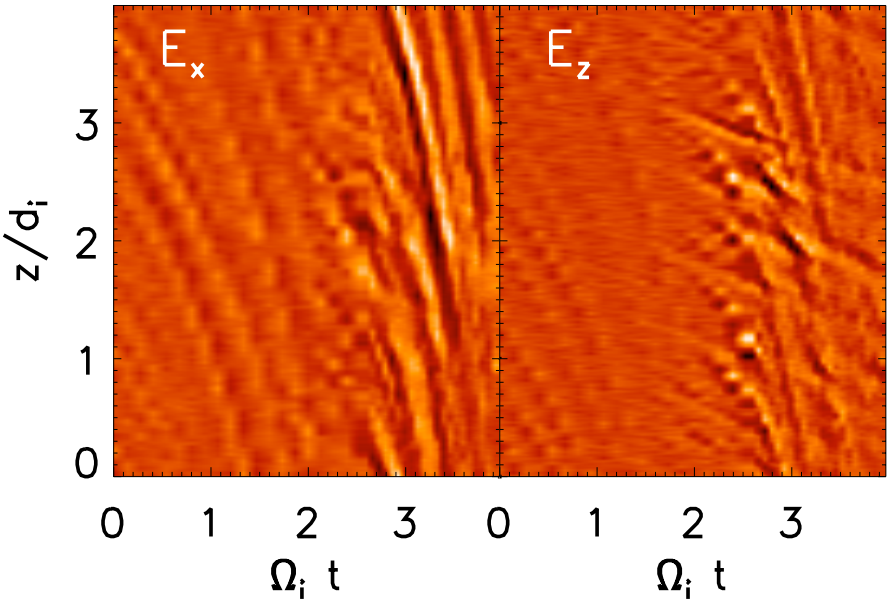

Figure 5.4: The cuts of $E_x(z)$ and $E_z(z)$ along z at x-line versus time. The slope of the curves is the phase speed v_{pz}.

the double-Drifting Maxwellian model with the dispersion relation obtained earlier for waves with $\Omega_i \ll \omega \ll \Omega_e$:

$$1 + \frac{2\omega_{pi}^2}{k^2 v_{ti}^2}[1 + \zeta_i Z(\zeta_i)] + \frac{2\delta\omega_{pe}^2}{k^2 v_{te1}^2}[1 + I_0(\lambda)e^{-\lambda}\zeta_{e1} Z(\zeta_{e1})] + \frac{2(1-\delta)\omega_{pe}^2}{k^2 v_{te2}^2}[1 + I_0(\lambda)e^{-\lambda}\zeta_{e2} Z(\zeta_{e2})] = 0,$$

where $\zeta_i = (\omega - k_z v_{di})/k v_{ti}$, $\zeta_{e1} = (\omega - k_z v_{de1})/k_z v_{zte1}$, $\zeta_{e2} = (\omega - k_z v_{de2})/k_z v_{zte2}$, $\lambda = k_x^2 v_{xte}^2/2\Omega_e^2$, δ is the weight of low velocity drifting Maxwellian, Z is the plasma dispersion function and I_0 is the modified Bessel function of the first kind with order zero. The thermal velocity of species j is defined by $v_{tj}^2 = 2T_{tj}/m_j$ and drift speed by v_{dj}, which is parallel to the magnetic field (z direction). The ions are taken to be isotropic.

The fitting parameters of distribution functions denoted by red dashed lines in

Table 5.1: Parameters of Model Dist. Funs.

	v_{zte1}	v_{zte2}	v_{de1}	v_{de2}	v_{ti}	v_{di}	δ
$\Omega_i t$= 1	2.8	1.1	-4.2	-0.1	0.3	0	0.07
$\Omega_i t$= 3	3.6	3.5	-9.0	-2.0	0.3	0	0.16
$\Omega_i t$= 4	4.0	4.2	-9.0	-5.0	0.34	0.1	0.26

Fig. 5.1 are listed in the table 5.1. Note that the fitting is not as good as in the case of $\omega_{pe}/\Omega_e < 1$ in Chapter III,the resulting wave spectra seem to fit simulations very well. Note that δ increase more than 30 times from $\Omega_i t = 1$ to $\Omega_i t = 4$, which means that high velocity electrons are diffused into the low velocity band, as indicated by the increasing of v_{zte2} which is the thermal velocity of the low velocity electrons.

The corresponding theoretical unstable modes obtained from the dispersion relation are shown in Fig. 5.5. Fig. 5.5 (a) is the spectrum at $\Omega_i t = 0$. Initially electron distribution function is a single Maxwellian, and the Buneman instability has a peak growth rate around $k_z d_i \sim 25$, which is two times smaller than the wavenumber of fast growing mode from cold plasma limit $k_z \sim \omega_{pe}/v_{de} \sim 50/d_i$. The growth rate of the fastest growing mode is $\gamma_{max} \sim 5$, much lower than the cold plasma limit $\gamma_{max} \sim \sqrt{3}\omega_{pe}/2[(m_e/2m_i)^{1/3}] \sim 28$. These differences are caused by the thermal effects. In this regime the Buneman instability needs to be treated as a kinetic rather than a fluid-like instability.

At $\Omega_i t = 1$, the parallel mode shifts to $(k_x d_i, k_z d_i) = (0, 20)$ and remains steadily at the same location during the reminder of the simulation, which is con-

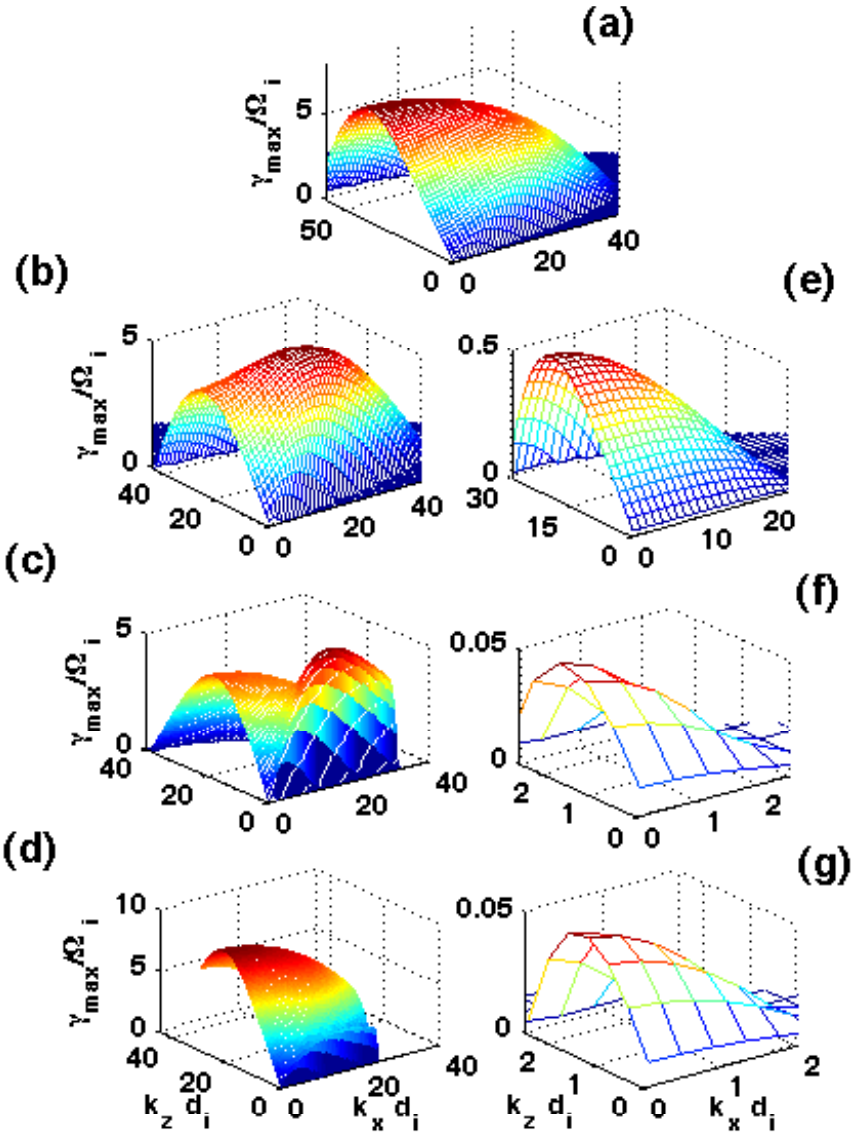

Figure 5.5: From the top to the bottom, theoretical spectra obtained by the double drifting Maxwellian model at $\Omega_i t = 0, 1, 3, 4$, respectively. (a), (b), (c) and (d) obtained from contribution of both electrons and ions; (e), (f) and (g) obtained from the contribution of electrons, but neglecting that of the ions.

sistent with the parallel mode we found in the power spectra from the simulations shown in Fig. 5.3. Is this mode still the Buneman instability or is it the electron-electron two-stream instability? To answer this question, we exclude the ions and the spectra produced by the remaining electrons at $\Omega_i t = 1, 3, 4$ are shown by Fig. 5.5 (e, f, g). The surviving mode is an electron-electron two-stream instability whose growth rate and k_z are much smaller than the Buneman mode. Thus we conclude that the parallel mode is still the kinetic Buneman instability.

A second mode appears at $\Omega_i t = 1$ around $(k_x d_i, k_z d_i) = (35, 20)$, and at $\Omega_i t = 3$, this mode moves to around $(k_x d_i, k_z d_i) = (30, 10)$, and becomes dominant. Gradually this nearly-perpendicular mode weakens and becomes very weak at $\Omega_i t = 4$. This mode is the nearly-perpendicular mode we discussed in Fig. 5.3.

What is the nearly-pependicular mode? Why does it weaken while the parallel Buneman instability remains steady? To answer these questions, we calculate the parallel phase speed v_{pz}, frequency ω and group velocity v_{gz} for unstable waves around the x-line and show the evolution of the physical parameters of fastest growing mode versus θ, the angle between the wave vector and the magnetic field. The results are shown in Fig. 5.6.

At $\Omega_i t = 1$, shown by black solid line, the phase speed v_{pz} of both the parallel and nearly-perpendicular modes is around $1c_A$. This is consistent with the phase speed for both E_x and E_z propagating along z at early time in the simulations which is shown in Fig. 5.4. At late time, the phase speed of the parallel mode is still around $-1c_A$ consistent with the Buneman instability while the nearly -perpendicular mode goes up to $-4c_A$ at $\Omega_i t = 3$, and $-7c_A$ at $\Omega_i t = 4$. These two modes have comparable

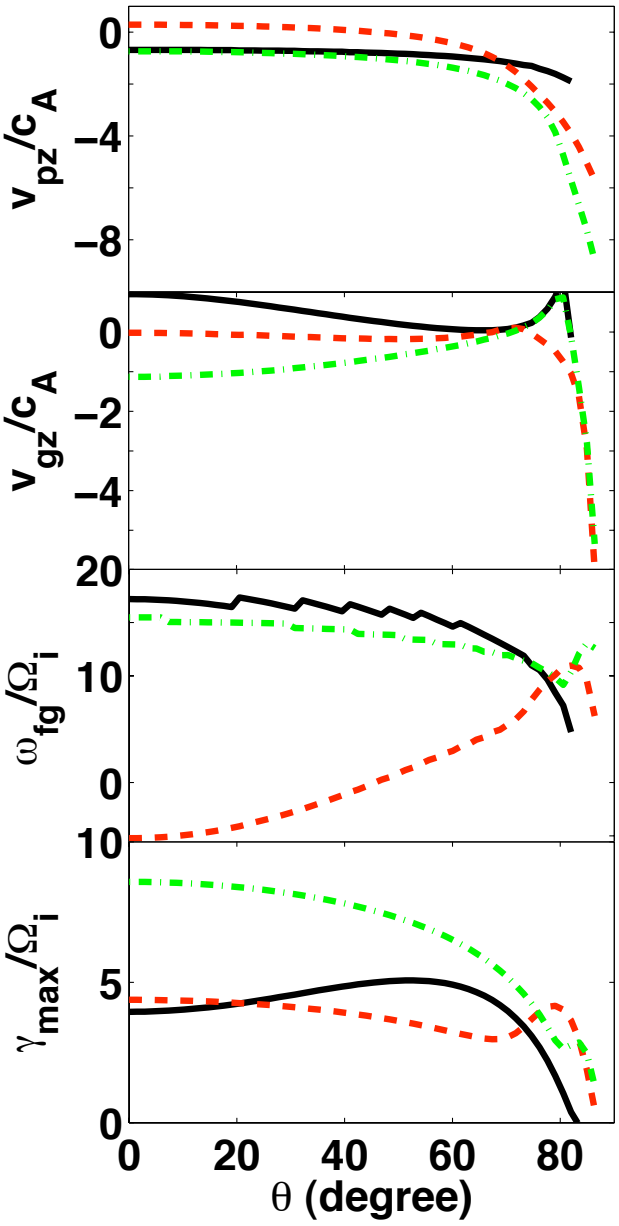

Figure 5.6: Theoretical phase velocity v_{pz}, group velocity v_{gz}, frequency ω_{fg} and maximal growth rate γ_{max} of the fastest growing mode around the x-line versus angle θ between the wave vector and the magnetic field. Black solid line, red dashed line and green dash-dotted line denote the results at $\Omega_i t = 1, 3, 4$, respectively.

growth rates during the evolution of the system, so we observe two distinct phase speeds at late time. The parallel waves resonate with the low velocity electrons while the nearly -perpendicular waves resonate with the high velocity electrons.

Unlike the parallel mode, the frequency of the nearly-perpendicular mode at different times is around $\omega_{fg} \sim 10\Omega_i$, about half of the frequency of the cold plasma limit for the lower hybrid frequency $\omega_{lh} = \omega_{pi}/(1+\omega_{pe}^2/\Omega_e^2)^{1/2} + k_z v_{di} \sim 18.5\Omega_i$. The nearly-perpendicular mode should be the lower hybrid instability, which resonates with ions moving perpendicular to $\mathbf{B}$. To further investigate this perpendicular mode, we show in Fig. 5.7 the perpendicular phase speed v_{px} around the x-line from simulations and the kinetic theory. v_{px} of the E_x waves around the x-line propagating along x in the simulations is obtained by stacking the cuts of E_x along x at successive times. $|v_{px}|$ increases from $\sim 0.2c_A$ at $\Omega_i t = 1$ to $\sim 0.8c_A$ at $\Omega_i t = 4$. v_{px} is symmetric with respect to the magnetic field so v_{px} is either positive or negative. This is consistent with the theoretical calculation shown in Fig. 5.7. The nearly-perpendicular mode has strong interactions with ions since its phase speed is within the thermal range of the ion distribution function. Thus we confirm that this perpendicular mode is the lower hybrid instability.

The perpendicular waves propagate along x and are dissipated as they heat the ions. Fig. 5.8 shows the ion distribution functions at $\Omega_i t = 1, 3, 4$ in the blue solid line, red dashed line and green dash-dotted line, respectively. We see that the width of the ion distribution function become wider at late time, but not significantly. So this indicates that the lower hybrid wave only transfers a small fraction of the energy from high velocity electrons to ions. Where does the majority of the energy

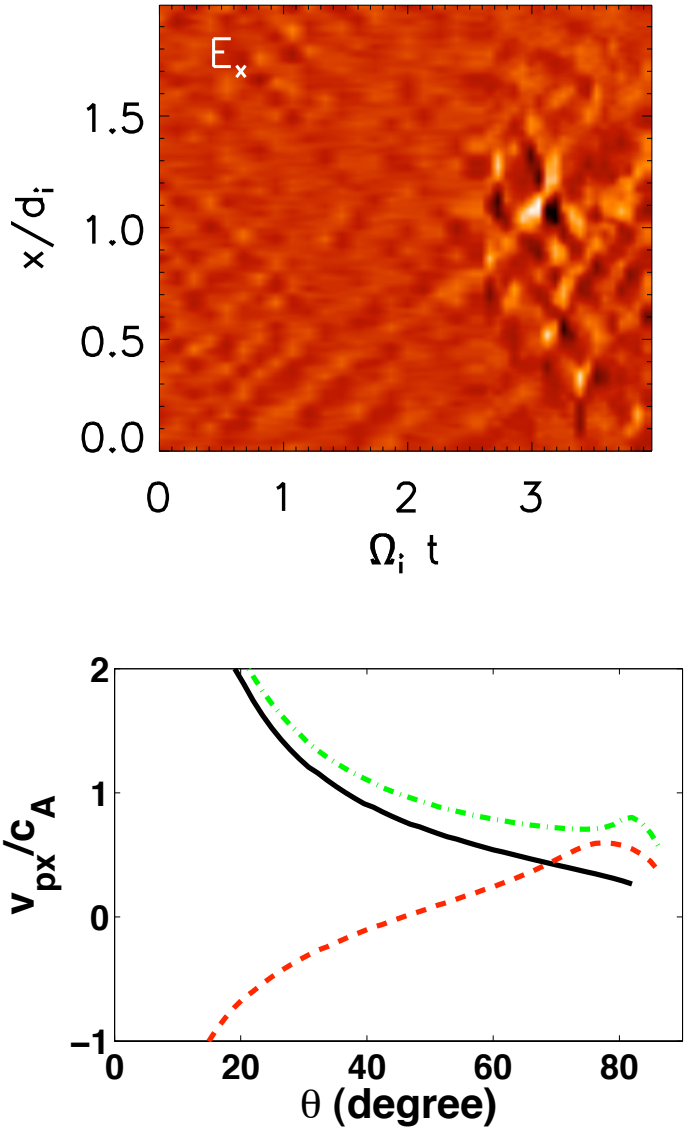

Figure 5.7: Perpendicular phase speed v_{px}. Top: the stack plot of the cuts of $E_x(x)$ around the x-line in 3D magnetic simulations at successive times that trace the motion of peaks or valleys of the wave E_x along x. Bottom: Theoretical perpendicular phase speed v_{px} versus the angle θ at $\Omega_i t = 1, 3, 4$, denoted by black solid, red dashed and green dash-dotted lines, respectively.

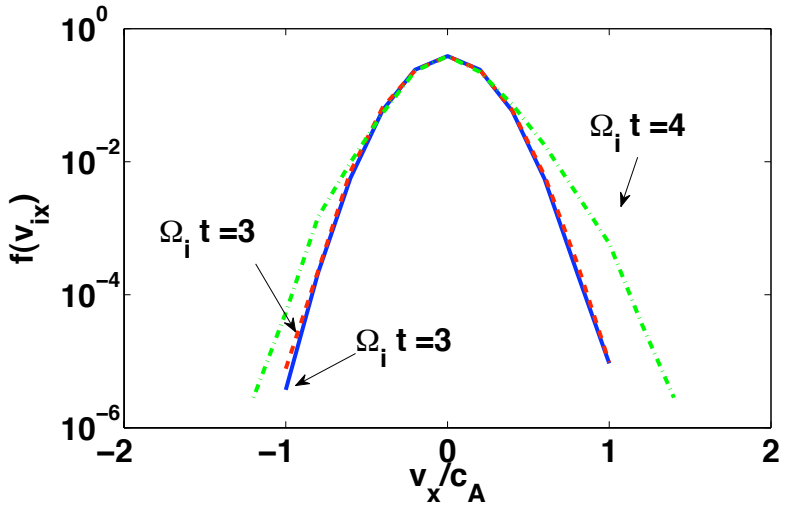

Figure 5.8: Ion distribution function for v_x at $\Omega_i t = 1, 3, 4$, denoted by blue solid line, red dashed line and green dash-dotted line, respectively.

go?

The evolution of the streaming instabilities is now clear, but two puzzles remain. One is what continuously supports the Buneman instability and the other is what is the sink of the momentum transferred from the high velocity electrons by lower hybrid instability. The answers to these two questions are the keys to understanding the coherent relation that builds up among the instabilities and the mechanism of momentum transport in this turbulence.

The formation condition of electron holes is $|v_{pz} - v_{gz}| < \sqrt{2e|\phi|/m_e}$. At $\Omega_i t = 1, 4$, $\sqrt{2e|\phi|/m_e} \sim 3c_A$ for the parallel Buneman instability and $\sqrt{2e|\phi|/m_e} \sim 1.6c_A$ for the lower hybrid instability, where we calculate $\phi = E_x ctan\theta/k_x$ for the lower hybrid instability, and $\phi \sim E_z/k_z$ for the Buneman instability using $E_x \sim E_z \sim 1c_A B_0/c$ and $k_z d_i \sim 20$. At $\Omega_i t = 3$, for the Buneman instability $\sqrt{2e|\phi|/m_e} \sim 5c_A$ and for the lower hybrid instability $\sqrt{2e|\phi|/m_e} \sim 3c_A$, where we take $E_z \sim E_x \sim$

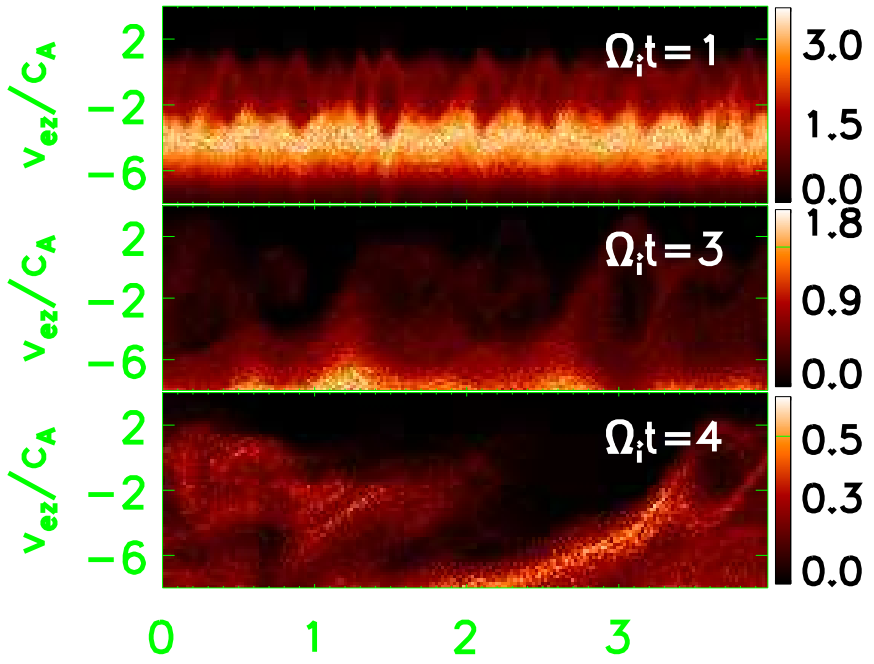

Figure 5.9: Electron distribution functions in phase space (z, v_{ez}) at $\Omega_i t = 1, 3, 4$. The intensity of $f(v_{ez}, z)$ is lowered by 10^4 times.

$2c_A B_0/c$. Going back to Fig. 5.6, we find that both the Buneman instability and the lower hybrid instability satisfy $|v_{pz} - v_{gz}| \sim 0$. Therefore, both instabilities can lead to the formation of stable electron holes. This conclusion is supported by the two phase speeds observed around the x-line in the simulations of 3D magnetic reconnection (Fig. 5.4): one has a velocity close to zero while the other moves much faster. These observations from the simulations are consistent with the low phase speed v_{pz} and group velocity v_{gz} for the Buneman instability and high v_{pz} and v_{gz} for the lower hybrid instability.

Electron distribution functions in phase space (z, v_{ez}) are shown in Fig. 5.9. At $\Omega_i t = 1$, the resonance velocity range for the Buneman instability is around

$-4c_A < v < 2c_A$ and for the lower hybrid instability is $-2.6c_A < v < 0.6c_A$, where we have used the relation $|v - v_p| < \sqrt{2e\phi/m_e}$. The overlapping of the resonant velocities within $-2.6c_A < v < 0.6c_A$ causes the chaotic motion of electrons in phase space. The frequency of the lower hybrid wave is close to the frequency of the Buneman instability, so the action of the lower hybrid instability on the electrons is as important as that of the Buneman instability. At $\Omega_i t = 3$, the resonance velocity range is $-5c_A < v < 5c_A$ for the Buneman instability and $-8c_A < v < 1c_A$ for the lower hybrid instability. The overlapping resonant velocity range is $-5c_A < v < 1c_A$. When the electrons circulate in the phase space in this velocity range, the momentum is transferred from high velocity electrons to low velocity electrons. This process continues to provide sufficient energy for the growth of Buneman instability and gradually stabilizes the lower hybrid instability. Such stochastic motion of electrons also might lead to the destruction of electron holes. At $\Omega_i t = 4$, the lower hybrid instability is weak and the Buneman instability drives the unstable waves. The lower hybrid instability is too weak to continuously produce electron holes and most of the electron holes vanish. A few new holes form because of the Buneman instability. These holes trap electrons in the phase space $-3c_A < v < 3c_A$. This is consistent with the hole appearing at $(z, v_p) \sim (3.7, 0)$ in Fig. 5.9. These holes quickly decay because of the saturation of the Buneman instability when the lower hybrid instability has been stabilized.

The momentum is finally transported from high velocity electrons to ions through the interaction of the lower hybrid and Buneman instabilities.

5.2 Conclusion

In this chapter, we analyzed the nonlinear development of streaming instabilities in 3D magnetic reconnection. The major difference from the simulations in Chapter IV is that the electron-electron two-stream instability does not appear. The phase speed of the lower hybrid instability increases from about zero to high velocity. This instability suppresses the electron two-stream instability, whose resonant velocity is similar to that of the lower hybrid instability. Playing a similar role to the Buneman instability, the lower hybrid waves resonate with parallel moving electrons and cause the formation of electron holes. Through the overlapping of resonances in phase space, the lower hybrid instability transfers momentum from high velocity electrons to low velocity electrons which act as the energy source for the growth of the Buneman instability, and which finally transfers the momentum to the ions. The overlapping of the resonances also leads to the destruction of the electron holes.

The formation and destruction of electron holes redistribute the energy in electron velocity space. Anomalous resistivity is enhanced by the momentum transfer in phase space. As we have shown in Chapter III, the acceleration of the electrons at the x-line decreases to zero at late time in the simulations of the low temperature reconnection since the reconnection electric field being balanced by the turbulence drag. Note, however the turbulent dissipation does not increase the magnetic reconnection rate which is consistent with the insensitivity of reconnection to dissipation mechanism documented earlier (Shay & Drake 1998; Hesse et al. 1999; Birn et al.

2001).

Chapter 6

Conclusions and Discussions

We have discussed the nonlinear development of streaming instabilities in three different simulations which are based on a similar initial configuration. Two simulations are designed to focus on streaming instabilities in the absence of reconnection — the limited domain size in the direction perpendicular to the direction of electron drift inhibits reconnection. The streaming velocity is high enough for the Buneman instability to grow at the beginning of the simulations. Case 1 has $\omega_{pe}/\Omega_e = 0.4$ and case 2 has $\omega_{pe}/\Omega_e = 1.6$. Case 3 is a simulation of magnetic reconnection with $\omega_{pe}/\Omega_e = 0.4$.

In these three cases, the development of the nonlinear streaming instabilities are similar but there are significant differences. What is common in these three cases? What important physics has been clarified? What physics remains unclear?

In case 1, the Buneman instability (BI) dominates early but is overpowered by the electron-electron two-stream instability (ETS). The phase speed of the ETS increases with time and waves resonate with the high velocity electrons at late time, which sustains the formation of electron holes after the saturation of Buneman instability. The nearly-perpendicular lower hybrid instability (LHI) is weak and its parallel phase speed is very high. The high phase speed allows momentum to be transfered from high velocity electrons to low velocity electrons and ions.

In case 2, the electron-electron two-stream instability (ETS) again overpowers the Buneman instability (BI) early in time and in turn is overpowered by the lower hybrid instability (LHI). The parallel phase speed of the lower hybrid instability exceeds that of the Buneman instability and then further increases with time. The lower hybrid instability dominates and resonates with the fast electrons, which quenches the electron-electron two-stream instability. The momentum flows from fast electrons to slow electrons through overlapping of resonances (OLR) of the BI and LHI in phase space. The LHI therefore feeds the growth of the Buneman instability, which becomes comparable in strength to the lower hybrid instability at late time. The width of the resonance velocity is estimated to be $|v - v_p| \sim \sqrt{2e\phi/m_e}$ where ϕ is the amplitude of the potential of the electrostatic waves.

In case 3, the electron beams around the x-line are accelerated by the magnetic reconnection electric field from $4c_A$ to $10c_A$ until the turbulence drag balances the acceleration (see Chapter III). The Buneman instability occurs at the beginning of the simulations and then the lower hybrid instability dominates. The parallel phase speed of the nearly perpendicular lower hybrid instability starts off close to zero and increases to high velocity at late time. The electron-electron two-stream instability is suppressed. The overlapping resonance (OLR) of the BI and LHI again transfers the momentum from high velocity electrons to low velocity electrons, which sustains the growth of Buneman instability and eventually weakens the lower hybrid instability. Both the Buneman instability and the lower hybrid instability can form electron holes.

In all of these three simulations, turbulence dissipates the kinetic energy of

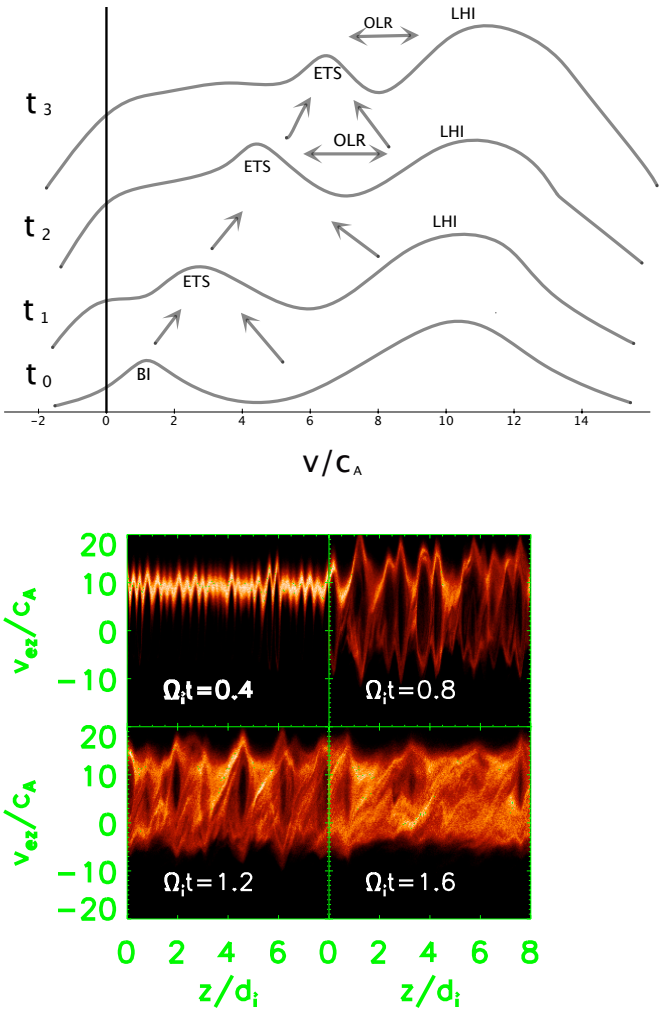

Figure 6.1: Top: a schematic for the evolution of the electron distribution function in case 1 ($\omega_{pe}/\Omega_e = 0.4$). Bottom: Electron distribution function in phase space $z - v_{ez}$ in case 1.

the electron beams into thermal energy of electrons and ions.

From the results summarized above, we have developed a global picture of the competition between the electron-electron two stream (ETS) and lower hybrid instability (LHI), the momentum transport by the turbulence and the turbulent dissipation. In the following, three schematic diagrams of the evolving electron distribution function show the competition among the streaming instabilities.

In Fig. 6.1, the schematic diagram of the electron distribution function shows the evolution of streaming instabilities in case 1 with $\omega_{pe}/\Omega_e = 0.4$. In this case the BI traps low velocity electrons, forming an electron distribution with two distinct peaks. These peaks cause the ETS to grow. The electron-electron two-stream instability continues to drive electron holes at late time. In parallel with the ETS, the LHI develops and resonates with high velocity electrons. The range of the resonance velocity of the two-stream and the lower hybrid instabilities overlap at late time, and the electron trajectory become chaotic, destroying the electron holes (see the electron distribution function in phase space at time $\Omega_i t = 1.2, 1.6$).

In Fig. 6.2, we can see the difference of the evolution of the streaming instability between case 2 and case 1. In both cases, BI occurs first and then leads to the ETS. The difference is that the LHI resonates with electrons at a velocity just above the the resonance velocity of two-stream instability, which blocks the development of two-stream instability. Instead, the Buneman instability grows and the parallel speed of the lower hybrid instability increases with the time. The increasing parallel phase speed of the LHI enables it to tap the energy of high velocity electrons and pull them down to low velocity where they in turn drive the BI. The overlapping of resonance causes the trajectories of electrons in the phase space to be completely randomized (see the electron distribution function in phase space at time $\Omega_i t = 0.2$).

In Fig. 6.3, we show the schematic evolution of electron distribution function in 3D magnetic reconnection. Case 3 has the same ratio of ω_{pe}/Ω_e as case 1, but the development of the streaming instability is more like case 2. After the initial BI saturates, the LHI grows and resonates with the intermediate velocity electrons. As

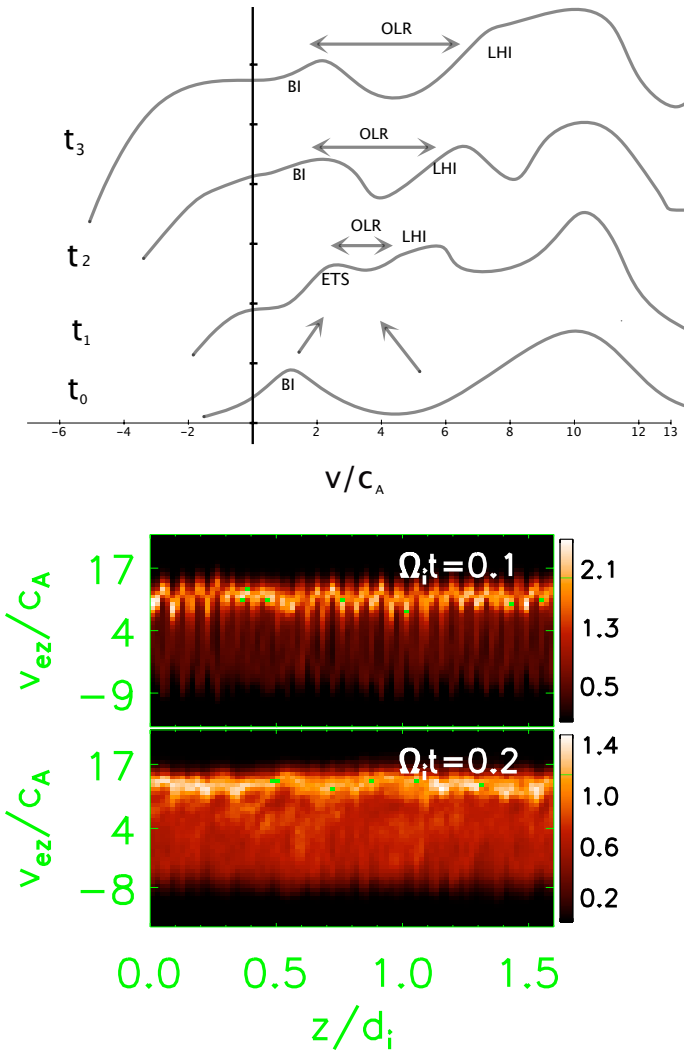

Figure 6.2: Top: a schematic for the evolution of electron velocity distribution function in case 2 ($\omega_{pe}/\Omega_e = 1.6$). Bottom: Electron distribution function in phase space $z - v_{ez}$ in case 2.

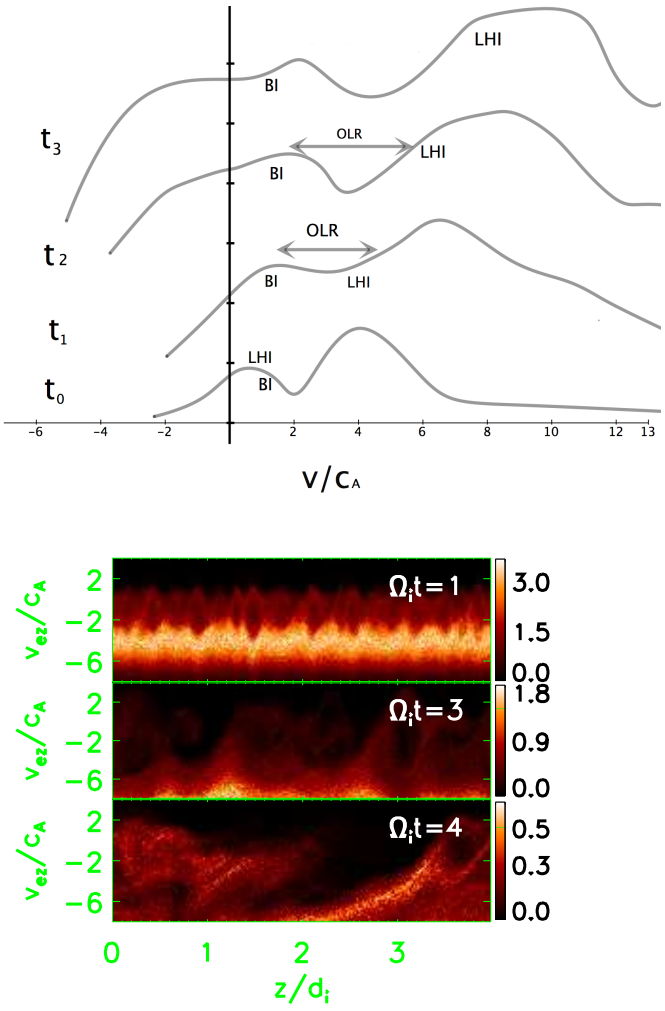

Figure 6.3: Top: a schematic for the evolution of electron velocity distribution function in case 3 ($\omega_{pe}/\Omega_e = 0.4$) with reconnection. Bottom: Electron distribution function in phase space $z - v_{ez}$ in case 3.

a result the ETS is completely suppressed. The parallel phase speed of the LHI then increases with time, which leads to the fast growth of the LHI as it taps the energy of high velocity electrons. The LHI quickly dominates the dynamics. As in case 2, the overlapping of the resonance between the BI and the LHI sustains the BI and finally weakens the LHI. The resulting chaotic motion of electrons in phase space destroys the electron holes formed by the Buneman and lower hybrid instabilities.

From these three cases, we can conclude:

1: Lower hybrid instability dominates the development of streaming instabilities in low β plasma. The growth of electron-electron two-stream instability or Buneman instability depends on the parallel phase speed of the lower hybrid instability. If its parallel phase speed is larger and leaves sufficient velocity space for electron-electron two-stream instability to grow, the two-stream instability takes over the Buneman instability and can dominate the process. If not, then the two-stream instability will be suppressed and the Buneman instability grows.

2: The instability with the high phase speed can tap the energy of the high velocity electrons and dominate the process, like the electron two-stream instability in case 1 and the lower hybrid instability in cases 2 and 3. The strong lower hybrid instability can also form electron holes.

3: The condition for the formation of stable electron holes requires $|v_p - v_g| < \sqrt{2e|\phi|/m_e}$, where ϕ is the amplitude of the electric potential.

4: The overlapping resonance in phase space is the dominant mechanism for transporting the momentum and energy from the high velocity electrons to the low velocity electrons. It also leads to the chaotic motion of electrons in phase space

and finally to the destruction of electron holes.

5: The birth and destruction of the electron holes transforms the kinetic energy of electron beams into thermal energy of electrons and ions and acts as an effective drag on electrons. As a result, turbulence induced anomalous resistivity can play an important role in fast magnetic reconnection.

What is unclear to us is what determines the phase speed of the lower hybrid instability and electron-electron two-stream instability. The dynamics is determined by their phase speed.

In our studies turbulence effectively converts the electron streaming energy into thermal energy. However, the turbulent dissipation does not significantly accelerate the process of magnetic reconnection. The simulation studies in past years on fast magnetic reconnection show that the Hall effect facilitates fast reconnection and that the reconnection rate is independent of the mechanism of dissipation (Shay & Drake 1998; Hesse et al. 1999; Birn et al. 2001). Our results seem consistent with this result. However, it remains unclear if anomalous resistivity facilitate fast magnetic reconnection without the Hall effect which is generically contained within the PIC mode (Kulsrud 1998; Ji et al. 1998; Kulsrud et al. 2005). This issue requires further exploration. Electron-positron magnetic reconnection might be a good choice to study the role of anomalous resistivity in which Hall effect is absent and turbulence is dominant.

BIBLIOGRAPHY

Akhiezer, A. I., Akhiezer, I. A., Polovin, R. V., Sitenko, A. G., & Stepanov, K. N. 1967 (English edition: The MIT Press)

Aydemir, A. Y. 1992, *Phys. Fluid B*, 4, 3469

Berk, H. L. & Roberts, K. V. 1967, *Phys. Fluids*, 10, 1595

Bernstein, I. B., Greene, J. M., & Kruskal, M. D. 1957, Physical Review, 108, 546

Birn, J., Drake, J. F., Shay, M. A., Rogers, B. N., Denton, R. E., Hesse, M., Kuznetsova, M., Ma, Z. W., Bhattacharjee, A., Otto, A., & Pritchett, P. L. 2001, *J. Geophys. Res. (Space Phys.)*, 106, 3715

Birn, J. & Priest, E. R. 2007, Reconnection of magnetic fields : magnetohydrodynamics and collisionless theory and observations (Reconnection of magnetic fields : magnetohydrodynamics and collisionless theory and observations / edited by J. Birn and E. R. Priest. Cambridge : Cambridge University Press, 2007. ISBN: 9780521854207 (hbk.))

Biskamp, D. 1986, *Phys. Fluids*, 29, 1520

—. 1994, *Physics Reports*, 237, 179

Boris, J. P., Dawson, J. M., Orens, J. H., & Roberts, K. V. 1970, *Phys. Rev. Lett.*, 25, 706

Buneman, O. 1958, *Phys. Rev. Lett.*, 1, 8

Cafaro, E., Grasso, D., Pegoraro, F., Porcelli, F., & Saluzzi, A. 1998, *Phys. Rev. Lett.*, 80, 4430

Carrington, R. C. 1859, *MNRAS*, 20, 13

Carter, T. A., Yamada, M., Ji, H., Kulsrud, R. M., & Trintchouk, F. 2002, *Phys. Plasmas*, 9, 3272

Cattell, C., Dombeck, J., Wygant, J., Drake, J. F., Swisdak, M., Goldstein, M. L., Keith, W., Fazakerley, A., André, M., Lucek, E., & Balogh, A. 2005, *J. Geophys. Res. (Space Phys.)*, 110, 1211

Cattell, C. A., Dombeck, J., Wygant, J. R., Hudson, M. K., Mozer, F. S., Temerin, M. A., Peterson, W. K., Kletzing, C. A., Russell, C. T., & Pfaff, R. F. 1999, *Geophys. Res. Lett.*, 26, 425

Cowley, S. W. H. 1975, *J. Plasma Phys.*, 14, 475

Davidson, R. C. 1972, Methods in nonlinear plasma theory., ed. R. C. Davidson

Davidson, R. C. 1984, in Basic Plasma Physics: Selected Chapters, Handbook of Plasma Physics, Volume 1, ed. A. A. Galeev & R. N. Sudan, 519–585

Davidson, R. C. & Gladd, N. T. 1975, *Phys. Fluids*, 18, 1327

Drake, J. F., Shay, M. A., Thongthai, W., & Swisdak, M. 2005, *Phys. Rev. Lett.*, 94, 095001

Drake, J. F., Swisdak, M., Cattell, C., Shay, M. A., Rogers, B. N., & Zeiler, A. 2003, *Science*, 299, 873

Dungey, J. W. 1953, *MNRAS*, 113, 180

Dupree, T. H. 1983, *Phys. Fluids*, 26, 2460

Farrell, W. M., Desch, M. D., Kaiser, M. L., & Goetz, K. 2002, *Geophys. Res. Lett.*, 29, 190000

Fox, W., Porkolab, M., Egedal, J., Katz, N., & Le, A. 2008, *Phys. Rev. Lett.*, 101, 255003

Galeev, A. A. & Sagdeev, R. Z. 1984a, in Basic Plasma Physics: Selected Chapters, Handbook of Plasma Physics, Volume II, ed. A. A. Galeev & R. N. Sudan, 271–303

Galeev, A. A. & Sagdeev, R. Z. 1984b, in Basic Plasma Physics: Selected Chapters, Handbook of Plasma Physics, Volume I, ed. A. A. Galeev & R. N. Sudan, 683–711

Giovanelli, R. G. 1946, *Nature*, 158, 81

Goldman, M. V., Newman, D. L., & Pritchett, P. 2008, *Geophys. Res. Lett.*, 35, 22109

Haeff, A. V. 1949, Proc. Inst. radio Engrs., 37, 4

Hesse, M., Kuznetsova, M., & Birn, J. 2004, *Phys. Plasmas*, 11, 5387

Hesse, M., Kuznetsova, M., & Hoshino, M. 2002, *Geophys. Res. Lett.*, 29, 4

Hesse, M., Schindler, K., Birn, J., & Kuznetsova, M. 1999, *Phys. Plasmas*, 6, 1781

Hodgson, R. 1859, *MNRAS*, 20, 15

Horiuchi, R. & Sato, T. 1994, *Phys. Plasmas*, 1, 3587

Hoyle, F. 1949, Some recent researches in solar physics. (Cambridge [Eng.] University Press, 1949.)

Imada, S., Nakamura, R., Daly, P. W., Hoshino, M., Baumjohann, W., Mühlbachler, S., Balogh, A., & Rème, H. 2007, *J. Geophys. Res. (Space Phys.)*, 112, 3202

Ji, H., Terry, S., Yamada, M., Kulsrud, R., Kuritsyn, A., & Ren, Y. 2004, *Phys. Rev. Lett.*, 92, 115001

Ji, H., Yamada, M., Hsu, S., & Kulsrud, R. 1998, *Phys. Rev. Lett.*, 80, 3256

Kleva, R. G., Drake, J. F., & Waelbroeck, F. L. 1995, *Phys. Plasmas*, 2, 23

Kulsrud, R., Ji, H., Fox, W., & Yamada, M. 2005, Plasma Physics, 12, 082301

Kulsrud, R. M. 1998, *Phys. Plasmas*, 5, 1599

—. 2001, Earth, Planets, and Space, 53, 417

—. 2005, Plasma physics for astrophysics (Plasma physics for astrophysics / Russell M. Kulsrud. Princeton, N.J. : Princeton University Press, c2005. (Princeton series in astrophysics))

Laval, G., Pellat, R., & Vuillemin, M. 1966, in Plasma Physics and Controlled Nuclear Fusion Research Vol. II, (IAEA, Vienna), 259

Lin, R. P. & Hudson, H. S. 1971, , 17, 412

Mandt, M. E., Denton, R. E., & Drake, J. F. 1994, *Geophys. Res. Lett.*, 21, 73

Matsumoto, H., Deng, X. H., Kojima, H., & Anderson, R. R. 2003, *Geophys. Res. Lett.*, 30, 060000

McMillan, B. F. & Cairns, I. H. 2006, *Phys. Plasmas*, 13, 052104

—. 2007, *Phys. Plasmas*, 14, 012103

Miller, J. A. 1997, *The Astrophsical Journal Letters*, 491, 939

Nergaard, L. S. 1948, RCA Rev. 9, 585, 9, 585

Øieroset, M., Lin, R. P., Phan, T. D., Larson, D. E., & Bale, S. D. 2002, *Phys. Rev. Lett.*, 89, 195001

Omura, Y., Heikkila, W. J., Umeda, T., Ninomiya, K., & Matsumoto, H. 2003, *J. Geophys. Res. (Space Phys.)*, 108, 0148

Oppenheim, M. M., Vetoulis, G., Newman, D. L., & Goldman, M. V. 2001, *Geophys. Res. Lett.*, 28, 1891

Papadopoulos, K. 1977, Reviews of Geophysics and Space Physics, 15, 113

Papadopoulos, K. & Palmadesso, P. 1976, *Phys. Fluids*, 19, 605

Parker, E. N. 1957, *J. Geophys. Res. (Space Phys.)*, 62, 509

—. 1963, *The Astrophsical Journal Supplement*, 8, 177

Petschek, H. E. 1964, in The Physics of Solar Flares, ed. W. N. Hess, 425–+

Pierce, J. R. 1949, J. Appl. Phys., 19, 231

Pierce, J. R. & Hebenstrett, W. B. 1949, Bell System Tech. J., 28, 33

Priest, E. & Forbes, T. 2000, Magnetic Reconnection (Magnetic Reconnection, by Eric Priest and Terry Forbes, pp. 612. ISBN 0521481791. Cambridge, UK: Cambridge University Press, June 2000.)

Priest, E. R. & Forbes, T. G. 1986, *J. Geophys. Res. (Space Phys.)*, 91, 5579

Pritchett, P. L. & Coroniti, F. V. 2004, *J. Geophys. Res. (Space Phys.)*, 109, 1220

Retinò, A., Sundkvist, D., Vaivads, A., Mozer, F., André, M., & Owen, C. J. 2007, Nature Physics, 3, 236

Ricci, P., Lapenta, G., & Brackbill, J. U. 2002, *Geophys. Res. Lett.*, 29, 3

Rogers, B. N., Denton, R., Drake, J., & Shay, M. 2001, *Physical Review E*, 87, 195004

Rogers, B. N., Kobayashi, S., Ricci, P., Dorland, W., Drake, J., & Tatsuno, T. 2007, *Phys. Plasmas*, 14, 092110

Rowland, H. L., Palmadesso, P. J., & Papadopoulos, K. 1981, *Phys. Fluids*, 24, 832

Sagdeev, R. Z. & Galeev, A. A. 1969, Nonlinear Plasma Theory (Nonlinear Plasma Theory, New York: Benjamin)

Sagdeev, R. Z., Usikov, D. A., & Zaslavsky, G. M. 1988, Nonlinear physics. From the pendulum to turbulence and chaos (Contemporary Concepts in Physics, Chur, Switzerland ; New York : Harwood Academic Publishers)

Sato, T. & Hayashi, T. 1979, *Phys. Fluids*, 22, 1189

Scholer, M. 1989, *J. Geophys. Res. (Space Phys.)*, 94, 8805

Shay, M. A. & Drake, J. F. 1998, *Geophys. Res. Lett.*, 25, 3759

Singh, N., Loo, S. M., Wells, B. E., & Lakhina, G. S. 2001a, *J. Geophys. Res. (Space Phys.)*, 106, 21165

Singh, N., Loo, S. M., & Wells, E. 2001b, *J. Geophys. Res. (Space Phys.)*, 106, 21183

Sonnerup, B. U. O. & Ledley, B. G. 1979, *J. Geophys. Res. (Space Phys.)*, 84, 399

Sonnerup, B. U. O. & Priest, E. R. 1975, *J. Plasma Phys.*, 14, 283

Stix, T. H. 1962, The Theory of Plasma Waves, ed. T. H. Stix (New York: McGraw-Hill, 1962)

Sundkvist, D., Retinò, A., Vaivads, A., & Bale, S. D. 2007, *Phys. Rev. Lett.*, 99, 025004

Sweet, P. A. 1958, in IAU Symp. 6: Electromagnetic Phenomena in Cosmical Physics, ed. B. Lehnert, 123–134

Swisdak, M., Drake, J. F., Shay, M. A., & McIlhargey, J. G. 2005, *J. Geophys. Res. (Space Phys.)*, 110, 5210

Tanaka, M. 1996, *Phys. Plasmas*, 3, 4010

Teste, A. & Parks, G. K. 2009, *Phys. Rev. Lett.*, 102, 075003

Ugai, M. 1995, *Phys. Plasmas*, 2, 388

Uzdensky, D. A. & Kulsrud, R. M. 2000, *Phys. Plasmas*, 7, 4018

Wang, X., Bhattacharjee, A., & Ma, Z. W. 2000, *J. Geophys. Res. (Space Phys.)*, 105, 27633

Yamada, M., Ji, H., Hsu, S., Carter, T., Kulsrud, R., & Trintchouk, F. 2000, *Phys. Plasmas*, 7, 1781

Yeh, T. & Axford, W. I. 1970, *J. Plasma Phys.*, 4, 207

Zeiler, A., Biskamp, D., Drake, J. F., Rogers, B. N., Shay, M. A., & Scholer, M. 2002, *J. Geophys. Res. (Space Phys.)*, 107, 1230